BRNO UNIVERSITY OF TECHNOLOGY

VYSOKÉ UČENÍ TECHNICKÉ V BRNĚ

CENTRAL EUROPEAN INSTITUTE OF TECHNOLOGY BUT

STŘEDOEVROPSKÝ TECHNOLOGICKÝ INSTITUT VUT

COHERENCE GATED HOLOGRAPHIC MICROSCOPY

HOLOGRAFICKÁ MIKROSKOPIE VYUŽÍVAJÍCÍ KOHERENČNÍ BRÁNY

DOCTORAL THESIS

DIZERTAČNÍ PRÁCE

AUTHOR — **Ing. Miroslav Ďuriš**

AUTOR PRÁCE

SUPERVISOR — **prof. RNDr. Radim Chmelík, Ph.D.**

ŠKOLITEL

BRNO 2023

Abstract

Biomedical and metasurface researchers repeatedly reach for quantitative phase imaging (QPI) as their primary imaging technique due to its high-throughput, label-free, quantitative nature. Therefore, QPI has quickly established its role in identifying rare events and screening in biomedicine or automated image data analysis using artificial intelligence. These and many other applications share the requirement for extensive high-quality datasets, which is challenging to meet due to obstacles specific to each application. This thesis tackles the principal problems of optical imaging, mainly in biomedical research. The research aimed to study and develop new imaging methods by extending the capabilities of the coherence-controlled holographic microscope. In the thesis, we tackled three principal areas of biomedical imaging: turbid media imaging, super-resolution QPI, and 3D refractive index reconstruction.

To achieve such ambitious results, we have utilized the so-called coherence-gating effect, typically exploited for imaging through disordered media by least-scattered (ballistic) light. To tackle turbid media imaging, we counterintuitively use the coherence gate for imaging by the non-ballistic light, enabling us to retrieve information missing in the ballistic image. A combination of images for different coherence gate positions allow us to synthesize an image of quality superior to ballistic light approaches, which we experimentally demonstrate on QPI through thick biological tissue.

Two approaches to super-resolution QPI were explored in the thesis. First is the synthetic aperture approach, for which we again exploit the coherence-gating properties of the partially coherent light combined with the oblique illumination provided by the diffraction on a simple hexagonal phase grating placed near the specimen. We synthesize synthetic aperture QPI with significantly increased spatial frequency bandwidth from sequentially acquired images formed by the coherence-gated light scattered into each grating's diffraction order. Second, we developed the coherence gate shaping method allowing real-time super-resolution QPI. We propose an approach based on the fact that our system's point spread function (PSF) is a product of the diffraction-limited spot and the coherence-gating function, which we shape similarly to the superoscillatory hotspot. The product simultaneously produces the PSF with a super-resolution central peak and minimizes sidelobe effects, the common obstacle of superoscillatory imaging. The attenuation of sidelobes and resolution improvement co-occur in the entire field of view. Therefore, we present the first single-shot wide-field super-resolution QPI. For both methods, we achieved a resolution improvement of at least 19%. Furthermore, we demonstrate the feasibility of the proposed methods by imaging biological specimens with super-resolution.

In the thesis, we also address 3D imaging by the coherence-controlled holographic microscope. We developed a method for 3D refractive index distribution reconstruction from a z-stack QPI measurement. The reconstructed refractive index distribution has qualities similar to the outputs of optical diffraction tomography. At the same time, the required number of acquisitions is significantly lower in the case of the proposed method. We demonstrate our approach using simulated as well as experimental data.

Keywords

holographic microscopy, imaging in turbid media, coherence gate, super-resolution, 3D imaging

Abstrakt

Výskumníci v oblasti biomedicíny a metapovrchov opakovane siahajú po kvantitatívnom fázovom zobrazovaní (QPI) ako primárnej zobrazovacej technike vďaka jej vysokovýkonnému, neinvazívnemu a kvantitatívnemu charakteru. Preto si QPI rýchlo vybudovalo svoju nepostrádateľnú úlohu pri identifikácii zriedkavých javov a skríningu v biomedicíne alebo automatizovanej analýze obrazových dát pomocou umelej inteligencie. Tieto a mnohé ďalšie aplikácie zdieľajú náročné splnieľnú požiadavku na rozsiahle a kvalitné súbory dát. Táto práca sa zaoberá základnými problémami optického zobrazovania a to hlavne v biomedicínskom výskume. Výskum v tejto práci je zameraný na štúdium a vývoj nových zobrazovacích metód rozšírením možností koherenciou riadeného holografického mikroskopu. V práci sme sa zaoberali tromi hlavnými oblasťami biomedicínskeho zobrazovania: zobrazovaním v kalnom prostredí, QPI so superrozlíšením a rekonštrukciou 3D rozloženia indexu lomu.

Na dosiahnutie takýchto ambicióznych výsledkov sme využili takzvaný efekt koherenčnej brány, ktorý sa zvyčajne využíva na zobrazovanie cez nepriehľadné médiá najmenej rozptýleným (balistickým) svetlom. Zobrazovanie v kalných prostrediach adresujeme v tejto práci tak, že neintuitívne používame koherenčnú bránu na zobrazovanie nebalistickým svetlom, čo nám umožňuje získať informácie chýbajúce v balistickom obraze. Kombinácia obrazov pre rôzne pozície koherenčnej brány nám umožňuje syntetizovať obraz kvalitnejší ako prístupy využívajúce len balistické svetlo. Toto experimentálne demonštrujeme na kvantitatívnom zobrazovaní cez hrubé biologické tkanivo.

V práci boli skúmané dva prístupy k superrozlíšeniu kvantitatívneho fázového obrazu. Prvým je prístup adaptujúci syntetickú apertúru, pre ktorý opäť využívame efekty koherenčného bránovania čiastočne koherentného svetla v kombinácii so šikmým osvetlením, ktoré zabezpečuje difrakcia na jednoduchej šesťuholníkovej fázovej mriežke umiestnenej v blízkosti vzorky. Syntetizujeme QPI s výrazne zväčšeným pásmom priestorových frekvencií zo sekvenčne získaných obrazov vytvorených koherenčne filtrovaným svetlom rozptýleným do každého difrakčného rádu mriežky. Ďalej sme vyvinuli metódu tvarovania koherenčnej brány, ktorá umožňuje QPI so superrozlíšením v reálnom čase. V práci navrhujeme prístup založený na skutočnosti, že rozptylová funkcia nášho systému je súčin difrakčne limitovaného obrazu bodového objektu a funkcie koherenčnej brány, ktorú tvarujeme podobne ako superoscilačný hotspot. Výsledok súčinu je rozptylová funkcia so sub-difrakčne limitovanou šírkou centrálneho peaku a so zanedbateľnými postrannými maximami, ktoré sú bežnou prekážkou zobrazovania pomocou superoscilácií. Útlm postranných maxím a zlepšenie rozlíšenia sa odohráva súčasne v celom zornom poli. Preto predstavujeme prvé jednosnímkové QPI so superrozlíšením. Pri oboch metódach sme dosiahli zlepšenie rozlíšenia aspoň o 19%.

V práci sa taktiež venujeme aj 3D zobrazovaniu pomocou koherenciou riadeného holografického mikroskopu. Vyvinuli sme metódu na rekonštrukciu 3D distribúcie indexu lomu zo série kvantitatívnych fázových obrazov vzorky pre rôzné pozície v axiálnom smere. Rekonštruovaná distribúcia indexu lomu má vlastnosti podobné výstupom optickej difrakčnej tomografie. Zároveň je ale potrebný počet akvizícií v prípade navrhovanej metódy výrazne nižší. Náš prístup demonštrujeme pomocou simulovaných, ako aj experimentálnych údajov.

Kľúčové slová

holografická mikroskopia, zobrazovanie v opticky kalných prostrediach, koherenčná brána, super-rozlíšenie, 3D zobrazovanie

ĎURIŠ, M. *Coherence gated holographic microscopy*. Doctoral Thesis. Brno University of Technology, Central European Institute of Technology, Brno 2024. 100 p. Supervisor prof. RNDr. Radim Chmelík, Ph.D.

I declare that I have written this thesis on my own with the help of expert supervision provided by prof. RNDr. Radim Chmelík, Ph.D. and using the sources listed in the bibliography at the end of this thesis.

Dec 7, 2023 Ing. Miroslav Ďuriš

I would like to express thanks to my supervisor prof. RNDr. Radim Chmelík, Ph.D., for his expert guidance and discussions as well as valuable suggestions on improving my thesis. A special thanks to my family for the excellent care and support I was provided by during my whole studies.

Ing. Miroslav Ďuriš

Contents

Chapter 1

Introduction

Digital holography has established over the years an irreplaceable role as a technique allowing convenient measurement of a wavefront [1]. There is a persistent dogma that only coherent light source is suitable for digital holography because coherent light allows very simple interferometric setup designs and on top of that it can be mathematically easily described in any space-time point. This property makes numerous numerical processing methods to work [2–4]. However, it has been shown that the digital holography is feasible even with partially coherent light [5–7]. The partially coherent illumination provides, in comparison to the coherent one, numerous advantageous imaging properties such as higher spatial resolution, depth sectioning, and speckle noise reduction [7]. Additionally to improved imaging properties that apply even for non-interferometric techniques, there is an intrinsic effect that arises only in the interferometers with partially coherent illumination - the coherence-gating effect [8–10]. The coherence gate is used as a tool separating the ballistic (the least scattered) from the multiply scattered light. This provides microscopes with ability to image in turbid media [11–14] and optical sectioning capabilities [6, 15] extending their possible applications in biomedical research [16–18]. The drawbacks of the partially coherent illumination lie in its difficult description by at least four-dimensional functions and interpretation of their measurement. The most common representations include cross-spectral density, mutual coherence function, and phase-space distributions [19]. Approaching partially coherent systems similarly to coherent ones proved to provide very good results, but to a limited extent [20, 21]. The experimentally challenging measurement of the functions representing partially coherent light is redeemed by being irreplaceable in illumination source characterization [22, 23], crystallography [24, 25], three-dimensional object reconstruction [26], quantitative phase imaging [27] or object tracking behind opaque structures [28, 29].

This thesis deals with the use of the coherence-controlled holographic microscope and its coherence-gating properties to improve its imaging capabilities. We approach the problem by utilizing an advanced coherence gate manipulation and the complete mutual coherence function measurement, which is applicable also to techniques such as optical coherence tomography and microscopy [30], achromatic digital holography [5, 7], Horn microscopy [31] or white-light diffraction tomography [15] that measure only a very limited part of the mutual coherence function. We tackle principal optical imaging problems including imaging through scattering media and super-resolved imaging by mastering imaging by multiply scattered light. It has been shown in coherent sys-

tems that suitable post-processing leads to the 3D object reconstruction [3, 32], seeing through opaque structures [33] or resolution improvement [34]. However, the use of partially coherent light promises unprecedented imaging capabilities and qualities.

Chapter 2

Theoretical framework

2.1 Optical coherence theory

The term coherence represents in physics several distinct concepts. It usually describes limiting cases that allow interpretation of underlying physics, but they never quite occur in reality. In optics, coherence is an ideal wave property enabling stationary interference. More generally, coherence describes all correlation properties between physical quantities of a single wave or between several waves quantified by the cross-correlation function. All natural sources produce time-varying fields with complicated and irregular waveforms. The field propagation greatly modifies these waveforms due to diffraction. Even though the field fluctuations are too rapid to be observed directly and waveforms are not precisely known, one can deduce their existence and shape from suitable experiments. The optical coherence theory provides mathematical models that are very successful in describing the statistical wave properties and their effect on the measurable time-averaged intensity. It is based on the electromagnetic wave theory of light and uses statistical techniques to analyze the effects of temporal and spatial waveform fluctuations.

2.1.1 Analytic Signal Representation

The typical variables treated in optics, e.g., components of electric and magnetic fields that are solutions of the time-dependent, macroscopic Maxwell's equations, are real functions of position and time. These scalar components can be represented by a real field variable $u^{(\mathrm{r})}(\mathbf{q},t)$ at a point described by a position vector $\mathbf{q} = (x,y,z)$ and at time t. The polychromatic field can be expressed as a superposition of monochromatic components

$$\widetilde{u}^{(r)}(\mathbf{q},\nu) = \widetilde{u}_0(\mathbf{q},\nu)\cos[\phi(\mathbf{q},\nu) - 2\pi\nu t], \tag{2.1}$$

where $\widetilde{u}_0(\mathbf{q},\nu)$ is the field magnitude, $\phi(\mathbf{q},\nu)$ is the time-independent phase delay and ν is the field's temporal frequency. It is more convenient to carry out the analysis in terms of the associated complex analytic signal $u(\mathbf{q},t)$ instead of using the real field variable. This eliminates the need of trigonometric identities when adding or multiplying field amplitudes. The time-dependent deterministic complex analytic signal is defined as

$$u(\mathbf{q},t) = \int_0^\infty \widetilde{u}(\mathbf{q},\nu)\mathrm{e}^{-2\pi\mathrm{i}\nu t}\mathrm{d}\nu, \tag{2.2}$$

which is the Fourier transform of the phasor $\widetilde{u}(\mathbf{q},\nu) = \widetilde{u}_0(\mathbf{q},\nu)\exp[\mathrm{i}\phi(\mathbf{q},\nu)]$. Because of the Hermitian symmetry the negative frequency components do not carry any additional information to the positive frequency components, therefore, the integration can be carried out from 0 to ∞ without any loss of generality [35].

However, the coherence theory usually does not deal with deterministic fields but with real stationary random processes. We can again associate analytic signals with these processes as well, one has to be cautious, though, because sample functions of a stationary stochastic process are not square-integrable. We choose the same workaround as in Ref. [35] by formally defining the analytic signal according to Eq. (2.2) without any further justification.

2.1.2 Temporal coherence

The simplest correlation phenomenon of optical fields is the interference effect due to superposition of two light beams originating from the same source. When the two beams are combined after propagation through optical paths that differ by $\Delta l = c\Delta t$ (c is the speed of light in vacuum) the fringes may form. The fringe formation is conditional on temporal coherence between the beams. The fringes will be formed only if the time delay Δt satisfies [35]

$$\Delta t \Delta \nu \lesssim 1, \tag{2.3}$$

where $\Delta\nu$ is bandwidth of the light. The time delay $\Delta t \sim 1/\Delta\nu$ is called the *coherence time* and the corresponding path difference $\Delta l = c\Delta t$ is known as the *coherence length*.

2.1.3 Spatial coherence

The possible formation of interference fringes on superposition of beams originating from two spatially distinct points of the source or the wavefront is described by spatial coherence between the fields at these points. The existence of this phenomenon can be revealed by the Young's double-slit interference experiment. The fringes appear as a manifestation of the finite correlation between field vibrations at the two pinholes, which can be considered as two separate light sources. The spatial coherence is usually quantified by coherence width or area. In some cases it is useful to use the concept of coherence volume, which is defined as the right-angle cylinder with base of coherence area and height being the coherence length [35].

2.1.4 Optical coherence quantification

The high frequency optical vibrations of the order of $10^{14}\,\mathrm{s}^{-1}$ are not detectable by the typical photoelectric devices, which can reach sampling frequencies of $10^{9}\,\mathrm{s}^{-1}$. Higher frequency measurements can be though obtained using special techniques designed for very specific scenarios [36–38]. It has been shown that the measurable quantity, time-averaged intensity, contains the high frequency information in the form of auto-correlation and cross-correlation contributions. A well designed interference experiment

has to be used in order to allow extraction of the sought information. It is usually sufficient to take into account only second-order correlations, therefore we will focus on the study and measurement of the correlations between two space-time points of the optical field.

Suppose that signals originating from two point sources producing time-varying stationary and ergodic fields $u(\mathbf{q}_1,t-t_1)$ and $u(\mathbf{q}_2,t-t_2)$ time delayed by t_1 and t_2 are superposed, and time-averaged intensity $\langle|u(\mathbf{q}_1,t-t_1)+u(\mathbf{q}_2,t-t_2)|^2\rangle_t$ is recorded at the point defined by position vector $\mathbf{q}$. This can be expressed as

$$\langle i(\mathbf{q},t)\rangle_t = \langle i(\mathbf{q}_1,t)\rangle_t + \langle i(\mathbf{q}_2,t)\rangle_t + 2\mathrm{Re}\{\langle u^*(\mathbf{q}_1,t-t_1)u(\mathbf{q}_2,t-t_2)\rangle_t\}, \tag{2.4}$$

where $i(\mathbf{q}_1,t) = u^*(\mathbf{q}_1,t)u(\mathbf{q}_1,t)$ and $i(\mathbf{q}_2,t) = u^*(\mathbf{q}_2,t)u(\mathbf{q}_2,t)$ are intensity terms and the third term on the right hand side of Eq. (2.4) is the interference term, which can be described by temporal cross-correlation function. This function depends on t_1 and t_2 through their difference $\tau = t_2 - t_1$ and is known as the *mutual coherence function* $\Gamma(\mathbf{q}_1,\mathbf{q}_2,\tau)$. It is the central quantity of the optical coherence theory [36], and is defined as follows

$$\Gamma(\mathbf{q}_1,\mathbf{q}_2,\tau) = \langle u^*(\mathbf{q}_1,t)u(\mathbf{q}_2,t+\tau)\rangle_t. \tag{2.5}$$

The temporal and spatial coherence phenomena qualitatively discussed in preceding sections can be characterized by $\Gamma(\mathbf{q}_1,\mathbf{q}_1,\tau)$ and $\Gamma(\mathbf{q}_1,\mathbf{q}_2,0)$, respectively. In the case of temporal coherence, the τ parameter is crucial, while for the spatial coherence characterization the time delay τ is kept fixed and the positions $\mathbf{q}_1$ and $\mathbf{q}_2$ of the two field points are of interest. However, this distinction can be made only for very simple cases, because in general these two types of coherence are not completely independent of each other [35].

2.1.5 Cross-spectral density

In the course of optical coherence theory development it has been shown that it is much easier to work with space-frequency representation of the coherence. Therefore, the most common function used in recent publications is the *cross-spectral density* function $W(\mathbf{q}_1,\mathbf{q}_2,\nu)$ of the light disturbances at points $\mathbf{q}_1$ and $\mathbf{q}_2$ at frequency ν defined by the equation [35]

$$\langle\widetilde{u}^*(\mathbf{q}_1,\nu)\widetilde{u}(\mathbf{q}_2,\nu')\rangle = W(\mathbf{q}_1,\mathbf{q}_2,\nu)\delta(\nu-\nu'), \tag{2.6}$$

where the angular brackets denote ensemble average and the δ is the Dirac delta function. Equation (2.6) shows the meaning of cross-spectral density function as a measure of correlation between the spectral amplitudes for each frequency component of the light vibrations at points $\mathbf{q}_1$ and $\mathbf{q}_2$. The mutual coherence function and the cross-spectral density function are interconnected through Fourier transform relation, which

is the so called Wiener-Khintchine theorem:

$$\Gamma(\mathbf{q}_1,\mathbf{q}_2,\tau) = \int_0^\infty W(\mathbf{q}_1,\mathbf{q}_2,\nu)\mathrm{e}^{-2\pi\mathrm{i}\nu\tau}, \tag{2.7a}$$

$$W(\mathbf{q}_1,\mathbf{q}_2,\nu) = \int_{-\infty}^\infty \Gamma(\mathbf{q}_1,\mathbf{q}_2,\tau)\mathrm{e}^{2\pi\mathrm{i}\nu\tau}. \tag{2.7b}$$

The cross-spectral density function gains a special form when the two points $\mathbf{q}_1$ and $\mathbf{q}_2$ coincide. It will become a function of the one point location and frequency, and it is called the *spectral density of light*

$$S(\mathbf{q},\nu) = W(\mathbf{q},\mathbf{q},\nu). \tag{2.8}$$

2.1.6 Propagation of correlations

The first to show how correlations propagate was Wolf in 1955 [36] by deriving two wave equations for the mutual coherence function propagation in the following form:

$$\nabla_1^2\Gamma(\mathbf{q}_1,\mathbf{q}_2,\tau) = \frac{1}{c^2}\frac{\partial}{\partial\tau^2}\Gamma(\mathbf{q}_1,\mathbf{q}_2,\tau), \tag{2.9a}$$

$$\nabla_2^2\Gamma(\mathbf{q}_1,\mathbf{q}_2,\tau) = \frac{1}{c^2}\frac{\partial}{\partial\tau^2}\Gamma(\mathbf{q}_1,\mathbf{q}_2,\tau), \tag{2.9b}$$

where the indexed Laplacian operator means $\nabla_i^2 = \frac{\partial^2}{\partial x_i^2} + \frac{\partial^2}{\partial y_i^2} + \frac{\partial^2}{\partial z_i^2}$. These equations describe how the mutual coherence function evolves, while one of the two points ($\mathbf{q}_1$ or $\mathbf{q}_2$) is fixed, and the other one and time-delay τ vary. We make use of the time difference between two time instants t_1 and t_2, however, in experiments the parameter τ appears only in the form of the optical path difference. Eqs. (2.9) also prove the fact that spatial and temporal coherence properties of light are not mutually independent and show the link between these two properties.

By applying the Wiener-Khintchine theorem on Eqs. (2.9) we obtain differential equations for propagation of the cross-spectral density function $W(\mathbf{q}_1,\mathbf{q}_2,\nu)$ in the form of Helmholtz equations:

$$\nabla_1^2 W(\mathbf{q}_1,\mathbf{q}_2,\nu) + k^2 W(\mathbf{q}_1,\mathbf{q}_2,\nu) = 0, \tag{2.10a}$$

$$\nabla_2^2 W(\mathbf{q}_1,\mathbf{q}_2,\nu) + k^2 W(\mathbf{q}_1,\mathbf{q}_2,\nu) = 0, \tag{2.10b}$$

where $k = 2\pi\nu/c$ is the *wavenumber*. It is simpler to propagate cross-spectral density function as it obey the Helmholtz equations (2.6), which are easier to manipulate with than the wave equations for the mutual coherence function.

The differential equations allow us to rigorously derive formulas for propagation of correlations, however, in practice approximate propagation laws are often adequate. It is possible to derive equations for mutual coherence function and cross-spectral density propagation analogous to Huygens-Fresnel principle of monochromatic light

propagation. Following a derivation in Sec. 4.4.3 of Ref. [35] one obtains

$$W(\mathbf{q}_1,\mathbf{q}_2,\nu) = \int_{\mathcal{A}}\int_{\mathcal{A}} W(\mathbf{q}_1',\mathbf{q}_2',\nu)h^*(\mathbf{q}_1,\mathbf{q}_1',\nu)h(\mathbf{q}_2,\mathbf{q}_2',\nu)\mathrm{d}^2\mathbf{q}_1'\mathrm{d}^2\mathbf{q}_2', \tag{2.11}$$

where $h(\mathbf{q},\mathbf{q}',\nu)$ is a transmission function that describes the complex disturbance at $\mathbf{q}$ due to a monochromatic point source situated at $\mathbf{q}'$ of the surface $\mathcal{A}$ with frequency ν, and of unit strength and zero phase. Under assumption of quasi-monochromatic light one obtains from Eq. (2.11) approximate generalized propagation law for the mutual coherence function [35]

$$\Gamma(\mathbf{q}_1,\mathbf{q}_2,\tau) \approx \int_{\mathcal{A}}\int_{\mathcal{A}} \Gamma(\mathbf{q}_1',\mathbf{q}_2',\tau)h^*(\mathbf{q}_1,\mathbf{q}_1',\bar{\nu})h(\mathbf{q}_2,\mathbf{q}_2',\bar{\nu})\mathrm{d}^2\mathbf{q}_1'\mathrm{d}^2\mathbf{q}_2', \tag{2.12}$$

where $\bar{\nu}$ is the central frequency of light.

2.1.7 Phase-space representations

We have shown that for the complete description of partially coherent field at least a four-dimensional function is needed. In contrast, coherent light can be described just by two-dimensional complex function, which allows very simple experimental implementation and image processing. An effort has been put into development of theoretical and corresponding experimental techniques utilizing partially coherent light in order to facilitate its use for quantitative measurements. It has been shown that in some cases phase-space distributions are a suitable class of function to represent partially coherent light [39]. Namely, Wigner distribution function and ambiguity function are widely used [40, 41].

Comprehensive theoretical models of propagation [42,43] have been developed to aid the implementation of the phase-space distributions, and they have been subsequently applied to problems in brightfield, phase-contrast and other imaging techniques [19].

2.1.8 Measurement of correlations

Measurement of the functions describing cross-correlation properties of electromagnetic field has proven to be experimentally challenging [22, 23], but it is well know fact that it has an irreplaceable role in illumination source characterization [22, 23], crystallography [24, 25], three-dimensional object reconstruction [26], quantitative phase imaging [27] or object tracking behind opaque structures [28,29]. One of the first techniques was proposed by Thompson and Wolf in 1957 [37], by means of which they were able to measure spatial coherence properties of light. Complete second-order correlation measurements have been demonstrated by coherence holography [44] or using a pinhole array mask [45]. Heterodyne imaging [46] and spatial light modulator [47] have been employed to obtain phase-space distributions. Recently, subwavelength spatial coherence measurement has been achieved with plasmonic interferometry [48]. Also, higher-order correlations have been investigated to achieve super-resolved imaging [49].

2.2 Interferometric microscopy

As mentioned in Sec. 2.1.8, correlations are measured using some sort of interferometer. Even though the knowledge of complete cross-correlation information of light can be very beneficial, not all partially coherent interferometric imaging techniques strive for complete description of partially coherent light-beam. Many benefit from intrinsic *coherence-gating effect* [8–10]. This effect is caused by a limited spatiotemporal correlation of the object-scattered and reference field. Coherence gate filtering has always been perceived as a method separating the least-scattered (ballistic) light from the multiply scattered light because the ballistic part of the object-scattered field carries almost unaltered specimen information. The multiply scattered light is believed to be unsuitable for direct imaging (imaging with no extensive post-processing) as it can be randomly modulated, which results in undesirable background [50]. Techniques such as optical coherence tomography and microscopy [30], achromatic digital holography [5,7], Horn microscopy [31] or white-light diffraction tomography [15] separate ballistic light using a specific coherence gate position. This corresponds to a very limited part of the cross-correlation function measurement.

2.2.1 Coherent techniques

The state of art interferometric imaging techniques are predominantly designed to use coherent light sources (lasers), which have very high spatial and temporal coherence. The interferometers are in general composed of two optical pathways. In one of the paths is placed studied object, and the other path provides reference field. The object causes wavefront deformation, which is encoded in the phase of the light ϕ, due to refraction or reflection. The purpose of interferometers is to visualize and quantify these phase changes by introducing reference field of known properties. The reference field is not always obtained by propagating light through empty space, but it can be obtained by spatial filtering of the object scattered light. Therefore, interferometers can be categorized based on the design as dual-path or common-path. The superposed object-scattered and reference fields are recorded by electronic devices measuring time-averaged intensity. The intensity measurement contains (thanks to the interference) information about the light scattered by the object, but extraction of the cross-correlation information is not always easy. The approaches to retrieving the cross-correlation term from the intensity measurements divides further interferometers into on-axis and off-axis types.

On-axis arrangement

Suppose that monochromatic signal $u_\mathrm{o}(\mathbf{q},t) = A_\mathrm{o}(\mathbf{q},t)\exp\{\mathrm{i}[\phi_\mathrm{o}(\mathbf{q}) - 2\pi\nu t]\}$ representing object scattered light and reference signal $u_\mathrm{r}(\mathbf{q},t+\tau) = A_\mathrm{r}(\mathbf{q},t+\tau)\exp\{\mathrm{i}[\phi_\mathrm{r}(\mathbf{q}) - 2\pi\nu(t+\tau)]\}$ are superposed and their time-averaged intensity is recorded. Based on the Eq. (2.4) and (2.5) we get

$$I(\mathbf{q}) = \langle i(\mathbf{q},t)\rangle_t = I_\mathrm{o}(\mathbf{q}) + I_\mathrm{r}(\mathbf{q}) + 2\mathrm{Re}\{\Gamma(\mathbf{q},\mathbf{q},\tau)\}, \tag{2.13}$$

where $I_\mathrm{o}(\mathbf{q}) = \langle u_\mathrm{o}^*(\mathbf{q},t)u_\mathrm{o}(\mathbf{q},t)\rangle_t$ and $I_\mathrm{r}(\mathbf{q}) = \langle u_\mathrm{r}^*(\mathbf{q},t)u_\mathrm{r}(\mathbf{q},t)\rangle_t$. The third term on the right-hand side of Eq. (2.13), the mutual coherence function of the object-scattered and reference field, can be expressed as

$$\Gamma(\mathbf{q},\mathbf{q},\tau) = \langle u_\mathrm{o}(\mathbf{q},t)u_\mathrm{r}^*(\mathbf{q},t+\tau)\rangle_t = \langle A_\mathrm{o}(\mathbf{q},t)A_\mathrm{r}(\mathbf{q},t+\tau)\rangle_t \mathrm{e}^{\mathrm{i}[\phi_\mathrm{o}(\mathbf{q})-\phi_\mathrm{r}(\mathbf{q})+2\pi\nu\tau]}, \tag{2.14}$$

where $\langle A_\mathrm{o}(\mathbf{q},t)A_\mathrm{r}(\mathbf{q},t+\tau)\rangle_t$ can be regarded as the modulus of the mutual coherence function $|\Gamma(\mathbf{q},\mathbf{q},\tau)|$. In on-axis systems the reference field is usually assumed to be a flat field (plane wave), therefore the phase $\phi_\mathrm{r}(\mathbf{q})$ is zero. The quantities, one strives to determine from interferometric measurements, are $|\Gamma(\mathbf{q},\mathbf{q},\tau)|$ and $\phi_\mathrm{o}(\mathbf{q})$, which carry the information about the studied object. It is not possible to retrieve them from single on-axis measurement, which has the form

$$I(\mathbf{q};\tau) = I'(\mathbf{q}) + 2|\Gamma(\mathbf{q};\tau)|\cos[\phi_\mathrm{o}(\mathbf{q}) + 2\pi\nu\tau], \tag{2.15}$$

because there are three unknowns: $I'(\mathbf{q}) = I_\mathrm{o}(\mathbf{q}) + I_\mathrm{r}(\mathbf{q})$, the modulus of the mutual coherence function and phase $\phi_\mathrm{o}(\mathbf{q})$. The time-delay τ is now a parameter that is further exploited in order to derive the aforementioned unknowns. At least three intensity measurements with different τ have to be carried out to obtain three equations, which can be combined to solve for the phase or modulus. This approach is called the phase-shifting method. In the most used adaptation the time-delay is chosen so that $2\pi\nu\tau$

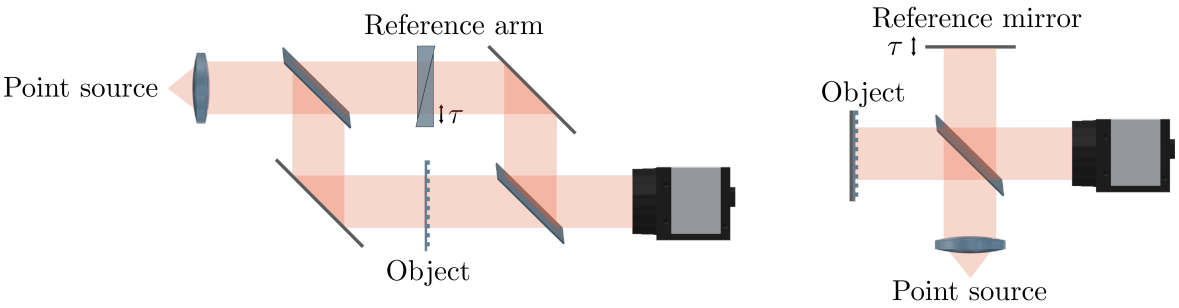

Figure 2.1: Two representative optical setups of on-axis interferometric systems. (a) Mach-Zehnder design and (b) Michelson interferometer design.

takes on values $0,\pi/2,\pi,3\pi/2$. As the light is monochromatic, the modulus $|\Gamma(\mathbf{q};\tau)|$ varies slowly with the change of τ, therefore, it is assumed to be constant for all four values of τ. One then obtains following four equations:

$$I_1(\mathbf{q}) = I'(\mathbf{q}) + 2|\Gamma(\mathbf{q};0)|\cos[\phi_\mathrm{o}(\mathbf{q})], \tag{2.16a}$$
$$I_2(\mathbf{q}) = I'(\mathbf{q}) - 2|\Gamma(\mathbf{q};0)|\sin[\phi_\mathrm{o}(\mathbf{q})], \tag{2.16b}$$
$$I_3(\mathbf{q}) = I'(\mathbf{q}) - 2|\Gamma(\mathbf{q};0)|\cos[\phi_\mathrm{o}(\mathbf{q})], \tag{2.16c}$$
$$I_4(\mathbf{q}) = I'(\mathbf{q}) + 2|\Gamma(\mathbf{q};0)|\sin[\phi_\mathrm{o}(\mathbf{q})]. \tag{2.16d}$$

The phase is easily obtained as

$$\phi_\mathrm{o}(\mathbf{q}) = \tan^{-1}\left[\frac{I_4(\mathbf{q}) - I_2(\mathbf{q})}{I_1(\mathbf{q}) - I_3(\mathbf{q})}\right]. \tag{2.17}$$

This approach can be used either in reflection setup (see Fig. 2.1b) or transmission setup (see Fig. 2.1a). The phase-stepping is carried out by moving the reference mirror in the reflection setup, and in the transmission setup an optical wedge is used to change the optical path length of the reference arm.

Off-axis arrangement - standard digital holography

The advantage of off-axis interferometric setups is the possibility to retrieve the cross-correlation information from a single measurement. The retrieval approach is based on the removal of the carrier frequency [7, 51], which is associated with the holographic signal.

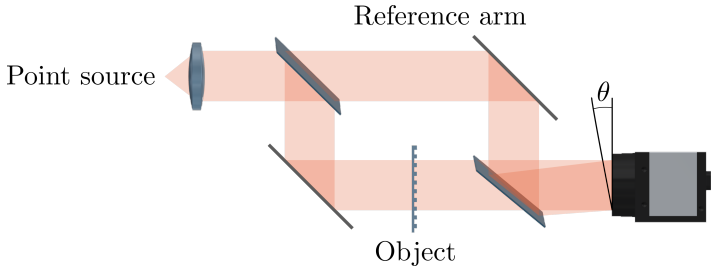

Figure 2.2: Off-axis arrangement of Mach-Zehnder interferometer.

Suppose again that the camera records time-averaged intensity of superposed monochromatic object $u_o(\mathbf{q},t)$ and reference $u_r(\mathbf{q},t)$ signals. In off-axis interferometry, the reference field is incident to the output plane at an angle (see Fig. 2.2), therefore the time-delay of the wavefront is linearly proportional to the transverse position vector $\mathbf{q}_t = (x,y)$. The object scattered field is again $u_o(\mathbf{q},t) = A_o(\mathbf{q},t)\exp\{i[\phi_o(\mathbf{q}) - 2\pi\nu t]\}$ and the reference signal is $u_r[\mathbf{q},t+\tau(\mathbf{q}_t)] = A_r[\mathbf{q},t+\tau(\mathbf{q}_t)]\exp\{-2\pi i\nu[t+\tau(\mathbf{q}_t)]\}$. The term $\nu\tau(\mathbf{q}_t)$ will be further assumed to be a superposition of a constant time-delay τ times ν and spatially varying term $\mathbf{Q}_C \cdot \mathbf{q}_t$, where $\mathbf{Q}_C = (X_C,Y_C)$ is the *carrier frequency*, which is in general dependent on ν and the tilt of the beamsplitter. The intensity measurement has following form

$$I(\mathbf{q}) = I_o(\mathbf{q}) + I_r(\mathbf{q}) + 2\mathrm{Re}\{\Gamma(\mathbf{q},\mathbf{q},\tau)e^{2\pi i\mathbf{Q}_C\cdot\mathbf{q}_t}\}. \tag{2.18}$$

This equation contains two non-modulated intensity terms and interference term modulated by the carrier frequency. The wavefront tilt originating from the interferometer design can be chosen in a way that the spatial frequency information of intensity and interference terms does not overlap in the frequency domain. Therefore, the mutual coherence function can be retrieved by Fourier transforming off-axis interferogram [described by Eq. (2.18)], then windowing the cross-correlation term centered at carrier frequency as shown in Fig. 2.3a and then applying inverse Fourier transform on the filtered part of the spectrum. For the case of monochromatic and coherent light, the modulus and argument of the complex signal represent amplitude and phase, respectively, of the object scattered light. The tilted reference wavefront results in relatively high values of the time-delay τ between two interfering wavefronts in some parts of the field of view as illustrated in Fig. 2.3b. The need for complete separation of interference

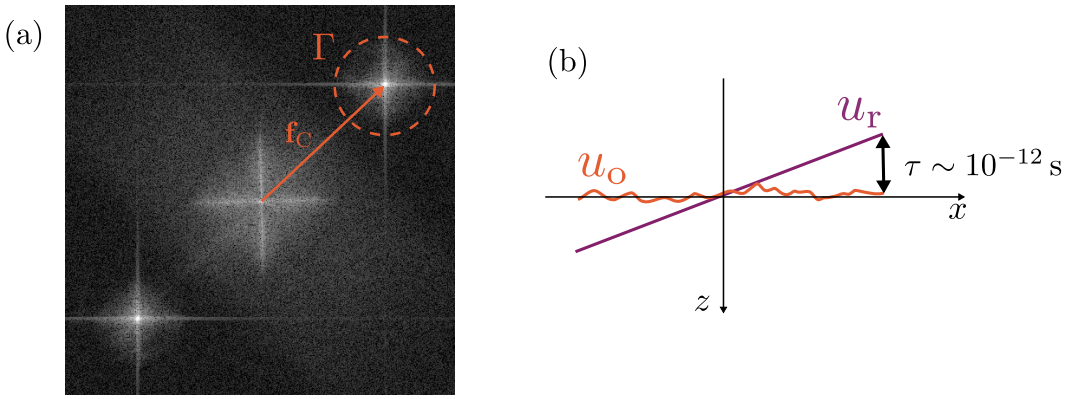

Figure 2.3: (a) Example of the spatial frequency representation of the measured off-axis interferogram when imaging through diffuser. (b) Illustration of the time-delay in the case of tilted wavefront in off-axis holography.

from intensity terms is the reason of time-delays in the order of 10^{-12} s. This imposes corresponding coherence demands on the illumination source. For example halogen lamp has the coherence time in the order of 10^{-14} s, which is by no means sufficient for off-axis holography. This requirement of very high temporal coherence of illumination in the off-axis holography is usually met only when a laser source is used.

2.2.2 Partially coherent techniques

Spatially and temporally low coherence of illumination provides substantial benefits to the wide-field light microscopy. The superposition of contributions from each source point and wavelength leads to the suppression of coherence artifacts. Unwanted interference and diffraction effects originating from imperfections and inhomogeneities in an optical system. Additionally, the implementation of a broad spatially incoherent source reduces the resolution limit in comparison with the central illumination [52]. A very important effect, called coherence-gating effect, occurs in interferometric systems utilizing partially coherent illumination. This effect is caused by a limited spatiotemporal correlation of the object-scattered and reference field. Coherence gate filtering has always been perceived as a method separating the least-scattered (ballistic) light from the multiply scattered light because the ballistic part of the object-scattered field carries almost unaltered specimen information. The multiply scattered light is believed to be unsuitable for direct imaging (imaging with no extensive post-processing) as it can be randomly modulated, which results in undesirable background [50]. There have been developed numerous techniques relying on the coherence-gating effect, e.g., optical coherence tomography and microscopy [30], achromatic digital holography [5, 7], Horn microscopy [31] or white-light diffraction tomography [15]. Besides achromatic digital holography, all of the mentioned techniques use on-axis interferometer arrangement, and rely on phase-shifting retrieval of the mutual coherence function, because partially coherent light does not meet coherence requirements of off-axis digital holography as shown in Sec. 2.2.1.

2.3 Coherence-controlled holographic microscope

The first achromatic off-axis holographic microscope allowing imaging with light of arbitrarily low coherence was designed by Chmelík and Harna in reflected light arrangement [53]. The adaptation for transmitted light called Coherence-controlled holographic microscope (CCHM) was designed by Pavel Kolman [6] and the design was further improved by Tomas Slaby [7]. The imaging theory was composed in the Ref. [12]. The initial purpose of the microscope was to be used for a quantitative observation of phase samples (transparent but altering the phase of the light), such as cells or other biological specimen. Therefore, the setup is based on the Mach-Zehnder interferometer (see Fig. 2.4). The illumination beam emitted by an incoherent light source (LS) (a halogen-tungsten lamp coupled into an optical cable with aperture stop (A) and interference filter (IF) controlling the degree of spatial and temporal coherence, respectively) is split and propagates through two separate optical paths formed by identical microscope setups – condensers (C), infinity-corrected objectives (O) and tube lenses (TL). Reference (R) and specimen (S) planes are optically conjugated with the output plane (OP). An essential component of the CCHM is the diffraction grating (DG). In

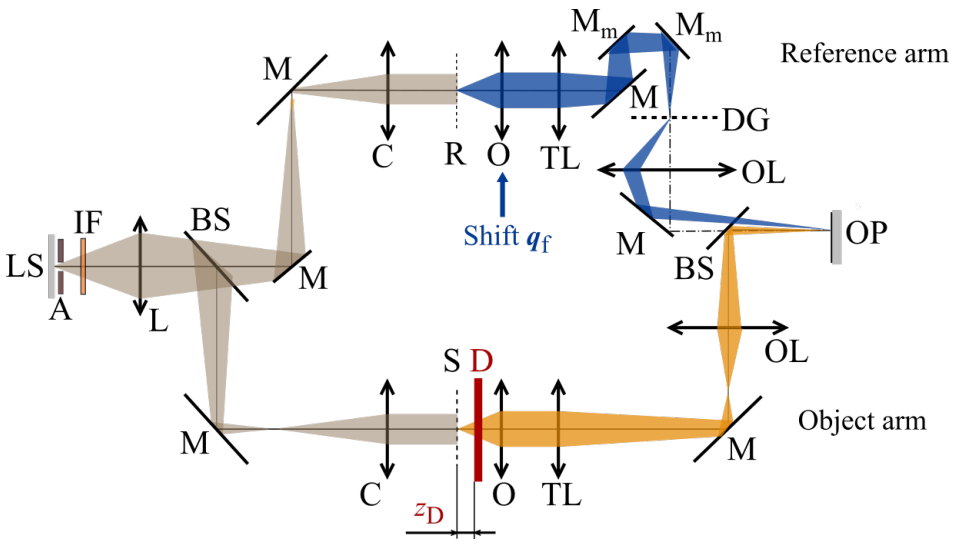

Figure 2.4: Optical set-up of coherence-controlled holographic microscope (CCHM). LS – light source, a – aperture stop of adjustable size, IF – interference filter, L – collector lens, BS – beam splitters, M – mirrors, Mm – movable mirrors, C – condenser lenses, R – reference plane, S – specimen (object) plane, D – diffuser, O – objective lenses, TL – tube lenses, OL – output lenses, DG – diffraction grating, OP – output plane.

this setup the transmission grating is placed in the reference arm and imaged onto the output plane (OP) according to the incoherent-light holography principle proposed by Leith and Upatnieks [5]. The use of the first diffraction order (other diffraction orders are eliminated by spatial filtering) for imaging results in spatially modulated reference beam by linear phase in the output plane. In the object arm, the diffraction grating is replaced by a mirror, which is equivalent to using the zeroth diffraction order. After recombination of the reference and the object beam in the output plane (OP) interference fringe pattern of the hologram appears. The fringe frequency, i.e., the hologram

carrier frequency Q_{C}, is proportional to the spatial frequency Q_{G} of diffraction grating grooves, unlike in the conventional off-axis holography microscope, where it is proportional to the introduced reference beam tilt. The proportionality relation is as follows

$$Q_{\mathrm{C}} = \frac{Q_{\mathrm{G}}}{m_{\mathrm{OL}}}, \tag{2.19}$$

where m_{OL} is the magnification of the output lens.

The microscope utilizes Köhler illumination. The light source (LS) is imaged by the collector lens (L) to the front focal planes of condensers (C). The use of Köhler illumination in combination with aperture stop (A) allows to control the spatial coherence of the illumination, which is of principal interest in numerous experiments. The downside of using highly incoherent illumination is that there are high demands on the precise alignment of optical components. Simple and fully automated procedure was developed to align microscope easily. This microscope is currently commercially available as Telight Q-Phase. Therefore, the thesis outcomes are of high impact due to potential application by numerous Telight customers.

CCHM has been already successfully deployed in cancer research [17, 18, 54] and studies of plasmonic metasurfaces [55]. CCHM was also utilized in automated classification of cell morphology [56].

Chapter 3

Thesis aims and objectives

The aim of this thesis is to extend existing and develop novel imaging techniques based on partially coherent digital holography and coherence-gating effect. The aim is to tackle principal problems of optical imaging in biomedical research and imaging of plasmonic structures, i.e., label-free imaging through turbid media, 3D object reconstruction and super-resolved imaging.

Achievement of following objectives will help reaching desired thesis outcomes:

- Extend the existing CCHM imaging theory [12] by implementing concepts of optical coherence theory.
- Derive relation for imaging through volumetric specimen using appropriate approximations.
- Develop the concept proposed in [14] into a robust routine observation method of a highly specific specimen – an object behind a strongly scattering planar layer. Further, extend the observation method to imaging through multiple scattering layers and potentially to volumetric diffusers.
- Utilize concepts of imaging by multiply scattered light to enhance the resolving power of the partially coherent microscope.
- Explore potential application of superoscillations to coherence-controlled holographic microscopy.
- Develop 3D object reconstruction method from CCHM z-stack images. The goal is to obtain refractive index reconstructions similar to optical diffraction tomography.

Chapter 4

Methods

4.1 Basic imaging principles

4.1.1 Plane wave representation

Wolf [57] has shown that any arbitrary complex signal representation $u(\mathbf{q})$ of a monochromatic wave satisfying Helmholtz equation can be expressed in terms of plane waves as a superposition

$$u(\mathbf{q}) = \iint_{-\infty}^{\infty} U(\mathbf{K}_\mathrm{t}) \exp(2\pi \mathrm{i} \mathbf{K} \cdot \mathbf{q}) \mathrm{d}^2\mathbf{K}_\mathrm{t}, \tag{4.1}$$

where $\mathbf{q} = (\mathbf{q}_\mathrm{t},z) = (x,y,z)$ is a position vector in a Cartesian coordinate system and $U(\mathbf{K}_\mathrm{t})$ is so called *angular spectrum* for the plane $z = 0$. In all our derivations we will assume that the coordinates in the image plane are represented by associated conjugate points in the object plane. Fourier optics approach is utilized for majority of derivations in this thesis, therefore, the *reduced wave vector* $\mathbf{K} = (\mathbf{K}_\mathrm{t},K_z) = (K_x,K_y,K_z)$ notation is used. For a wave propagating in the positive z-axis direction $K_z = \sqrt{K^2 - K_\mathrm{t}^2}$ holds. The magnitude of the reduced wave vector is defined as $|\mathbf{K}| = K = 1/\lambda = n/\lambda_\mathrm{v}$, where λ is a wavelength in a medium with the refractive index n and λ_v is the wavelength in a vacuum. In this notation the wave vector components has physical meaning of spatial frequencies. Therefore, it simplifies notation in spatial frequency domain. Evanescent waves are neglected by assuming $U(\mathbf{K}_\mathrm{t}) = 0$ for $K_\mathrm{t} > K$. The angular spectrum in $z = 0$ plane can be expressed according to Eq. (4.1) as

$$U(\mathbf{K}_\mathrm{t}) = \iint_{-\infty}^{\infty} u(\mathbf{q}) \exp(-2\pi \mathrm{i} \mathbf{K} \cdot \mathbf{q}) \mathrm{d}^2\mathbf{q}_\mathrm{t}. \tag{4.2}$$

4.1.2 Scattering by an object

A linear and elastic scattering of a wave with an angular spectrum $U(\mathbf{K}_\mathrm{t})$ by an object can be described as a separate scattering of individual plane wave components of the primary wave and a superposition of scattered waves spectra. The angular spectrum $U'(\mathbf{K}'_\mathrm{t})$ of the scattered field by an object is then expressed by the following integral

$$U'(\mathbf{K}'_\mathrm{t}) = \iint_{-\infty}^{\infty} \mathcal{S}(\mathbf{K}',\mathbf{K}) U(\mathbf{K}_\mathrm{t}) \mathrm{d}^2\mathbf{K}_\mathrm{t}, \tag{4.3}$$

where $\mathcal{S}(\mathbf{K}',\mathbf{K})$ is the *scattering function* of the object. The elasticity of the scattering $K' = K$ and linearity allows the integration in Eq. (4.3). In general, when a light wave undertakes multiple scattering events in the object, it may not be possible to express the function $\mathcal{S}(\mathbf{K}',\mathbf{K})$ in a closed form. However, if only single scattering is assumed, then the scattering function has following form:

$$\mathcal{S}(\mathbf{K}',\mathbf{K}) = C_0(\mathbf{K},\mathbf{Q})F(\mathbf{Q}), \tag{4.4}$$

where $\mathbf{Q} = (X,Y,Z) = \mathbf{K}' - \mathbf{K}$ is the *scattering vector*,

$$F(\mathbf{Q}) = \iiint_{-\infty}^{\infty} f(\mathbf{q}) \exp(-2\pi \mathrm{i}\mathbf{Q}\cdot\mathbf{q}) \mathrm{d}^3\mathbf{q} \tag{4.5}$$

is the Fourier transform of the *scattering potential* $f(\mathbf{q})$ of the object and $C_0(\mathbf{K},\mathbf{Q})$ is a *geometric factor* [12].

A planar object, characterized by a transmission function $t(\mathbf{q}_\mathrm{t})$, satisfies the condition of the single scattering, and for the scattering potential it holds

$$f(\mathbf{q}_\mathrm{t},z) = t(\mathbf{q}_\mathrm{t})\delta(z) \text{ and simultaneously } C_0 = 1, \tag{4.6}$$

where δ denotes the Dirac delta function.

An expression for the scattering potential was derived by Wolf [58] under the so-called first Born approximation, which holds for a weakly scattering volumetric object or when only ballistic light is used for imaging. The scattering potential has following form:

$$f(\mathbf{q}) = \mathrm{i}\pi[n^2(\mathbf{q}) - 1] \text{ and simultaneously } C_0(\mathbf{K},\mathbf{Q}) = \frac{K^2}{K_z + Z}, \tag{4.7}$$

where $n(\mathbf{q})$ is the refractive index distribution.

4.1.3 Transformation of the angular spectrum by the imaging

The angular spectrum of a light wave is always to some degree transformed by an optical system. In [52, Sec. 9.5] it is shown that in the case of a stigmatic imaging within an isoplanatic region of a system the imaging system acts as a linear filter of the object spatial frequencies. Suppose, the output plane is optically conjugated with the object plane, then the object-scattered wave angular spectrum $U_\mathrm{o}(\mathbf{K}_\mathrm{t})$ is in relation to the image angular spectrum $U_\mathrm{i}(\mathbf{K}_\mathrm{t})$ in following way [12]

$$U_\mathrm{i}(\mathbf{K}_\mathrm{t}) = P_\mathrm{T}(\mathbf{K})U_\mathrm{o}(\mathbf{K}_\mathrm{t}), \tag{4.8}$$

where the filter function P_T is called the pupil function and describes the transfer of the object wave angular spectrum U_o by an imaging system. According to [12] for a rotationally symmetrical aplanatic system the pupil function P_T takes on the

following form:

$$P_{\mathrm{T}}(\mathbf{K}) = \sqrt{\frac{K}{K_z}}\mathrm{circ}\left(\frac{K\cos\alpha}{K_z}\right) = \sqrt{\frac{K}{K_z}}\mathrm{circ}\left(K_{\mathrm{t}}\frac{\lambda_{\mathrm{v}}}{\mathrm{NA}}\right), \tag{4.9}$$

where the $\mathrm{circ}(x)$ function is defined as follows

$$\mathrm{circ}(x) = \begin{cases} 1, & \text{for } x < 1, \\ \frac{1}{2}, & \text{for } x = 1, \\ 0, & \text{for } x > 1. \end{cases} \tag{4.10}$$

4.2 Multi-slice approach to light propagation

To image 3D objects from 2D data, we need a suitable optical device and a proper reconstruction method that can recover the 3D information. The reconstruction method depends on the assumptions we make about the object. For optical imaging, we need to choose a good object representation for the inverse modeling. Objects that are thick and volumetric scatter light multiple times inside them, so the first Born approximation is not accurate for inverse reconstruction. A better way to model light propagation in these objects is the Multi-slice approach with the Beam propagation method. This approach divides the object into thin slices along the optical axis, each slice acting as a 2D transmission layer with a uniform refractive index between them [3, 59]. Further accuracy improvement of the Multi-slice approach was recently proposed by Chen et al. [59] called Multi-layer Born multiple-scattering model. This model, as depicted in Fig. 4.1, utilizes the first Born approximation at the level of each slice consecutively (and separately).

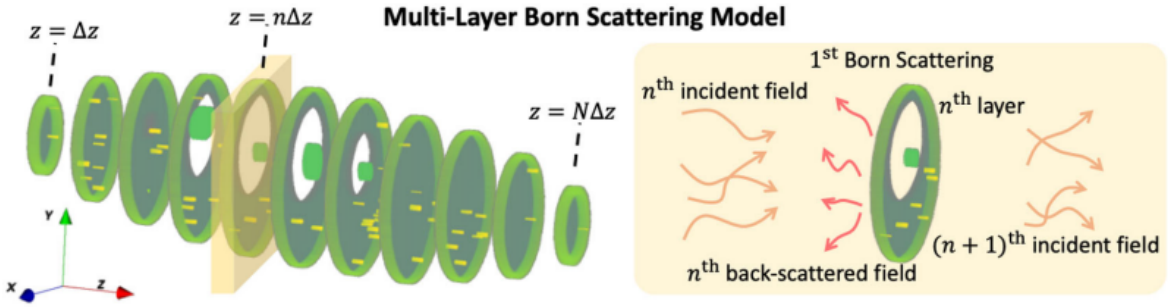

Figure 4.1: Multi-layer Born model illustration, adapted from [59].

4.3 Quantitative phase imaging

Transparent objects such as a living human cell absorb and scatter just small amounts of light. Therefore, bright-field microscopes detecting light absorption and scattering image translucent object with very low contrast. However, the light interacting with the specimen, in addition to absorption and scattering, undergoes also refraction. As

a result the light wave passing through the object has imprinted the phase retardation specific for each part of the object. The phase shifts of the incident light wave induced by the tissue structures can be in high contrast visualized by several techniques. The first solution was proposed by Frits Zernike in 1934 [60]. He developed a qualitative-only technique allowing high contrast cell imaging using a simple phase plate. The drawback of this method is solved by interferometric methods like digital holography, which provide quantitative amplitude and phase-contrast imaging. The phase dif-

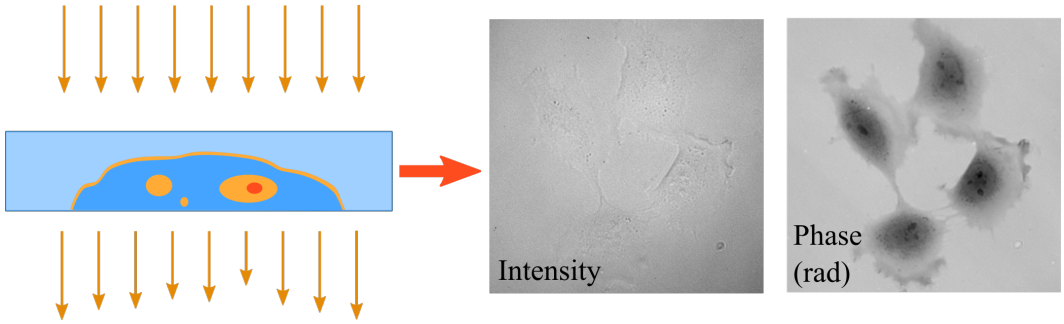

Figure 4.2: Phase retardation of the light due to the cell, nucleus and other intracellular organelles can be with high contrast visualized by quantitative phase imaging. Adapted from [61].

ference $\varphi_{\text{object}}(x,y)$ induced by a very thin transparent object with the homogeneous refractive index distribution n_{object} along optical axis surrounded by a medium of the refractive index n_{medium} can be approximated by the following relation

$$\varphi_{\text{object}}(x,y) = \frac{2\pi}{\lambda} d_{\text{object}}(x,y)(n_{\text{object}} - n_{\text{medium}}), \tag{4.11}$$

where $d_{\text{object}}(x,y)$ is the object thickness, λ is the light wavelength in vacuum, and x,y are spatial coordinates in the object plane.

The quantitative phase information is of interest in the bio-medical research because the cellular dry-mass density $\mu(x,y)$ is proportional to the phase retardation induced by a cell

$$\mu(x,y) \approx \frac{1}{\alpha}\lambda\varphi(x,y). \tag{4.12}$$

Constant α is known as the specific refractive increment [62–64].

Chapter 5

Partially coherent holographic microscope theory

5.1 Mutual coherence function of object-scattered and reference fields

To describe interferometric imaging in systems utilizing partially coherent illumination, we use the scalar description of light and a simple model of an optical system depicted in Fig. 5.1. A partially coherent planar source produces on its surface $\mathcal{S}$ at the point with position vector $\mathbf{q}_\mathcal{S} = (x_\mathcal{S},y_\mathcal{S})$ fluctuating field $u_\mathcal{S}(\mathbf{q}_\mathcal{S},t)$. The analytic signal $u_\mathcal{S}(\mathbf{q}_\mathcal{S},t)$ is assumed to be a realization of a wide-sense stationary and ergodic stochastic process. The emitted light is optically split and propagated by two separate paths to the object space. The object-scattered field $u_\mathrm{o}(\mathbf{q}_\mathrm{o},t)$ and the reference field $u_\mathrm{r}(\mathbf{q}_\mathrm{r},t+\tau)$ time-delayed by τ are stigmatically and within isoplanatic region imaged to the interference plane (IP). The position of a point in the image plane is specified by the coordinate vectors $\mathbf{q}_\mathrm{o} = (x_\mathrm{o},y_\mathrm{o},z_\mathrm{o}=0)$ and $\mathbf{q}_\mathrm{r} = (x_\mathrm{r},y_\mathrm{r},z_\mathrm{r}=0)$ of the optically conjugated point in the object plane. The time-averaged intensity measured in IP where object-scattered and refer-

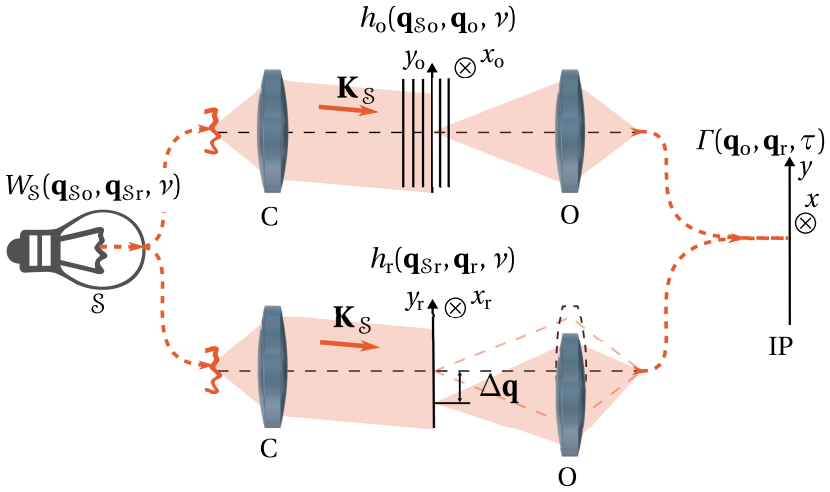

Figure 5.1: Simplified interferometer optical scheme. Partially coherent source with condenser lenses C form Köhler illumination of two distinct optical paths. In one of the optical path is placed multi-layer object. Objectives O image the produced field to the mutual interference plane IP.

ence fields are superposed can be written as $\langle i(\mathbf{q},t)\rangle_t = \langle|u_\mathrm{o}(\mathbf{q}_\mathrm{o},t)+u_\mathrm{r}(\mathbf{q}_\mathrm{r},t+\tau)|^2\rangle_t$, where

the angular brackets with the subscript t denote averaging over time and $\mathbf{q}$ is a coordinate vector of IP. The measurement contains besides intensity $\langle|u_\mathrm{o}(\mathbf{q}_\mathrm{o},t)|^2\rangle_t$, $\langle u_\mathrm{r}(\mathbf{q}_\mathrm{r},t)|^2\rangle_t$ also the cross-correlation information of the object-scattered and reference field. This cross-correlation $\Gamma(\mathbf{q}_\mathrm{o},\mathbf{q}_\mathrm{r},\tau) = \langle u_\mathrm{o}(\mathbf{q}_\mathrm{o},t)u_\mathrm{r}^*(\mathbf{q}_\mathrm{r},t+\tau)\rangle_t$ can be defined as mutual coherence function (MCF) of object-scattered and reference field. Spectral amplitudes in IP of the system with partially coherent illumination can be expressed in terms of complex amplitudes at all source surface points as $\widetilde{u}_\mathrm{o}(\mathbf{q}_\mathrm{o},\nu) = \int_\mathcal{S} \widetilde{u}_\mathcal{S}(\mathbf{q}_{\mathcal{S}\mathrm{o}},\nu)h_\mathrm{o}(\mathbf{q}_{\mathcal{S}\mathrm{o}},\mathbf{q}_\mathrm{o},\nu)\mathrm{d}^2\mathbf{q}_{\mathcal{S}\mathrm{o}}$ and $\widetilde{u}_\mathrm{r}(\mathbf{q}_\mathrm{r},\nu) = \int_\mathcal{S} \widetilde{u}_\mathcal{S}(\mathbf{q}_{\mathcal{S}\mathrm{r}},\nu)h_\mathrm{r}(\mathbf{q}_{\mathcal{S}\mathrm{r}},\mathbf{q}_\mathrm{r},\nu)\mathrm{d}^2\mathbf{q}_{\mathcal{S}\mathrm{r}}$, where $h_\mathrm{o}(\mathbf{q}_\mathcal{S},\mathbf{q},\nu)$ and $h_\mathrm{r}(\mathbf{q}_\mathcal{S},\mathbf{q},\nu)$ describe propagation of light emitted by the source point $\mathbf{q}_\mathcal{S}$ through the object and reference path. According to Eq. (2.6) the cross-correlation of these spectral amplitudes is regarded as cross-spectral density $W(\mathbf{q}_\mathrm{o},\mathbf{q}_\mathrm{r},\nu)$, see Eq. (2.11). It forms according to Wiener-Khintchine theorem [Eq. (2.7)] a Fourier transform pair with mutual coherence function, therefore we can derive from intensity measurements MCF in the form

$$\Gamma(\mathbf{q}_\mathrm{o},\mathbf{q}_\mathrm{r},\tau) = \int_0^\infty \int_\mathcal{S}\int_\mathcal{S} W_\mathcal{S}(\mathbf{q}_{\mathcal{S}\mathrm{o}},\mathbf{q}_{\mathcal{S}\mathrm{r}},\nu)h_\mathrm{o}(\mathbf{q}_{\mathcal{S}\mathrm{o}},\mathbf{q}_\mathrm{o},\nu) \times h_\mathrm{r}^*(\mathbf{q}_{\mathcal{S}\mathrm{r}},\mathbf{q}_\mathrm{r},\nu)\mathrm{e}^{-2\pi\mathrm{i}\nu\tau}\mathrm{d}^2\mathbf{q}_{\mathcal{S}\mathrm{r}}\mathrm{d}^2\mathbf{q}_{\mathcal{S}\mathrm{o}}\mathrm{d}\nu, \quad (5.1)$$

where $W_\mathcal{S}(\mathbf{q}'_\mathcal{S},\mathbf{q}_\mathcal{S},\nu)$ is the cross-spectral density of the source. As mentioned in Sec. 2.2, the extraction of the cross-correlation term can be carried out using phase-shifting method or off-axis holography approach. Both has been already applied to partially coherent imaging systems [7,31,65]. Equation (5.1) shows that complete mutual coherence function can be derived from sequential acquisition of two-dimensional intensity images under controlled adjustment of reference field parameters. Elongation of the reference optical path controls the time-delay τ and $\mathbf{q}_\mathrm{r}$ can be manipulated through reference objective shift as illustrated in Fig. 5.1.

5.2 Illumination source approximation

By assuming certain illumination source properties we are able to more conveniently interpret measurement results. Therefore, we assume planar, thermal, spatially and spectrally broad source, which can be modeled as Schell-model source with the cross-spectral density function defined as $W_\mathcal{S}(\mathbf{q}_{\mathcal{S}\mathrm{o}},\mathbf{q}_{\mathcal{S}\mathrm{r}},\nu) = [S(\mathbf{q}_{\mathcal{S}\mathrm{o}},\nu)]^{1/2}[S(\mathbf{q}_{\mathcal{S}\mathrm{r}},\nu)]^{1/2}\delta^{(2)}(\mathbf{q}_{\mathcal{S}\mathrm{o}} - \mathbf{q}_{\mathcal{S}\mathrm{r}})$, where $S(\mathbf{q}_\mathcal{S},\nu)$ is the spectral density of the light [see Eq. (2.8)] at the typical point in the source plane and $\delta^{(2)}$ is the two-dimensional Dirac delta function. The illumination source point situated in the front focal plane of the condenser lens (C) creates plane wave illumination with transverse wave vector $\mathbf{K}_\mathcal{S}$. Mutual incoherence of light emitted by two distinct points in the source plane can be interpreted as mutual incoherence of the plane waves incident to the object space. We can, therefore, formally replace $W_\mathcal{S}(\mathbf{q}_{\mathcal{S}\mathrm{o}},\mathbf{q}_{\mathcal{S}\mathrm{r}},\nu)$ in Eq. (5.1) with $W_K(\mathbf{K}_{\mathcal{S}1},\mathbf{K}_{\mathcal{S}2},\nu) = P_\mathrm{C}(\mathbf{K}_{\mathcal{S}1})P_\mathrm{C}^*(\mathbf{K}_{\mathcal{S}2})\delta^{(2)}(\mathbf{K}_{\mathcal{S}1} - \mathbf{K}_{\mathcal{S}2})\nu^{-2}S(\nu)$, where $P_\mathrm{C}(\mathbf{K}_\mathrm{t})$ is the condenser lens transfer function (equal to its pupil function) and change the integration over all source points to the integration over all plane waves formed by condenser lenses. As the IP and the object coordinate systems are conjugated, we can relate $\mathbf{q}_\mathrm{o} \equiv \mathbf{q}$. We express the reference field position

as $\mathbf{q}_\mathrm{r} \equiv \mathbf{q} - \Delta\mathbf{q}$, where $\Delta\mathbf{q} = (\Delta x,\Delta y)$ is a transverse relative displacement of the reference and object fields. Thanks to these assumptions and manipulations the MCF expression acquires following more understandable form

$$\Gamma(\mathbf{q},\mathbf{q}-\Delta\mathbf{q},\tau) = \int_0^\infty \iint_{-\infty}^{\infty} |P_\mathrm{C}(\mathbf{K}_\mathrm{S})|^2 S(\nu) \times h_\mathrm{o}(\mathbf{K}_\mathrm{S},\mathbf{q},\nu) h_\mathrm{r}^*(\mathbf{K}_\mathrm{S},\mathbf{q}-\Delta\mathbf{q},\nu) \mathrm{e}^{-2\pi\mathrm{i}\nu\tau} \nu^{-2} \mathrm{d}^2\mathbf{K}_\mathrm{S} \mathrm{d}\nu. \quad (5.2)$$

This equation shows the relation between illumination system properties $P_\mathrm{C}(\mathbf{K}_\mathrm{t})$, $S(\nu)$ and complete MCF measurement, which can be derived from sequentially acquired two-dimensional intensity images under controlled adjustment of time-delay τ and $\Delta\mathbf{q}$.

5.3 Multi-slice model and light propagation in the object space

In order to derive $h_\mathrm{o}(\mathbf{K}_\mathrm{S},\mathbf{q},\nu)$, the way the light propagates through object space, we need to use appropriate model. This model has to be chosen such that it will allow us to properly investigate the imaging properties of the microscope. We will now derive an expression for the measured mutual coherence function for case of volumetric specimen modeled by the multi-slice approach (see Sec. 4.2). Each slice can be represented by a thin layer such that the scattering potential of n-th layer is described using Eq. (4.6) as

$$f_n(\mathbf{q}_\mathrm{t},z_n) = t_n(\mathbf{q}_\mathrm{t})\delta(z - z_n) \quad (5.3)$$

where $t_n(\mathbf{q}_\mathrm{t})$ is the complex transmission function of the n-th layer and z_n is its axial position. Corresponding scattering function can be derived using Eqs. (4.4) and (4.5) in the following form:

$$\mathcal{S}_n(\mathbf{K}_n,\mathbf{K}_{n-1}) = C_0(\mathbf{K}_n,\mathbf{Q}_n) F_n(\mathbf{Q}_n) = F_n(\mathbf{Q}_n) = T_n(\mathbf{Q}_{n\mathrm{t}}) \mathrm{e}^{-2\pi\mathrm{i}Z_n z_n}, \quad (5.4)$$

where Z_n can be expressed under parabolic approximation as $Z_n \approx (Q_{n\mathrm{t}}^2/2 - \mathbf{Q}_{n\mathrm{t}} \cdot \mathbf{K}_{n\mathrm{t}})/K$. The light that propagates through multi-layer object undertakes a cascade of scattering events and each of them can be characterized by the adaptation of Eq. (4.3)

$$\begin{aligned} U_n(\mathbf{K}_{n\mathrm{t}}) &= \iint_{-\infty}^{\infty} F_n(\mathbf{Q}_n) U_{n-1}(\mathbf{K}_{n\mathrm{t}} - \mathbf{Q}_{n\mathrm{t}}) \mathrm{d}^2\mathbf{Q}_{n\mathrm{t}} \\ &= \iint_{-\infty}^{\infty} T_n(\mathbf{Q}_{n\mathrm{t}}) \mathrm{e}^{-2\pi\mathrm{i}Z_n z_n} U_{n-1}(\mathbf{K}_{n\mathrm{t}} - \mathbf{Q}_{n\mathrm{t}}) \mathrm{d}^2\mathbf{Q}_{n\mathrm{t}} \\ &\approx \iint_{-\infty}^{\infty} T_n(\mathbf{Q}_{n\mathrm{t}}) \mathrm{e}^{-2\pi\mathrm{i}\frac{z_n}{K}(\frac{Q_{n\mathrm{t}}^2}{2} - \mathbf{Q}_{n\mathrm{t}} \cdot \mathbf{K}_{n\mathrm{t}})} U_{n-1}(\mathbf{K}_{n\mathrm{t}} - \mathbf{Q}_{n\mathrm{t}}) \mathrm{d}^2\mathbf{Q}_{n\mathrm{t}}, \end{aligned} \quad (5.5)$$

where $U_n(\mathbf{K}_{n\mathrm{t}})$ is the angular spectrum of a wave calculated in the $z = 0$ plane after the n-th scattering event. The expressions will be further made more compact by using a defocused spatial frequency spectrum $T_n'(\mathbf{Q}_{n\mathrm{t}}) = T_n(\mathbf{Q}_{n\mathrm{t}}) \exp(-\pi\mathrm{i}z_n Q_{n\mathrm{t}}^2)/K$.

Consider a plane wave described by transverse reduced wave vector $\mathbf{K}_\mathrm{S}$ is propagating through the multi-layer object. The angular spectrum of the plane wave is

$$U_0(\mathbf{K}_{0\mathrm{t}}) = \delta(\mathbf{K}_\mathrm{S} - \mathbf{K}_{0\mathrm{t}}). \tag{5.6}$$

The cascade of scattering events will affect the angular spectrum of the wave in the following manner:

$$U_1(\mathbf{K}_{1\mathrm{t}}) = \iint_{-\infty}^{\infty} T_1'(\mathbf{Q}_{1\mathrm{t}}) \mathrm{e}^{2\pi\mathrm{i}\frac{z_1}{K}\mathbf{Q}_{1\mathrm{t}}\cdot\mathbf{K}_{1\mathrm{t}}} \delta(\mathbf{K}_{1\mathrm{t}} - \mathbf{K}_\mathrm{S} - \mathbf{Q}_{1\mathrm{t}}) \mathrm{d}^2\mathbf{Q}_{1\mathrm{t}},$$

$$U_2(\mathbf{K}_{2\mathrm{t}}) = \iint_{-\infty}^{\infty} T_2'(\mathbf{Q}_{2\mathrm{t}}) \mathrm{e}^{2\pi\mathrm{i}\frac{z_2}{K}\mathbf{Q}_{2\mathrm{t}}\cdot\mathbf{K}_{2\mathrm{t}}} \iint_{-\infty}^{\infty} T_1'(\mathbf{Q}_{1\mathrm{t}}) \mathrm{e}^{2\pi\mathrm{i}\frac{z_1}{K}\mathbf{Q}_{1\mathrm{t}}\cdot(\mathbf{K}_{2\mathrm{t}}-\mathbf{Q}_{2\mathrm{t}})} \times \delta(\mathbf{K}_{2\mathrm{t}} - \mathbf{K}_\mathrm{S} - \mathbf{Q}_{2\mathrm{t}} - \mathbf{Q}_{1\mathrm{t}}) \mathrm{d}^2\mathbf{Q}_{1\mathrm{t}} \mathrm{d}^2\mathbf{Q}_{2\mathrm{t}},$$

$$U_3(\mathbf{K}_{3\mathrm{t}}) = \iint_{-\infty}^{\infty} T_3'(\mathbf{Q}_{3\mathrm{t}}) \mathrm{e}^{2\pi\mathrm{i}\frac{z_3}{K}\mathbf{Q}_{3\mathrm{t}}\cdot\mathbf{K}_{3\mathrm{t}}} \times \iint_{-\infty}^{\infty} T_2'(\mathbf{Q}_{2\mathrm{t}}) \mathrm{e}^{2\pi\mathrm{i}\frac{z_2}{K}\mathbf{Q}_{2\mathrm{t}}\cdot(\mathbf{K}_{3\mathrm{t}}-\mathbf{Q}_{3\mathrm{t}})} \iint_{-\infty}^{\infty} T_1'(\mathbf{Q}_{1\mathrm{t}}) \mathrm{e}^{2\pi\mathrm{i}\frac{z_1}{K}\mathbf{Q}_{1\mathrm{t}}\cdot(\mathbf{K}_{3\mathrm{t}}-\mathbf{Q}_{3\mathrm{t}}-\mathbf{Q}_{2\mathrm{t}})} \times \delta(\mathbf{K}_{3\mathrm{t}} - \mathbf{K}_\mathrm{S} - \mathbf{Q}_{3\mathrm{t}} - \mathbf{Q}_{2\mathrm{t}} - \mathbf{Q}_{1\mathrm{t}}) \mathrm{d}^2\mathbf{Q}_{1\mathrm{t}} \mathrm{d}^2\mathbf{Q}_{2\mathrm{t}} \mathrm{d}^2\mathbf{Q}_{3\mathrm{t}}.$$

One can continue applying angular spectrum transformations by each layer all the way to the N-th layer and will obtain after a bit of rearranging following expression:

$$U_N(\mathbf{K}_{N\mathrm{t}}) = \iint_{-\infty}^{\infty} \cdots \iint_{-\infty}^{\infty} \delta(\mathbf{K}_{N\mathrm{t}} - \mathbf{K}_\mathrm{S} - \sum_{n=1}^{N} \mathbf{Q}_{n\mathrm{t}}) \times \prod_{n=1}^{N} T_n'(\mathbf{Q}_{n\mathrm{t}}) \mathrm{e}^{2\pi\mathrm{i}\frac{z_n}{K}\mathbf{Q}_{n\mathrm{t}}\cdot(\mathbf{K}_{N\mathrm{t}}-\sum_{m=n+1}^{N}\mathbf{Q}_{m\mathrm{t}})} \mathrm{d}^2\mathbf{Q}_{n\mathrm{t}}. \tag{5.7}$$

Now suppose that this angular spectrum propagates through an optical system, therefore it gets modified by the pupil function P_O of the objective in a manner described by Eq. (4.8). In order to obtain $h_\mathrm{o}(\mathbf{K}_\mathrm{S},\mathbf{q},\nu)$, Eq. (4.1) is applied:

$$h_\mathrm{o}(\mathbf{K}_\mathrm{S},\mathbf{q},\nu) = \mathrm{e}^{2\pi\mathrm{i}\mathbf{K}_\mathrm{S}\cdot\mathbf{q}} \iint_{-\infty}^{\infty} \cdots \iint_{-\infty}^{\infty} P_\mathrm{O}\left(\mathbf{K}_\mathrm{S} - \sum_{n=1}^{N} \mathbf{Q}_{n\mathrm{t}}\right) \times \prod_{n=1}^{N} T_n'(\mathbf{Q}_{n\mathrm{t}}) \mathrm{e}^{2\pi\mathrm{i}\frac{z_n}{K}\mathbf{Q}_{n\mathrm{t}}\cdot(\mathbf{K}_\mathrm{S}-\sum_{m=1}^{n-1}\mathbf{Q}_{m\mathrm{t}})} \mathrm{e}^{2\pi\mathrm{i}\mathbf{Q}_{n\mathrm{t}}\cdot\mathbf{q}} \mathrm{d}^2\mathbf{Q}_{n\mathrm{t}}. \tag{5.8}$$

Propagation of a plane wave through the reference optical path is straightforward and one obtains the expression

$$h_\mathrm{r}(\mathbf{K}_\mathrm{S},\mathbf{q}-\Delta\mathbf{q},\nu) = P_\mathrm{O}(\mathbf{K}_\mathrm{S}) \mathrm{e}^{2\pi\mathrm{i}\mathbf{K}_\mathrm{S}\cdot(\mathbf{q}-\Delta\mathbf{q})}. \tag{5.9}$$

5.4 Coherence-gating function

Now we will investigate coherence-gating effects interconnected with the spatial coherence properties of the illumination, therefore, quasi-monochromatic light will be assumed. Plugging Eqs. (5.8) and (5.9) describing propagation of a plane wave in the object and reference arm, respectively, into Eq. (5.2) we obtain in the quasi-monochromatic approximation MCF for $\tau = 0$ in the following form

$$\Gamma(\mathbf{q};\Delta\mathbf{q}) \approx \iint_{-\infty}^{\infty} |P_{\mathrm{C}}(\mathbf{K}_{\mathrm{S}})|^2 \iint_{-\infty}^{\infty} \dots \iint_{-\infty}^{\infty} P_{\mathrm{O}}\left(\mathbf{K}_{\mathrm{S}} - \sum_{n=1}^{N} \mathbf{Q}_{nt}\right) \mathrm{e}^{2\pi\mathrm{i}\mathbf{K}_{\mathrm{S}}\cdot\Delta\mathbf{q}} \times \prod_{n=1}^{N} T'_n(\mathbf{Q}_{nt}) \mathrm{e}^{2\pi\mathrm{i}\frac{z_n}{\widetilde{K}}\mathbf{Q}_{nt}\cdot(\mathbf{K}_{\mathrm{S}} - \sum_{m=1}^{n-1}\mathbf{Q}_{mt})} \mathrm{e}^{2\pi\mathrm{i}\mathbf{Q}_{nt}\cdot\mathbf{q}} \mathrm{d}^2\mathbf{Q}_{nt} \mathrm{d}^2\mathbf{K}_{\mathrm{S}}, \quad (5.10)$$

where $\widetilde{K} = 1/\widetilde{\lambda}$ and $\widetilde{\lambda}$ is the central wavelength of light. The diffraction by the imaging objective apertures represented by the P_{O} function does not dramatically affect the spatial coherence of the object-scattered and reference light, therefore, we set $P_{\mathrm{O}} = 1$. The studied object is positioned in the microscope in a way that one of the layers is in focus and for that layer $z_{\mathrm{f}} = 0$, where $\mathrm{f} \in \{1,2,3,\dots,N\}$ is the in-focus layer number. It is, therefore, possible to integrate Eq. (5.10) over $\mathbf{K}_{\mathrm{S}}$ and $\mathbf{Q}_{\mathrm{ft}}$ to obtain

$$\Gamma(\mathbf{q};\Delta\mathbf{q}) \approx \iint_{-\infty}^{\infty} \dots \iint_{-\infty}^{\infty} t_{\mathrm{f}}\left(\mathbf{q}_{\mathrm{t}} + \sum_{n\in N^+} \frac{z_n}{\tilde{K}}\mathbf{Q}_{nt}\right) \mathcal{G}\left(\sum_{n\in N_{\mathrm{f}}} \frac{z_n}{\tilde{K}}\mathbf{Q}_{nt} + \Delta\mathbf{q}\right) \times \prod_{n\in N_{\mathrm{f}}} T'_n(\mathbf{Q}_{nt}) \mathrm{e}^{2\pi\mathrm{i}\frac{z_n}{\tilde{K}}\mathbf{Q}_{nt}\cdot\sum_{m=1}^{n-1}\mathbf{Q}_{mt}} \mathrm{e}^{2\pi\mathrm{i}\mathbf{Q}_{nt}\cdot\mathbf{q}_{\mathrm{t}}} \mathrm{d}^2\mathbf{Q}_{nt}, \quad (5.11)$$

where $N_{\mathrm{f}} = \{1,2,3,\dots,N\} - \{\mathrm{f}\}$, and $N^+ = \{f{+}1, f{+}2, f{+}3, \dots, N\}$. Function $\mathcal{G}(\Delta\mathbf{q}) = \iint_{-\infty}^{\infty} |P_{\mathrm{C}}(\mathbf{K}_{\mathrm{S}})|^2 \exp[2\pi\mathrm{i}(\mathbf{K}_{\mathrm{S}}\cdot\Delta\mathbf{q})]\mathrm{d}^2\mathbf{K}_{\mathrm{S}}$ can be for a diffraction limited condenser with the numerical aperture $\mathrm{NA_C}$ approximated using Bessel function of the first kind as $\mathcal{G}(\Delta\mathbf{q}) = 2J_1(\mu)/\mu$, where $\mu = 2\pi\tilde{K}\mathrm{NA_C}\Delta\mathbf{q}$. For example, using wavelength 650 nm and $\mathrm{NA_C} = 0.5$ the central Airy disk radius is 0.8 µm. This area limits the shift (blurring when integrated) of the t_{f} image caused by scattering in layers with $z_n > 0$. Then, Eq. (5.11) shows that we can understand imaging by multiply scattered light as modulation of in-focus layer image t_{f} by inverse Fourier transforms of expressions $T'_n(\mathbf{Q}_n)\exp(2\pi\mathrm{i}\mathbf{Q}_n\cdot\sum_{m=1}^{n-1}\mathbf{Q}_m z_n/\tilde{K})$ filtered by windowing function $\mathcal{G}$. The narrow central maximum of $\mathcal{G}$ in case of illumination of low spatial coherence results in strong suppression of the defocused layers effect on the t_{f} image. We, therefore, call function $\mathcal{G}$ coherence-gating function (CGF). It ensures that only scattering event cascades with scattering vectors satisfying $\sum z_n\mathbf{Q}_n/\tilde{K} \sim -\Delta\mathbf{q}$ contribute to the image formation process. The degree of the contribution is dictated by $T'_n(\mathbf{Q}_n)$ values.

5.5 Complete mutual coherence function measurement

The interferometric imaging is usually carried out using $\Delta\mathbf{q} = (0,0)$ arrangement. It corresponds to the ballistic light propagation out of the focal plane, see Eq. (5.11). Non-ballistic combinations of $\mathbf{Q}_n$ that satisfy $|\sum z_n \mathbf{Q}_n/\tilde{K} + \Delta\mathbf{q}| \sim 0$ are also allowed. However, in reality, these combinations have weak contributions, especially for weak scattering when functions $|T_n|$ have significant maxima at the zeroth spatial frequency only. Each choice of $\Delta\mathbf{q} \neq (0,0)$ then corresponds to non-ballistic light propagation out of the focal plane. Imaging modes differing by $\Delta\mathbf{q}$ are according to Eq. (5.11) formally equal if no assumption is made about T_n.

The most complete object information can be obtained from the knowledge of the complete MCF. It is equivalent to the set of images acquired for all accessible positions of the CGF, i.e., $\Delta\mathbf{q}$ values.

Chapter 6

Imaging through turbid media

The need to observe biological phenomena beyond the sample surface has led to development of imaging techniques allowing to image in or through turbid media. As the light travels through opaque structures, the light is multiply scattered and is transformed in seemingly random manner. The transformation of the incident wave on the studied specimen is, however, deterministic, therefore, one can reverse the scattering process and obtain information about the original wavefront. The first emerging imaging techniques of that kind were based on the separation of the least scattered (ballistic or first-arriving) light, which is believed to carry the most reliable image information about the specimen, from the diffuse (multiply scattered) component. The principles of the ballistic light separation rely on spatial filtering, polarization gating, time-gating and coherence-gating. The most known spatial filtering techniques is the confocal microscope [66–68], in which the pinhole provides the spatial filtering to exclude the multiply scattered light component. The effectiveness drops dramatically, when the ballistic signal becomes lower than the background and noise. The polarization gating relies on the loss of former polarization state after the light undertakes multiple scattering events. Therefore, it can be partially suppressed by a polarizer. Time gating techniques depend on the capabilities of opto-electronic components, which allow ultrashort pulse generation and gating by optical Kerr gate [69], or separation of the ballistic components from the data acquired by a streak camera [70]. Interferometric methods exploit properties of a light source to coherence gate the ballistic light [7, 12, 71–74]. Imaging in a spatially and temporally low coherent light is analogous to the spatial filtering of a confocal microscope and the time gating, respectively [12, 73].

Besides gating approaches, there are techniques that aim to use also the multiply scattered light. These techniques require the use of coherent light source and extensive computational power. The diffuse optical tomography [75] is based on the diffusion approximation [76], which is used to computationally reconstruct an object, digital phase conjugation and wavefront optimization [77, 78] rely on the wavefront modulation by spatial light modulators or digital micro-mirror devices, transmission matrix approaches require a priori system and scattering medium calibration [33, 79], a deconvolution technique [80] uses measured point spread function (PSF) of the diffuser, where the PSF is valid only in a limited angular memory-effect range [81].

We focus on investigation and development of novel imaging techniques using Coherence-controled holographic microscope (CCHM), based on Leith's and Upatnieks' concept of incoherent holography [5], developed by the Experimental Biophotonics

group. Digital holography techniques provide one major advantage over the most of the previously mentioned imaging methods. Digital holography provides a quantitative phase image (QPI) of transparent specimen. QPI in turbid media, with the use of CCHM, of both model objects [11] and live cells [16] has been demonstrated experimentally. The theory and experiments [12, 13] suggest that CCHM is capable of QPI through a scattering medium using not only ballistic light, but also multiply scattered light, which is in other methods usually suppressed and never used for a direct image formation. Therefore, the focus of this chapter is on the use of multiply scattered light in interferometric systems with partially coherent illumination.

6.1 Imaging through a single strongly scattering layer

6.1.1 Theory

We demonstrate imaging through strongly scattering layer by the adaptation of the multi-slice approach to light propagation modeling in the object. We show that multiply scattered light carries image information of the same quality as the ballistic light even when imaging through strongly scattering media. We demonstrate this claim on the case of quantitative phase imaging. First, we assume a two-layer object. The layer of interest is placed in focus of the objective and imaged through the defocused layer with a random complex transmission function and position $z_1 > 0$. The adaptation of Eq. (5.11) for this case has the following form

$$\Gamma(\mathbf{q}_\mathrm{t};\Delta\mathbf{q}) \;\approx\; \iint t_\mathrm{f}\left(\mathbf{q}_\mathrm{t} + \frac{z_1}{\tilde{K}}\mathbf{Q}_{1\mathrm{t}}\right)\mathcal{G}\left(\frac{z_1}{\tilde{K}}\mathbf{Q}_{1\mathrm{t}} + \Delta\mathbf{q}\right)T_1'(\mathbf{Q}_{1\mathrm{t}})\mathrm{e}^{2\pi\mathrm{i}\mathbf{Q}_{1\mathrm{t}}\cdot\mathbf{q}_\mathrm{t}}\mathrm{d}^2\mathbf{Q}_{1\mathrm{t}}. \quad (6.1)$$

The spatial frequency spectrum of the defocused layer $T_1'(\mathbf{Q}_1)$ is limited by CGF to scattering vectors satisfying relation $\mathbf{Q}_{1\mathrm{t}}z_1/\tilde{K} \sim -\Delta\mathbf{q}$. The inverse Fourier transform of this limited spatial frequency spectrum modulates the image t_f. The produced random modulation can be considered a speckle pattern. Owing to the CGF properties, the speckle size is increasing with the defocus and $\mathrm{NA_C}$. The MCF modulus can serve as an indicator of phase quality because it is in relationship to the root mean square error of phase measurement through inverse proportion (see Chap. 9.4.4 in Ref. [82]), and phase singularities occupy dark speckle areas as modulus approaches zero [83]. Therefore, as the speckle size increases the number of phase singularities is expected to decrease and additive background phase of speckles should be more uniform. As stated before, the blur caused by the shift of t_f by $\mathbf{Q}_{1\mathrm{t}}z_1/\tilde{K}$ is also limited by CGF Airy disk radius, which is inversely proportional to $\mathrm{NA_C}$. Therefore, the change of the imaging mode from ballistic to multiply scattered light made by the change of $\Delta\mathbf{q}$ generally does not affect the size of high-quality phase areas or the resolving power.

6.1.2 Experiment

To demonstrate our predictions in the previous section experimentally we imaged the phase resolution target through an opaque etched glass plate separated by a coverslip, which defines the z_1 distance, and we compare MCF measured for ballistic [$\Delta\mathbf{q} = (0,0)\,\mu$m] and multiply scattered [$\Delta\mathbf{q} = (-2,0)\,\mu$m] light. The modulus images $|\gamma[\mathbf{q};(0,0)]|$[1] displayed in Fig. 6.1(a) and $|\gamma[\mathbf{q};(-2,0)]|$ displayed in Fig. 6.1(c) show that the areas (speckles) with high modulus have similar size and magnitude. Slightly higher modulus values of the scattered light image indicate locally better phase quality compared to the ballistic image. This is supported by corresponding phase images in Fig. 6.1(b) and 6.1(d). As could be predicted, the phase is more continuous in areas of higher modulus. These exemplary images show that the phase quality varies throughout the field of view and for different $\Delta\mathbf{q}$. This indicates that each image from a set acquired for different $\Delta\mathbf{q}$ should provide complementary information. Therefore, we measured MCF for a grid of $\Delta\mathbf{q}$ values with grid sampling based on the Airy disk radius of CGF. We set the sampling to 1 µm for the case of $\mathrm{NA_C} = 0.5$. We adapted an algorithm derived in our preliminary work for phase compensation [14] to combine 121 coherence-gated multiply-scattered-light images synthesizing a high-quality quantitative phase image of the phase resolution target hidden behind the strongly scattering layer, displayed in Fig. 6.1(e).

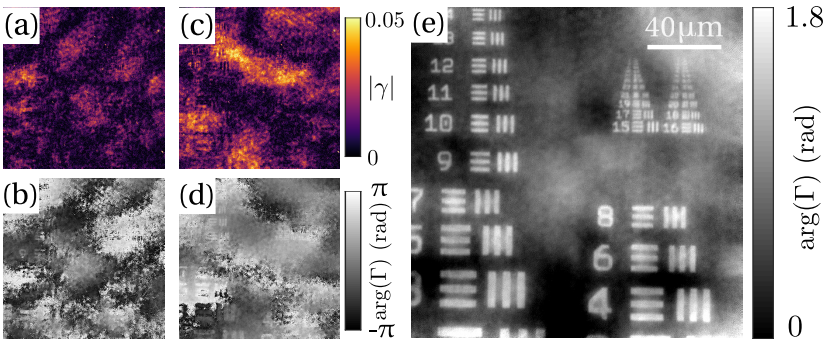

Figure 6.1: Normalized modulus (a), (c) and phase (b), (d) images derived from MCF for $\Delta\mathbf{q} = (0,0)\,\mu$m and $\Delta\mathbf{q} = (-2,0)\,\mu$m for imaging through the etched glass plate. (e) Synthetic quantitative phase image created by a combination of multiply scattered light images. Objectives used 20x/NA = 0.5, $\mathrm{NA_C} = 0.5$. The figure is reused from [84] (see Subsection 6.4).

6.1.3 Image processing - synthesis

The quantitative phase image synthesis starts by acquisition of 121 complex images for different $\Delta\mathbf{q}$ positions. The quality of each image varies throughout the field of view. We have shown, that the combination of the images provides improved image quality before [14], but we have not obtained consistent quality improvement throughout the field of view. Therefore, an improvement of the synthesis procedure was necessary.

[1] We define the normalized modulus as $|\gamma| = |\Gamma|/|\Gamma_{max}|$, where $|\Gamma_{max}|$ stands for the highest achievable value of $|\Gamma|$ in CCHM

Based on the size of high quality areas (we later found out that the size corresponds to the size of the speckle spots [83] in modulus images) we determined the area where the phase should be only linearly modulated, see illustration in Fig. 6.2a. The most important part of image synthesis is the modulus maximization of a coherent superposition of corresponding small parts of complex images. This is done by iterative phase compensating each image fraction separately and then evaluating the modulus of the coherent superposition of the corresponding image fractions. When the phase compensations producing the highest modulus are found, then the synthetic image part is represented by the coherent superposition. We found that the highest modulus means, in the majority of cases, also the best achievable phase quality in that area. This optimization procedure is repeated for each part of the field of view separately, yielding an image similar to the one in Fig. 6.2b, where each area has a slightly different offset phase. To tackle this problem, we choose the areas to optimize with some degree of overlap. The overlap helps us to easily remove the phase offset between two neighboring image tiles. Finally, when the offset is mitigated, a synthetic image with a flat and high-quality phase is obtained, as shown in Fig. 6.1e.

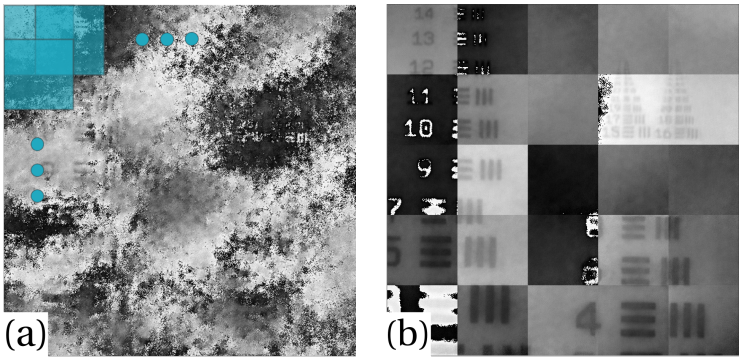

Figure 6.2: (a) Illustration of the choice of areas for optimization. The areas overlap making the follow-up stitching straightforward. (b) Only non-overlapping areas with synthetic high quality phase information.

6.2 Imaging through multiple strongly scattering layers

Preliminary results regarding imaging through multiple strongly scattering layers are presented in this section. We approach the problem by investigating the simplest cases first, and then we gradually increase the complexity of the randomly scattering part of the model sample. The next step after achieving high-quality images through a single strongly scattering layer is the case of imaging through two scattering layers. We imaged the phase resolution target through two strongly etched coverslips with the experimental scheme described in the previous section. Equation (5.11) can be adapted

for this case as

$$\Gamma(\mathbf{q}_\mathrm{t};\Delta\mathbf{q}) \approx \iint\!\!\iint t_\mathrm{f}\left(\mathbf{q}_\mathrm{t}+\frac{z_1}{\tilde{K}}\mathbf{Q}_{1\mathrm{t}}+\frac{z_2}{\tilde{K}}\mathbf{Q}_{2\mathrm{t}}\right)\mathcal{G}\left(\frac{z_1}{\tilde{K}}\mathbf{Q}_{1\mathrm{t}}+\frac{z_2}{\tilde{K}}\mathbf{Q}_{2\mathrm{t}}+\Delta\mathbf{q}\right) \times T_1'(\mathbf{Q}_{1\mathrm{t}})T_2'(\mathbf{Q}_{2\mathrm{t}})\mathrm{e}^{2\pi\mathrm{i}\frac{z_2}{\tilde{K}}\mathbf{Q}_{2\mathrm{t}}\cdot\mathbf{Q}_{1\mathrm{t}}}\mathrm{e}^{2\pi\mathrm{i}(\mathbf{Q}_{1\mathrm{t}}+\mathbf{Q}_{2\mathrm{t}})\cdot\mathbf{q}_\mathrm{t}}\mathrm{d}^2\mathbf{Q}_{1\mathrm{t}}\mathrm{d}^2\mathbf{Q}_{2\mathrm{t}}. \quad (6.2)$$

This equation shows that ambiguity can result from multiple scattering. It is connected to the blur of the image because of ambiguous lateral shift of the image t_f.

We applied the same phase optimization procedure as in the case of imaging only through single scattering layer. The experimental result in Fig. 6.3 shows that the algorithm for phase compensation is working even for imaging through multi-layer scattering object, however, resolving power drops. The resolving power is, in the case of the experimental data shown in Fig. 6.3, reduced also by the fact that the phase resolution target is not in the ideal focal plane of the objective lens. Bringing the specimen into a correct focal plane is in experiments with very strong scattering a difficult task as the ballistic light that provides the feedback about the specimen is significantly corrupted by the scattering.

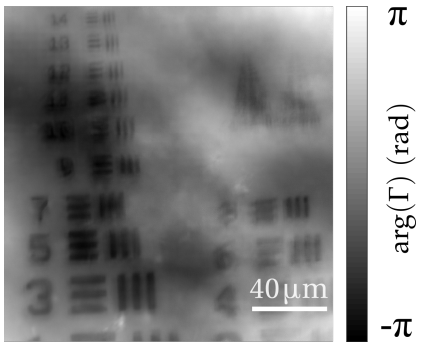

Figure 6.3: Result of the phase optimization algorithm for imaging through two-layer strongly scattering object.

6.3 Preliminary results for imaging through volumetric diffuser

Preliminary results of imaging through volumetric diffuser has been obtained by applying the grid measurement of mutual coherence function of 121 positions to imaging of the phase resolution target through a slab of chicken breast. Images with similar quality to the ballistic image displayed in Fig. 6.4a were recorded for each $\Delta\mathbf{q}$. The same reconstruction algorithm was applied as for the case of the single scattering layer. Even though the algorithm was initially designed for imaging through a single-scattering layer, it provides the synthetic image of improved quality, see Fig. 6.4b. The phase image degradation in Fig. 6.4b is similar to the one with two strongly scattering layers. The image is blurred, which means the resolving power dropped in comparison to the imaging without the diffuser. However, the resolving power drop can be again

accounted to the incorrectly chosen specimen z-direction position. Therefore, in the data presented in Fig. 6.4 the phase resolution target was slightly out of focus.

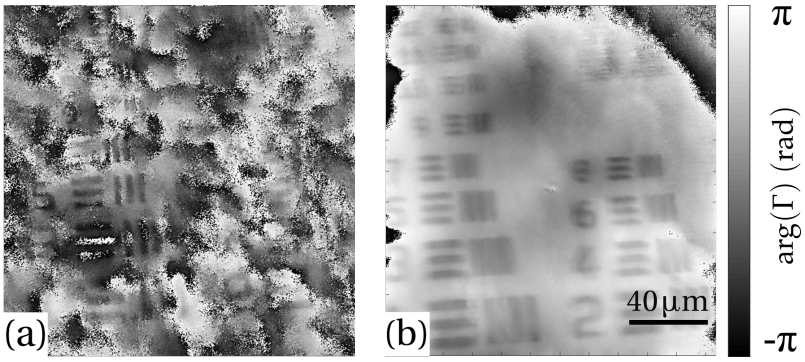

Figure 6.4: (a) Degraded ballistic image when imaging through the slab of chicken breast. (b) Preliminary result of the phase optimization algorithm.

We present higher quality data published in [84] in the following section as we further refined our experimental workflow to achieve precise specimen positioning and control over strength of the volumetric scattering layer.

6.4 Coherence gate manipulation for enhanced imaging through scattering media by non-ballistic light in partially coherent interferometric systems

6.4.1 Motivation

Imaging of biological and medical samples by means of light has been, for a long time, confined to the observation of the sample surface and phenomena happening in its immediate vicinity. An ability to see inside biological objects, such as tissues, is prevented by seemingly opaque structures. Skin, muscles, and other soft tissues appear opaque to the human eye because they strongly scatter light. Strong scattering distorts the image, which strictly limits imaging possibilities. Over the last few decades, extensive research has been carried out to overcome this limitation and non-invasively image objects inside turbid media. An overview of the most significant discoveries and state-of-the-art methods is provided in this chapter's introduction.

The Coherence-controlled holographic microscope we utilize in our research delivers QPI of exceptional quality and can exploit incoherent source properties to coherence gate scattered light [7, 12]. It has already provided an imaging method in numerous successful cancer research projects [16, 54]. However, these works have some experimental limitations. Only a group of adherent cells is observed in a suspension on the glass plate. Studies have shown that cancer cell motility patterns differ in two-dimensional space and in volume fibrous structures [18]. This indicates that dedicated research has to be carried out to discover all cancer cell properties in their natural environment.

However, there are no quantitative, non-invasive, label-free, and real-time methods for this purpose that could provide reliable information about the specimen. This is because of the fact that biological tissues are highly scattering media, and light scattered in out-of-focus planes degrades an image of the object in focus. Some methods provide 3D representation (tomography) of single cells (or a small number of cells) [32, 85], but they do not prove reliable when imaging in strongly scattering media. Therefore, the motivation for this part of this thesis is to develop a method to fill the gap in quantitative imaging through turbid media.

6.4.2 Outcomes

We have shown that it is possible to directly image not only by ballistic light but also by multiply scattered light, which was not shown before. We provide in this thesis and the presented paper [84] a theoretical description of the problem and also an experimental solution. We overcome and extend the limits of existing QPI methods to image through more complex media by utilizing the coherence gate in a counter-intuitive manner. We filter the non-ballistic light by a transversal coherence gate shifting, and we use it for imaging. We developed a novel method that allows imaging through thick and highly turbid media. An integral part of our imaging method is also the image reconstruction software developed in MATLAB environment. Our description of coherence-gated imaging as a spatial coherence measurement allows us to demonstrate the imaging properties of non-ballistic light. Even though the motivation behind our research was to provide imaging techniques to biomedical researchers, the obtained theoretical description shows the interconnection with other disciplines dealing with light source characterization, crystal structure determination, or quantification of light diffusion parameters. Therefore, the outcomes might prove very valuable in future not only to biomedical researchers.

6.4.3 Article 1

The article **Coherence gate manipulation for enhanced imaging through scattering media by non-ballistic light in partially coherent interferometric systems** was published in **Optics Letters** (2021 Impact factor: 3.56, Q1 in Optics) in September 2021.

Optics Letters

Coherence gate manipulation for enhanced imaging through scattering media by non-ballistic light in partially coherent interferometric systems

MIROSLAV ĎURIŠ[1,*] AND RADIM CHMELÍK[1,2]

[1]CEITEC—Central European Institute of Technology, Brno University of Technology, Purkyňova 656/123, 61200 Brno, Czech Republic
[2]Institute of Physical Engineering, Faculty of Mechanical Engineering, Brno University of Technology, Technická 2896/2, 61669 Brno, Czech Republic
*Corresponding author: miroslav.duris@ceitec.vutbr.cz

Received 25 May 2021; revised 27 July 2021; accepted 11 August 2021; posted 11 August 2021 (Doc. ID 432484); published 7 September 2021

Coherence gating is typically exploited for imaging through disordered media by least-scattered (ballistic) light. Ballistic light-based approaches produce clear images only when the proportion of ballistic to multiply scattered (non-ballistic) light is relatively high. To overcome this limitation, we counterintuitively utilize the coherence gate to image by the non-ballistic light, enabling us to retrieve information missing in the ballistic image. We show that non-ballistic images acquired by transversal coherence gate shifting have image quality and spatial resolution comparable to the ballistic image. Combining images for different coherence gate positions, we synthesize an image of quality superior to ballistic light approaches. We experimentally demonstrate our concept on quantitative phase imaging through biological tissue.

https://doi.org/10.1364/OL.432484

One of the principal challenges in biomedical research is imaging through turbid media [1]. Optical imaging methods tackling this problem strive to minimize the effect of the random multiply scattered light [2] or to control it optically or digitally [3]. The first group of methods increasingly utilize the coherence-gating effect [4]. This filtering phenomenon arises from a limited spatial and temporal coherence of illumination. Therefore, it is intrinsic to partially coherent optical systems. Imaging techniques that use the coherence gate for separating only the ballistic (scattered by the object only) light from the unwanted multiply scattered (non-ballistic) light include optical coherence tomography and microscopy [5], achromatic digital holography [6,7], Horn microscopy [8], or white-light diffraction tomography [9]. In comparison to the coherent one, partially coherent illumination provides numerous advantageous imaging properties such as higher spatial resolution, depth sectioning, and speckle noise reduction [7]. However, the use of coherent beams prevails owing to their convenient implementation and simple description allowing inverse modeling [10].

Partially coherent beams require the complete description of at least four-dimensional functions, making them less convenient for computational imaging [11]. The most common representations include cross-spectral density, mutual coherence function (MCF), and phase-space distributions [11]. Their experimentally challenging measurement is redeemed by being irreplaceable in illumination source characterization [12], crystal structure determination [13], three-dimensional object reconstruction [14], object tracking behind opaque structures [15], or quantification of light diffusion parameters [16]. Setting coherence gate to the position separating only the ballistic light makes imaging techniques [5–9] unable to measure complete MCF.

In this Letter, we demonstrate the principal importance of the complete MCF measurement for partially coherent interferometric imaging of objects with strongly scattering surroundings. We show that MCF describing the cross correlation between the object and reference beam comprises the image information formed by both the ballistic and non-ballistic light. In addition to the ballistic image, we extract from the complete MCF by coherence gate manipulation images formed by the non-ballistic light fractions. If the turbid medium is rather weakly scattering, the ballistic light contains almost unaltered specimen information. However, when the scattering is stronger, and the ballistic to multiply scattered light ratio is poor, the complementary non-ballistic light components can significantly improve insufficient ballistic imaging. Combining all of the scattered light components, we demonstrate high-quality quantitative phase imaging throughout the entire field of view (FOV), even in situations with a completely corrupted ballistic images.

To demonstrate the ideas mentioned above, we begin with a theoretical description of the MCF measurement in the optical setup used for the experimental part. We used a coherence-controlled holographic microscope (CCHM) [7], commercially available as Telight Q-Phase. The optical setup (see Fig. 1) consists of optically equivalent object and reference arms, with a scattering object present in the object arm. The diffraction grating (DG) is implemented according to principles proposed by Leith [6] in the reference arm to ensure a formation of an

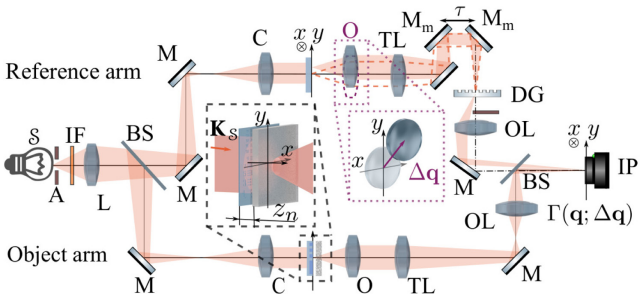

Fig. 1. Optical setup of the coherence-controlled holographic microscope: $\mathcal{S}$, light source; A, aperture; IF, interference filter; L, relay lens; BS, beam splitters; M, mirrors; M_m, movable mirrors; C, condensers; O, objective lenses; TL, tube lenses; DG, diffraction grating; OL, output lenses; IP, interference plane.

off-axis hologram in the interference plane (IP). The fundamental image properties depend on the parameters of condensers (C) and objective lenses (O) in couples with tube lenses (TL) characterized by the pupil functions (see Ref. [17]) P_C and P_O, respectively. The axes x, y of the object space Cartesian coordinate system lie in the object plane, and the axis z points in the optical axis direction (see Fig. 1). The position of a point in the image plane is specified by the coordinates of the optically conjugated point $\mathbf{q} = (x, y)$ in the object plane. A halogen lamp $\mathcal{S}$ filtered by an interference filter (IF, central wavelength 650 nm and 10 nm full width at half-maximum) provides thermal, spatially broad, and quasi-monochromatic illumination. It is imaged to the object focal planes of the C forming Köhler illumination. The transverse wave vector coordinates $\mathbf{K}_\mathcal{S}$ of a plane wave behind C are proportional to the respective source point coordinates. For this reason, the source properties can be characterized by a function of $\mathbf{K}_\mathcal{S}$. We use reduced wave vector notation $|\mathbf{K}| = 1/\lambda$, where λ is the wavelength of light, and $\mathbf{K} = (\mathbf{K}_t, K_z) = (K_x, K_y, K_z)$, where $\mathbf{K}_t$ is the transverse wave vector, and $K_z = \sqrt{|\mathbf{K}|^2 - |\mathbf{K}_t|^2}$.

From the time-averaged intensity measurements in IP, we digitally retrieve the cross-correlation information between object-scattered and reference light by a carrier removal in the Fourier plane [7]. The cross-correlation term dependent on the transversal displacement $\Delta\mathbf{q} = (\Delta x, \Delta y)$ and relative time-delay τ of the object-scattered and reference field can be understood as their MCF $\Gamma(\mathbf{q}, \mathbf{q} - \Delta\mathbf{q}, \tau)$. Therefore, interferometric imaging for a given time-delay τ and transverse displacement $\Delta\mathbf{q}$ is a partial MCF measurement. Modulus and phase image for particular $\Delta\mathbf{q}$ and τ is obtained as modulus and argument of Γ, respectively. The acquisition of MCF (complex-valued images) for all accessible $\Delta\mathbf{q}$ and τ makes the measurement complete. The complete MCF is available to every partially coherent interferometric system, where the reference-field position and optical path difference can be manipulated. In our system, it is controlled by the reference arm elongation and objective shift (see Fig. 1). We further show that the most common arrangement of imaging setups fixed at $\tau = 0$ and $\Delta\mathbf{q} = (0, 0)$ correspond to ballistic light imaging, while the MCF at $\Delta\mathbf{q} \neq (0, 0)$ carries significant amounts of information about the non-ballistic imaging processes. As the coherence-gating effect is mainly related to the low spatial coherence in transmitted-light systems, while temporal coherence has the influence of the second order [18], we discuss only manipulation with $\Delta\mathbf{q}$ in this Letter. Given a complete spatial source incoherence, the expression for the measured MCF for $\tau = 0$ has, according to Eq. (4.4-31) in Ref. [19], the form

$$\Gamma(\mathbf{q}, \mathbf{q} - \Delta\mathbf{q}) = \iint_{-\infty}^{\infty} |P_C(\mathbf{K}_\mathcal{S})|^2 \times h_o(\mathbf{K}_\mathcal{S}, \mathbf{q}) h_r^*(\mathbf{K}_\mathcal{S}, \mathbf{q} - \Delta\mathbf{q}) \mathrm{d}^2\mathbf{K}_\mathcal{S}, \quad (1)$$

where $h_o(\mathbf{K}_t, \mathbf{q})$ and $h_r(\mathbf{K}_t, \mathbf{q} - \Delta\mathbf{q})$ describe the propagation of a plane wave $\mathbf{K}_t$ through the object and reference arm, respectively.

Light propagation within the system is derived similarly to Ref. [17] using the multi-slice model of a volumetric specimen [20]. We assume no backscattering and only paraxial propagation. The object is formed by a set of layers with spatial frequency spectra $T_n(\mathbf{Q}_n)$ in axial positions z_n of the object space, where $n \in N = \{A \ldots -2, -1, 0, 1, 2 \ldots B\}$. Negative n refers to $z_n < 0$, positive n refers to $z_n > 0$, and $n = 0$ denotes the in-focus layer. The propagation in object path is described by

$$h_o(\mathbf{K}_t, \mathbf{q}) = e^{2\pi i \mathbf{q}\cdot\mathbf{K}_t} \int \ldots \int P_O\left(\mathbf{K}_t + \sum_n \mathbf{Q}_n\right) \times \prod_n T'_n(\mathbf{Q}_n) e^{2\pi i \mathbf{Q}_n \cdot \left[\left(\mathbf{K}_t + \sum_m \mathbf{Q}_m\right) z_n/K + \mathbf{q}\right]} \mathrm{d}^2\mathbf{Q}_n, \quad (2)$$

where $T'_n(\mathbf{Q}_n) = T_n(\mathbf{Q}_n) \exp(\pi i z_n |\mathbf{Q}_n|^2/K)$ and $\mathbf{Q}_n = (X_n, Y_n)$ is the scattering vector in the nth layer. The integrals go from $-\infty$ to ∞. The sum in the exponential indexed by $m \in N$ goes only through $m < n$. The reference-field propagation can be described by $h_r(\mathbf{K}_t, \mathbf{q} - \Delta\mathbf{q}) = P_O(\mathbf{K}_t) \exp\{2\pi i [\mathbf{K}_t \cdot (\mathbf{q} - \Delta\mathbf{q})]\}$. If we neglect diffraction by objective apertures setting $P_O = 1$, then it is evident how illumination source properties affect MCF measurement and give rise to the coherence-gating effect. Plugging Eq. (2) into Eq. (1), one obtains MCF in the following form:

$$\Gamma(\mathbf{q}; \Delta\mathbf{q}) \approx \int \ldots \int t_0\left(\mathbf{q} + \sum_{n \in N^+} \frac{z_n}{K} \mathbf{Q}_n\right) \times \mathcal{G}\left(\sum_{n \in N_0} \frac{z_n}{K} \mathbf{Q}_n + \Delta\mathbf{q}\right) \times \prod_{n \in N_0} T'_n(\mathbf{Q}_n) e^{2\pi i \mathbf{Q}_n \cdot [\sum_m \mathbf{Q}_m z_n/K + \mathbf{q}]} \mathrm{d}^2\mathbf{Q}_n, \quad (3)$$

where $N^+ = \{1, 2, 3 \ldots B\}$ and $N_0 = N - \{0\}$. Function $\mathcal{G}(\Delta\mathbf{q}) = \iint_{-\infty}^{\infty} |P_C(\mathbf{K}_\mathcal{S})|^2 \exp[2\pi i (\mathbf{K}_\mathcal{S} \cdot \Delta\mathbf{q})] \mathrm{d}^2\mathbf{K}_\mathcal{S}$ can be for a diffraction-limited C with the numerical aperture NA_C approximated using a Bessel function of the first kind as $\mathcal{G}(\Delta\mathbf{q}) = 2J_1(\mu)/\mu$, where $\mu = 2\pi K \mathrm{NA}_C \Delta\mathbf{q}$. For example, using a wavelength of 650 nm and $\mathrm{NA}_C = 0.5$, the central Airy disk radius is 0.8 μm. Equation (3) shows that, in the case of imaging by multiply scattered light, MCF for each $\Delta\mathbf{q}$ can be understood as an image t_0 of the in-focus layer modulated by inverse Fourier transforms of expressions

$T'_n(\mathbf{Q}_n)\exp(2\pi i\mathbf{Q}_n\cdot\sum_m \mathbf{Q}_m z_n/K)$ filtered by a windowing function $\mathcal{G}$. The narrow central maximum of $\mathcal{G}$ ensures that only the scattering event cascades, satisfying $\sum z_n\mathbf{Q}_n/K \approx -\Delta\mathbf{q}$ to contribute to the image formation process, and also limits its blurring of t_0 for $N_0 = N^+$. $T'_n(\mathbf{Q}_n)$ values dictate the degree of the contribution. Therefore, we call the function $\mathcal{G}$ a coherence-gating function (CGF).

Equation (3) also clarifies the CGF setting for the ballistic and non-ballistic imaging mode. Measuring MCF for CGF position $\Delta\mathbf{q} = (0, 0)$ corresponds to $|\mathbf{Q}_n| = 0, \forall n \neq 0$, i.e., to the ballistic light imaging. It is evident that non-ballistic combinations of $\mathbf{Q}_n$ that satisfy $|\sum z_n\mathbf{Q}_n/K| \approx 0$ also affect the ballistic image. This effect is negligible only for weakly scattering surroundings. Otherwise, the image will not be a perfect representation of the object in focus. The same also applies for MCF measurement for $\Delta\mathbf{q} \neq (0, 0)$, the non-ballistic light imaging. Both ballistic and non-ballistic imaging obey the same equation, Eq. (3), and differ only by the parameter $\Delta\mathbf{q}$, so we treat them equally.

It is instructive to demonstrate the principles first on a simplified case of imaging through a single scattering layer. We show that when scattering by the surrounding medium is strong, non-ballistic light carries image information of the same quality as the ballistic light and that the images formed are complementary. We demonstrate this claim on the case of quantitative phase imaging of a phase resolution target through an opaque etched glass plate separated by a coverslip, which defines the z_1 distance. For this experiment, we used 20x objectives with NA = 0.5, and the illumination aperture was $\mathrm{NA}_C = 0.5$. The layer of interest was placed in the focus of the objective and imaged through the strongly scattering layer. We chose the scattering strength of the etched layer such that a bright-field image with partially coherent illumination, see Fig. 2(a), does not show any part of the resolution target. More importantly, not even coherence gated ballistic light provides high-enough quality throughout the whole FOV, see ballistic modulus and phase images in Figs. 2(c) and 2(d). We have measured the complete MCF with [purple curve in Fig. 2(b)] and without (orange curve) the scattering layer, and we display the normalized modulus $|\gamma_R| = |\Gamma_R|/|\Gamma_{\max}|$ for a point R [see Fig. 2(c)] against Δx in Fig. 2(b). Here, $|\Gamma_{\max}|$ stands for the highest possible value of $|\Gamma|$ in CCHM. In general, as the modulus drops, the quality of the image derived at that point of the MCF degrades. There are two reasons, the MCF modulus is in relationship to the root mean square error of phase measurement through inverse proportion (see Chap. 9.4.4 in Ref. [21]), and phase singularities occupy near-zero modulus areas [22]. Therefore, the MCF modulus serves as an indicator of phase quality. Regarding the curves in Fig. 2(b), one can expect to acquire some information only in Δx points with a high modulus. It is evident that when imaging only a single planar object the complete MCF measurement (orange curve) does not add any information to the ballistic mode. However, when we image through at least one additional strongly scattering layer, non-ballistic parts of the MCF contain valuable information. We adapt Eq. (3) for this case to facilitate further discussion:

$$\Gamma(\mathbf{q};\,\Delta\mathbf{q}) \approx \iint t_0\left(\mathbf{q}+\frac{z_1}{K}\mathbf{Q}_1\right)\mathcal{G}\left(\frac{z_1}{K}\mathbf{Q}_1+\Delta\mathbf{q}\right) \times T'_1(\mathbf{Q}_1)e^{2\pi i\mathbf{Q}_1\cdot\mathbf{q}}\mathrm{d}^2\mathbf{Q}_1. \quad (4)$$

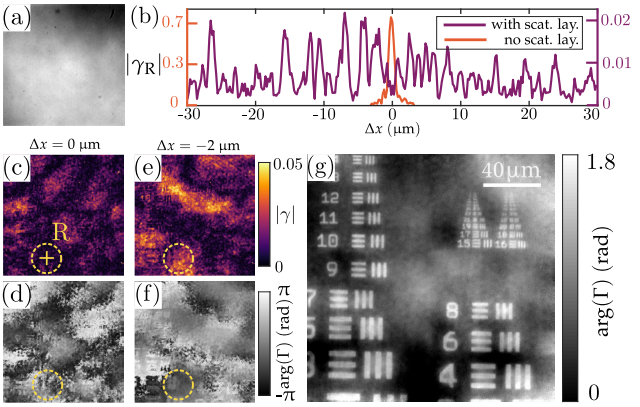

Fig. 2. Results for imaging of the phase resolution target through an etched glass plate. (a) Bright-field ballistic imaging mode. (b) Normalized modulus of measured MCF against Δx at point R. (c), (e) Modulus and (d), (f) phase images derived from MCF for $\Delta\mathbf{q} = (0, 0)$ μm (ballistic light image) and $\Delta\mathbf{q} = (-2, 0)$ μm for imaging through the etched glass plate. (g) Synthetic quantitative phase image created by a combination of non-ballistic images. Objectives used 20x/NA = 0.5, $\mathrm{NA}_C = 0.5$.

This equation suggests that each part of the MCF acquired for different $\Delta\mathbf{q}$ can be interpreted as an image t_0 of the resolution target shifted by $\Delta\mathbf{q}$. The scattering on the etched layer manifests itself as modulation by the inverse Fourier transform of the spatial frequency spectrum $T'_1(\mathbf{Q}_1)$. CGF limits this spectrum only to scattering vectors satisfying relation $\mathbf{Q}_1 z_1/K \approx -\Delta\mathbf{q}$. The produced modulation appears to be random with high and low modulus areas. The stronger coherence-gating effect reduces more the range of contributing $T'_1(\mathbf{Q}_1)$ spatial frequencies, and, therefore, the size of the high-modulus areas increases. This reduces the number of phase singularities and makes the additive phase from out-of-focus scattering more uniform. As the CGF allows a finite range of scattering layer components to contribute, the image is blurred. The blur is limited by CGF Airy disk radius, which defines the transversal spatial resolution. The CGF width (0.8 μm) can be measured when no object is present; see peak width in Fig. 2(b). We can conclude that the change of the imaging mode to non-ballistic light generally does not affect the size of high-quality phase areas or the resolution. Therefore, neither of the imaging modes is inferior.

We also use this experiment to demonstrate the complementary nature of non-ballistic images. Consider, for example, a small region of the FOV marked by the yellow dashed ring in Figs. 2(c)–2(f). One can see that information about the object is missing in the ballistic light [see the zero modulus in Fig. 2(c) and the random phase in Fig. 2(d)]. The shape of the complete MCF in Fig. 2(b) indicates that the information might be present for particular $\Delta\mathbf{q} \neq (0, 0)$ with a higher modulus. We show the image acquired for $\Delta\mathbf{q} = (-2, 0)$ μm, see Figs. 2(e) and 2(f), to support this statement. The modulus is higher in the circled area, and the phase information is present. These findings suggest that a combination of images acquired for different $\Delta\mathbf{q}$ can provide information about the whole FOV.

We designed a method to reconstruct a high-quality synthetic image throughout the whole FOV from the measured MCF. We acquired images for an 11 × 11 grid of $\Delta\mathbf{q}$ centered at the ballistic position with the sampling of 1 μm, based on the Airy disk radius of CGF to avoid overlap. Adapting our preliminary work

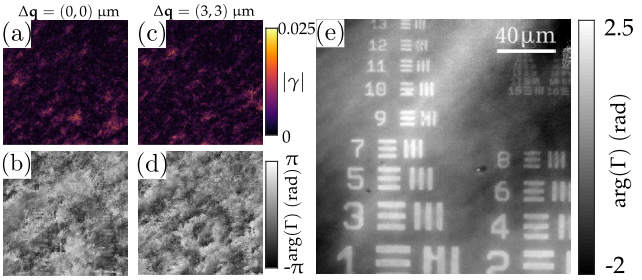

Fig. 3. Results for imaging through a slab of chicken breast. (a), (c) Modulus and (b), (d) phase images derived from the MCF for $\Delta\mathbf{q} = (0, 0)$ μm and $\Delta\mathbf{q} = (3, 3)$ μm. (e) Synthetic quantitative phase image created by a combination of non-ballistic images. Objectives used 20x/NA = 0.5, $NA_C = 0.3$.

[23], we start by shifting images to their correct positions based on the CGF position $\Delta\mathbf{q}$. Then, corresponding small regions of all 121 images are phase-corrected for linear phase distortions with the objective to maximize the modulus of their coherent superposition. Then, the phase quality is after superposition significantly improved. A full FOV image is stitched together from smaller overlapping areas producing a high-quality quantitative phase image, and the result is displayed in Fig. 2(g). The phase quality is consistent throughout the FOV and significantly improved in comparison to the ballistic light phase image in Fig. 2(d). The spatial resolution is also in agreement with the prediction. The smallest resolvable elements of the resolution target in Fig. 2(g) are 0.81 μm wide, which corresponds to the CGF width. It is important to note that coherent averaging of 121 ballistic images in this static case reduces low-contrast hologram noise but does not deal with the phase jumps and singularities, which are the main cause of image degradation. When the scattering medium is highly dynamic, averaging a high ballistic image number can provide similar image improvement as in Fig. 2(g) [24].

To verify the feasibility of our approach for imaging through turbid biological media, we carried out an experiment with a slab of chicken breast instead of the etched glass layer. The chicken breast was cut into a slab of thickness from 1 to 2 mm and squeezed between two coverslips separated by 0.8 mm thick ring. The chicken muscle tissue has a transport mean free path of 1.25 mm, mean free path of 43.7 μm, and an anisotropy factor of 0.965 [25]. One can see that neither ballistic [Figs. 3(a) and 3(b)] nor non-ballistic [Figs. 3(c) and 3(d)] images sufficiently reproduce the phase resolution target. We employed the same procedure as for the imaging through the etched glass plate. Even in this case it was possible to reconstruct a full FOV synthetic image [Fig. 3(e)] with high phase quality and spatial resolution.

In this Letter, we first demonstrated the equivalence between the complete MCF measurement and coherence-gated imaging for all accessible coherence gate positions in partially coherent interferometric systems. In the case of imaging through strongly scattering media, we showed that the coherence gate manipulation enables imaging by fractions of non-ballistic (multiply scattered) light and that it carries complementary information to the ballistic image. Finally, we proved the immense value of using coherence-gated non-ballistic light by proposing a method for significant improvement of quantitative phase imaging quality through strongly scattering media. Our outcomes benefit not only CCHM but a wide range of partially coherent interferometric systems. A minor alteration of imaging systems [6–10] would allow them to measure the complete MCF and extend their imaging capabilities in biomedical research.

Funding. Vysoké Učení Technické v Brně (VUT-J-20-6537, FSI-S-20-6353); Ministerstvo Školství, Mládeže a Tělovýchovy (LM2018129); Grantová Agentura České Republiky (21-01953S).

Acknowledgment. M. Ď. is grateful for the support provided by the Brno Ph.D. talent.

Disclosures. R. C.: Telight (P,R).

Data Availability. Data underlying the results presented in this Letter are not publicly available at this time but may be obtained from the authors upon reasonable request.

REFERENCES

1. S. Yoon, M. Kim, M. Jang, Y. Choi, W. Choi, S. Kang, and W. Choi, Nat. Rev. Phys. **2**, 141 (2020).
2. S. Kang, S. Jeong, W. Choi, H. Ko, T. D. Yang, J. H. Joo, J.-S. Lee, Y.-S. Lim, Q.-H. Park, and W. Choi, Nat. Photonics **9**, 253 (2015).
3. I. M. Vellekoop and A. P. Mosk, Opt. Lett. **32**, 2309 (2007).
4. O. Salhov, G. Weinberg, and O. Katz, Opt. Lett. **43**, 5528 (2018).
5. J. A. Izatt, E. A. Swanson, J. G. Fujimoto, M. R. Hee, and G. M. Owen, Opt. Lett. **19**, 590 (1994).
6. E. N. Leith and J. Upatnieks, J. Opt. Soc. Am. **57**, 975 (1967).
7. T. Slabý, P. Kolman, Z. Dostál, M. Antoš, M. Lošťák, and R. Chmelík, Opt. Express **21**, 14747 (2013).
8. D. Zicha and G. A. Dunn, J. Microsc. **179**, 11 (1995).
9. T. Kim, R. Zhou, M. Mir, S. D. Babacan, P. S. Carney, L. L. Goddard, and G. Popescu, Nat. Photonics **8**, 256 (2014).
10. Y. Cotte, F. Toy, P. Jourdain, N. Pavillon, D. Boss, P. Magistretti, P. Marquet, and C. Depeursinge, Nat. Photonics **7**, 113 (2013).
11. S. B. Mehta and C. J. R. Sheppard, J. Opt. Soc. Am. A **35**, 1272 (2018).
12. Y. Shao, X. Lu, S. Konijnenberg, C. Zhao, Y. Cai, and H. P. Urbach, Opt. Express **26**, 4479 (2018).
13. E. Wolf, Phys. Rev. Lett. **103**, 075501 (2009).
14. D. L. Marks, R. A. Stack, D. J. Brady, D. C. Munson, and R. B. Brady, Science **284**, 2164 (1999).
15. J. A. Newman, Q. Luo, and K. J. Webb, Phys. Rev. Lett. **116**, 073902 (2016).
16. A. Badon, D. Li, G. Lerosey, A. Claude Boccara, M. Fink, and A. Aubry, Optica **3**, 1160 (2016).
17. R. Chmelik, M. Slaba, V. Kollarova, T. Slaby, M. Lostak, J. Collakova, and Z. Dostal, Prog. Opt. **59**, 267 (2014).
18. E. N. Leith, W.-C. Chien, K. D. Mills, B. D. Athey, and D. S. Dilworth, J. Opt. Soc. Am. A **20**, 380 (2003).
19. L. Mandel and E. Wolf, *Optical Coherence and Quantum Optics* (Cambridge University, 1995).
20. U. S. Kamilov, I. N. Papadopoulos, M. H. Shoreh, A. Goy, C. Vonesch, M. Unser, and D. Psaltis, Optica **2**, 517 (2015).
21. J. W. Goodman, *Statistical Optics*, 2nd ed. (Wiley, 2015).
22. N. Shvartsman and I. Freund, Opt. Commun. **117**, 228 (1995).
23. R. Chmelík, M. Duris, and L. Štrbková, Proc. SPIE **10677**, 263 (2018).
24. A. V. Kanaev, A. T. Watnik, D. F. Gardner, C. Metzler, K. P. Judd, P. Lebow, K. M. Novak, and J. R. Lindle, Opt. Lett. **43**, 3088 (2018).
25. W. F. Cheong, S. A. Prahl, and A. J. Welch, IEEE J. Quantum Electron. **26**, 2166 (1990).

Chapter 7

Coherence-encoded structured illumination

The use of structured illumination is a well-known methodology that is used for 3D surface measurement [86], as an optical sectioning method to reject out-of-focus light contributions [87], as a tool to improve the lateral and axial resolution of an imaging system and as a method allowing optical diffraction tomography [88]. In its current form, structured illumination microscopy (SIM) aims mainly at improving the resolution limits of fluorescence microscopy [89]. An implementation of the reliable and easy to use structured illumination into coherent systems allowing sub-diffraction limited resolution or improving optical sectioning properties would be very welcomed by the QPI community and bio-medical researchers, because it would provide unprecedented throughput to their experiments and observations

Numerous techniques in the field of quantitative phase imaging have partially addressed resolution enhancement beyond the diffraction limit. Several methods employ sequential oblique coherent beam illumination paired with holographic detection [90–93]. These techniques capture images that contain high-frequency components of the object spectrum, which are downshifted due to oblique illumination, and then digitally synthesize an image with effectively larger numerical aperture of the system. Structured illumination microscopy adapted for coherent modalities like QPI also utilizes similar principles but the illumination of the specimen is simultaneous with multiple oblique beams [94, 95]. Surprisingly, even random speckle field illumination has been shown to enhance resolution [96, 97]. It is important to note that manipulating the illumination is not the only way to achieve sub-diffraction limited resolution. Researchers have demonstrated that by inverting light propagation through scattering media using a pre-recorded transmission matrix [34], synthetic aperture QPI can be produced. Another set of techniques that aim to achieve sub-diffraction limited resolution is lens-free techniques [98–100]. Additionally, it was shown that digital in-line holographic microscopy (member of lens-free techniques), can reach significantly improved resolving power through the application of synthetic aperture approaches [101, 102]. However, the practical use of lens-free on-chip techniques is limited due to the requirement of placing the specimen very close to the imaging sensor [98]. On the other hand, Fourier ptychographic microscopy (FPM) [103,104], which has gained attention recently due to its simple implementation, offers a promising method to achieve high spatial bandwidth. FPM does not rely on holographic detection but instead acquires a series

of intensity images for different oblique illuminations. The main drawback of FPM lies in its reliance on iterative phase retrieval algorithms [105] to stitch the recorded images in Fourier space, which affects the quantitative phase image quality. In general, all synthetic aperture methods trade off certain degrees of freedom in the system to expand the achievable spatial frequency bandwidth of the image [106]. For instance, one approach involves utilizing the dynamic range of a camera to multiplex multiple off-axis holograms corresponding to different oblique illumination directions into a single measurement, thereby providing a single-shot synthetic aperture method [107–109]. However, this elegant approach may result in a decrease in the quality of the quantitative phase image [110].

It is important to note where CCHM stands in the context of the techniques mentioned earlier for resolution improvement. Instead of using a conventional coherent point source for illumination, CCHM utilizes a spatially broad thermal source within the Köhler illumination configuration. As a result, the specimen is illuminated not by a single coherent wave (used in all the standard holographic systems), but by numerous mutually incoherent plane waves simultaneously. The size of the illumination cone is directly related to the numerical aperture of the condenser lens. Therefore, the spatial frequency bandpass of the CCHM imaging system is twice as wide when using a broad illumination source compared to a point source [7].

7.1 Preliminary results with linear diffraction grating

We approach SIM in CCHM by providing structured illumination by multiple-scattering events on known objects placed in the object arm. First, we show that multiply scattered light can be effectively separated from the complete mutual coherence function measurement and then we show that the multiply scattered light experiences properties of structured illumination.

First, we image a phase resolution target that is illuminated through two identical transmission diffraction gratings positioned in $z_{-2}, z_{-1} < 0$ with spatial frequency $150\,\mathrm{mm}^{-1}$ and groves oriented in the x-axis direction, see Fig. 7.1(a). This setup can be considered a three-layer object. We measured complete MCF and we display in Fig. 7.1(d) its normalized modulus $|\gamma_\mathrm{P}| = |\Gamma_\mathrm{P}|/|\Gamma_{max}|$ for a point P [see Fig. 7.1(c)] against Δy, Δx is set to 0. Here $|\Gamma_{max}|$ stands for the highest achievable value of $|\Gamma|$ in CCHM. The plotted function experiences several easily distinguishable peaks. The origin of the peaks can be explained based on the following adaptation of Eq. (5.11)

$$\Gamma(\mathbf{q};\Delta\mathbf{q}) \approx t_\mathrm{f}(\mathbf{q}_\mathrm{t}) \iint \iint \mathcal{G}\left(\frac{z_{-2}}{\tilde{K}}\mathbf{Q}_{-2\mathrm{t}} + \frac{z_{-1}}{\tilde{K}}\mathbf{Q}_{-1\mathrm{t}} + \Delta\mathbf{q}\right) \times T'_{-2}(\mathbf{Q}_{-2\mathrm{t}})T'_{-1}(\mathbf{Q}_{-1\mathrm{t}})\mathrm{e}^{2\pi\mathrm{i}(\mathbf{Q}_{-1\mathrm{t}}\cdot\mathbf{Q}_{-2\mathrm{t}})z_{-1}/\tilde{K}}\mathrm{e}^{2\pi\mathrm{i}(\mathbf{Q}_{-2\mathrm{t}}+\mathbf{Q}_{-1\mathrm{t}})\cdot\mathbf{q}_\mathrm{t}}\mathrm{d}^2\mathbf{Q}_{-1\mathrm{t}}\mathrm{d}^2\mathbf{Q}_{-2\mathrm{t}}. \quad (7.1)$$

The gratings have dominant 0^{th}, 1^{st} and -1^{st} diffraction orders, with which we can associate scattering vectors $\mathbf{Q}^\mathrm{o} = (0{,}0)$, $\mathbf{Q}^+ = (0{,}150)\,\mathrm{mm}^{-1}$ and $\mathbf{Q}^- = (0, -150)\,\mathrm{mm}^{-1}$,

respectively. The splitting ratio between diffraction orders is described by $T'_n(\mathbf{Q}_n)$. The 0^{th} diffraction orders of both gratings correspond to ballistic light propagation, and ballistic image of the phase resolution target is obtained by measuring MCF for $\Delta y = 0$. According to Eq. (7.1), CGF with radius 1.3 µm ($\text{NA}_\text{C} = 0.3$) ensures that no other diffraction orders significantly affect MCF, therefore we get $\Gamma[\mathbf{q},(0,0)] \approx t_\text{f}(\mathbf{q})T'_{-2}(\mathbf{Q}^\text{o})T'_{-1}(\mathbf{Q}^\text{o})$. The other peaks in Fig. 7.1(d) with $\Delta y \neq 0$ correspond to multi-

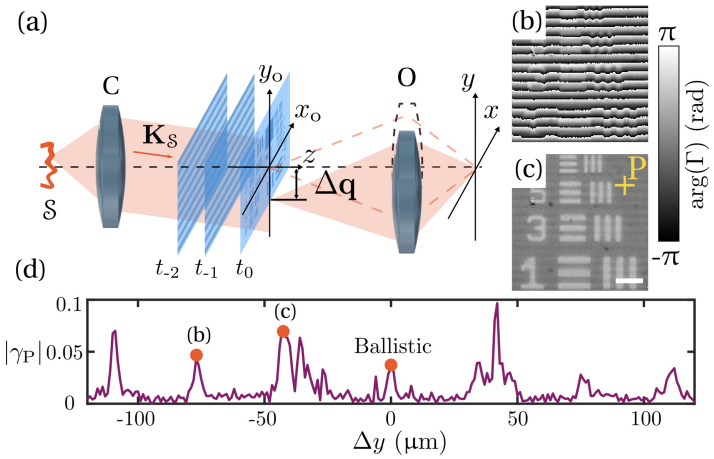

Figure 7.1: (a) Object setup illustration for MCF measurement of multiply scattered light by two diffraction gratings and phase resolution target. (b), (c) Phase images derived from MCF for $\Delta y^{(1)} = -77\,\mu\text{m}$ and $\Delta y^{(2)} = -42\,\mu\text{m}$. (d) Normalized modulus of measured MCF against Δy at point P. Objectives used 10x/NA = 0.3, $\text{NA}_\text{C} = 0.3$. Scale bar in (c) is 20 µm.

ply scattered light. MCF measured at $\Delta y^{(1)} = -77\,\mu\text{m} = -Y^+ z_{-2}/\tilde{K}$ carries information about the light diffracted into 1^{st} order of the first grating and 0^{th} order of the second grating. We therefore obtain $\Gamma[\mathbf{q};(0,\Delta y^{(1)})] \approx t_\text{f}(\mathbf{q})T'_{-2}(\mathbf{Q}^+)T'_{-1}(\mathbf{Q}^\text{o})\exp(2\pi\text{i}\mathbf{q}\cdot\mathbf{Q}^+)$. The phase image $\arg\{\Gamma[\mathbf{q};(0,\Delta y^{(1)})]\}$ is shown in Fig. 7.1(b). As predicted by Eq. (7.1), the phase is linearly modulated in the y-direction. The other illustrative case is for $\Delta y^{(2)} = -42\,\mu\text{m} = -Y^+ z_{-2}/\tilde{K} - Y^- z_{-1}/\tilde{K}$. Here we obtain from the measurement the complex image $\Gamma[\mathbf{q};(0,\Delta y^{(2)})] \approx t_\text{f}(\mathbf{q})T'_{-2}(\mathbf{Q}^+)T'_{-1}(\mathbf{Q}^-)$. Phase for this case is shown in Fig. 7.1(c). As could be predicted, no phase ramp appears for $\Delta y^{(2)}$ position, because modulation by $\mathbf{Q}^+$ and $\mathbf{Q}^-$ cancels up. Both of these cases are images formed purely by multiply scattered light. The phase ramp in Fig. 7.1(b) is straight forward to compensate for, therefore this experiment supports our statement that under certain circumstances, the coherence-gated multiply scattered light may play the same role in the imaging process as the ballistic light.

Despite neglecting the diffraction by the objective pupil in Eq. (5.11) in order to better understand coherence-gating effect, the resolving power of the real system is still diffraction limited. The ballistic image of the in-focus layer contains only spatial frequencies $T_\text{f}(\mathbf{Q}_\text{t})$ limited by the pupil function $P_\text{O}(\mathbf{K}_\text{t})$ centered at $\mathbf{Q}_\text{t} = (0,0)$. We showed that filtering by CGF a single diffraction order when imaging through diffraction grating causes the phase ramp modulation, which is interconnected with the spatial frequency spectrum shift with respect to the objective pupil. Knowledge of the shift can be used to synthetically extend the objective aperture and to directionally improve

resolution similarly to the structured illumination method [111]. The modulation process by the defocused layer is coherent, therefore the resolution improvement applies even for coherent imaging modalities such as quantitative phase imaging. We have used the object setup shown in Fig. 7.1(a) to acquire 5 images from the complete MCF measurement. The shifts of the object spatial frequency spectrum caused by the diffraction gratings in these images are $2\mathbf{Q}^+$, $\mathbf{Q}^+$, $\mathbf{Q}^o$, $\mathbf{Q}^-$ and $2\mathbf{Q}^-$. As a reference for the diffraction limited image we take the ballistic one with $\mathbf{Q}^o$ shift, the phase image is shown in Fig. 7.2(a). Combination of all 5 images using structured illumination approach [111]

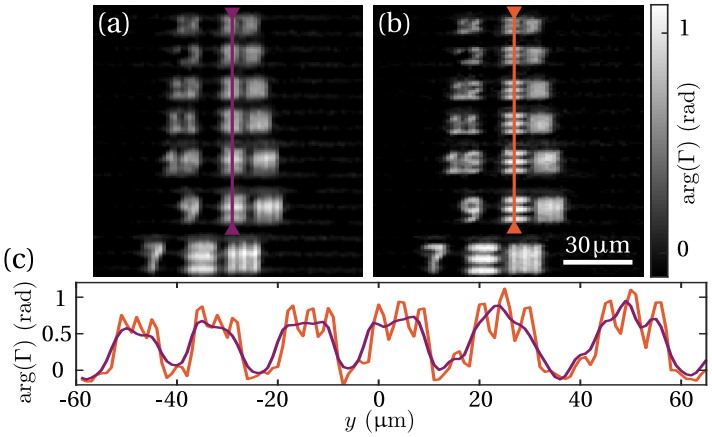

Figure 7.2: Directional resolution improvement when imaging through diffraction gratings. (a) Ballistic phase image, (b) synthetic phase image obtained by the structured illumination approach using multiply scattered coherence-gated light. (c) Cross-section along the purple and orange line in (a) and (b). Objectives used $4\text{x}/\text{NA} = 0.1, \text{NA}_\text{C} = 0.1$.

yields a synthetic phase image with the extended spatial frequency spectrum shown in Fig. 7.2(b). One can observe dramatic directional resolution improvement in the synthetic image, which is for clarity demonstrated by the cross-section comparison in Fig. 7.2(c).

7.2 Coherence-encoded synthetic aperture for super-resolution quantitative phase imaging

7.2.1 Motivation

The primary objective of biological research and medical diagnosis applications such as drug discovery [112], cancer cell biology [17, 18], and stem cell research [113] is to identify rare events of interest. Achieving a statistically and biologically meaningful analysis requires high-throughput imaging. However, the imaging platform's throughput is fundamentally limited by the space-bandwidth product of the optical system [114]. Due to this limitation, microscope designs face a trade-off between image resolution and field of view (FOV). Overcoming this limitation typically involves using high-resolution objectives combined with precise mechanical scanning of the sample followed by image stitching. However, the use of this approach in medical practice is limited due to the

mechanical scanning requirement and the short working distance of high-resolution objectives. To address these challenges, practical approaches have emerged that focus on surpassing the diffraction limit of low numerical aperture (NA) objectives while maintaining a large FOV and long working distance. Various techniques based on the synthetic aperture approach have been developed to achieve this [90–97, 103, 104]. By employing the synthetic aperture principles in digital holographic microscopy, specifically quantitative phase imaging (QPI), the limitations (invasive and non-quantitative) of traditional fluorescence microscopy can be overcome.

In this chapter of the thesis, we present a technique for improving the resolution of quantitative phase imaging beyond the diffraction limit. Our approach combines partially coherent holographic imaging with synthetic aperture microscopy. As mentioned in this chapter's introduction, CCHM utilizes a spatially broad thermal source within the Köhler illumination configuration instead of a conventional coherent point source for illumination. Therefore, the specimen is illuminated not by a single coherent wave, but by numerous mutually incoherent plane waves simultaneously. The implication is that the spatial frequency bandpass of the CCHM imaging system is twice as wide when using a broad illumination source compared to a point source [7]. As a result, the resolution that can be achieved conforms to Abbe's diffraction limit. Moreover, the standard CCHM image already reaches the maximum band limit attainable by certain methods discussed earlier [93, 94, 96], albeit only in their most extreme scenarios. Our goal is a further improvement of the resolution beyond Abbe's limit.

This thesis proposes applying the synthetic aperture approach to CCHM. This combination will provide the advantageous properties of both structured illumination and incoherent holographic imaging. Using incoherent illumination ensures high-quality single images and reduces the number of images required for reconstructing a high-NA image. Employing single-shot holography eliminates the need for iterative phase retrieval algorithms as in FPM, simplifying the aperture synthesis procedure. More importantly, this method allows for high-resolution imaging while maintaining a long working distance, which is crucial when imaging in standard multi-well plates and multi-channel chambers.

7.2.2 Outcomes

We demonstrate an unconventional use of the coherence-gating effect to allow the synthetic aperture imaging in a holographic microscope with partially coherent illumination. To the best of our knowledge, we utilize the coherence gate for the first time for a purpose different than imaging through or in turbid media. Thanks to the partially coherent illumination, our approach allows high-quality high-throughput synthetic aperture quantitative phase imaging, which is hardly matched by standard coherent synthetic aperture/structured illumination methods. We show synthesis of quantitative phase images with significantly increased spatial frequency bandwidth on real complex specimens such as cancer and cheek cells. We present here a thorough theoretical treatment of the coherence-gated imaging process as well as a detailed experimental methodology. We see the future potential of the method for high-throughput

studies (large field of view and high resolution).

7.2.3 Article 2

The article **Coherence-encoded synthetic aperture for super-resolution quantitative phase imaging** was published in **APL Photonics** (2022 Impact factor: 5.6, Q1 in Optics) in March 2022.

APL Photonics ARTICLE scitation.org/journal/app

Coherence-encoded synthetic aperture for super-resolution quantitative phase imaging

Cite as: APL Photon. 7, 046105 (2022); doi: 10.1063/5.0081134
Submitted: 7 December 2021 • Accepted: 20 March 2022 •
Published Online: 13 April 2022

Miroslav Ďuriš,[1,a)] Petr Bouchal,[1,2] Katarína Rovenská,[1] and Radim Chmelík[1,2]

AFFILIATIONS

[1] CEITEC—Central European Institute of Technology, Brno University of Technology, Purkyňova 656/123, 61200 Brno, Czech Republic

[2] Faculty of Mechanical Engineering, Institute of Physical Engineering, Brno University of Technology, Technická 2896/2, 61669 Brno, Czech Republic

[a)] **Author to whom correspondence should be addressed:** miroslav.duris@ceitec.vutbr.cz

ABSTRACT

Quantitative phase imaging (QPI) has quickly established its role in identifying rare events and screening in biomedicine or automated image data analysis using artificial intelligence. These and many other applications share the requirement for extensive high-quality datasets, which is challenging to meet because the invariance of the space–bandwidth product (SBP) fundamentally limits the microscope system throughput. Here, we present a method to overcome the SBP limit by achieving QPI super-resolution using a synthetic aperture approach in a holographic microscope with a partially coherent broad source illumination. We exploit intrinsic coherence-gating properties of the partially coherent light combined with the oblique illumination provided by the diffraction on a simple phase grating placed in proximity of the specimen. We sequentially coherence gate the light scattered into each grating's diffraction order, and we use the acquired images to synthesize QPI with significantly increased spatial frequency bandwidth. The resolution of QPI is increased substantially beyond Abbe's diffraction limit while a large field of view of low numerical aperture objectives is kept. This paper presents a thorough theoretical treatment of the coherence-gated imaging process supplemented by a detailed measurement methodology. The capability of the proposed method is demonstrated by imaging a phase resolution target and biological specimens. We envision our work providing an easily implementable super-resolution QPI method particularly suitable for high-throughput biomedical applications.

I. INTRODUCTION

Over recent years, quantitative phase imaging (QPI) has emerged and established itself as an irreplaceable imaging method in biomedical research. QPI provides label-free, non-invasive, real-time, and high-contrast quantitative means to image transparent specimens. Identifying rare events, for example, in drug discovery,[1] cancer cell biology,[2,3] or stem cell research,[4] requires the acquisition of not only quantitative data provided by QPI but also a statistically meaningful amount of high-resolution datasets. The recent development of automated data analysis and classification by artificial intelligence[5,6] exaggerates this ever-increasing demand for high-throughput QPI methods. Unfortunately, the throughput of a microscope is fundamentally limited by the invariance of the optical system space–bandwidth product[7] (SBP). Due to this limit, microscope designs always compromise between the achievable spatial resolution and effective field of view (FOV). Sequential acquisition of images while mechanically moving the specimen or microscope objective combined with image-stitching procedures increases SBP. However, enlarging the FOV while preserving the system's resolving power by mechanical movement of the specimen is suboptimal in live biological experiments. Moreover, manipulation with high numerical aperture (NA) objectives requires very precise autofocusing as they have very short working distances and short depths of focus.

To avoid mechanical movement, researchers increase SBP by overcoming the diffraction limit of low-NA objectives, motivated by their favorable properties—large FOV, long working distance and depth of focus, and price. Many QPI methods achieve sub-diffraction limited resolution by a sequential oblique coherent beam illumination and holographic detection.[8–11] These methods acquire images with downshifted high-frequency components of the

object spectrum and digitally synthesize a larger system aperture. A similar principle also applies to structured illumination microscopy in coherent modalities such as QPI, which illuminates the specimen simultaneously by several oblique beams.[12,13] The resolution increase was demonstrated even using a random speckle field illumination.[14,15] The illumination has to be manipulated to achieve the sub-diffraction limited resolution. Inverting light propagation through scattering media using a prerecorded transmission matrix has been shown to produce synthetic aperture QPI.[16] Lens-free techniques[17–19] provide unique imaging properties by avoiding the resolution-limiting diffraction on lens apertures. However, the specimen placement very close to the sensor significantly limits the applicability of the lens-free on-chip techniques.[17] The other group of lens-free techniques, digital in-line holographic microscopy,[18,19] has been already extended by synthetic aperture approaches[20,21] to significantly increase their resolving power. Due to its simple experimental implementation, a recently emerged Fourier ptychographic microscopy[22,23] (FPM) is a promising method achieving high SBP. FPM does not employ holographic detection, but it acquires only a series of intensity images for different oblique illuminations. High SBP QPI is in FPM obtained through the stitching of recorded images in Fourier space using an iterative phase retrieval algorithm,[24] representing the main drawback of this method. In general, all synthetic aperture methods increase the achievable spatial frequency bandwidth of the image by sacrificing other system's degrees of freedom.[25] For example, instead of sacrificing acquisition time, the dynamic range of a camera can be utilized to multiplex several off-axis holograms corresponding to different oblique illumination directions[26–28] into a single measurement. This elegant approach provides a single-shot synthetic aperture method; however, it may decrease the quantitative phase image quality.[29]

In this paper, we introduce a method for QPI resolution enhancement below the diffraction limit that combines partially coherent (PC) holographic imaging with synthetic aperture microscopy. Instead of a standard coherent point source illumination [see Fig. 1(a)], we utilize a spatially broad thermal source in the Köhler illumination [see Fig. 1(b)] arrangement. Therefore, the specimen is not illuminated by one but by many mutually incoherent plane waves simultaneously. The aperture of the illumination cone is proportional to the condenser lens numerical aperture (NA_C). Compared to the point source illumination, the broad source gives the imaging system the spatial frequency bandpass with a twice as large radius.[30] Consequently, the achievable resolution meets Abbe's diffraction limit, and our standard image already has the band limit reachable by some methods mentioned above[11,12,14] only in their upper-limit cases. Our goal is further improvement of the resolution beyond Abbe's limit.

We utilize a simple phase grating (PG), composed of hexagonal elements, to simultaneously tilt the whole illumination cone into several oblique directions. This is achieved by placing PG on the illumination side of the specimen; see Figs. 1(c) and 1(d). The oblique illumination shifts the object's spectrum, as illustrated in Figs. 1(b)–1(d), which makes images corresponding to each diffraction order contain different information. However, the simultaneous presence of images from all diffraction orders and their superposition in intensity make their information content inaccessible by standard methods. We exploit the coherence-gating properties of PC illumination[31] to capture images formed only by the light scattered into separate grating's diffraction orders. The coherence-gated images contain separate shifted image spectra, which we digitally combine to create a synthetic aperture image with subdiffraction-limited resolution. To the best of our knowledge, we are the first to utilize the coherence gate for a purpose different than imaging through or in turbid media. Due to the broad spectral support of a single measurement, using only the ±first diffraction orders of the PG is sufficient to achieve a similar resolution as FPM with a significantly lower number of acquisitions. Coherence-gating interconnected with PC illumination also reduces coherent phase artifacts to a minimum, resulting in high phase quality of a single image not matched by iterative phase retrieval algorithms.

II. OPTICAL SETUP DESCRIPTION

To demonstrate proposed principles, we used a coherence-controlled holographic microscope[30] (CCHM), commercially available as Telight Q-Phase. Another implementation of the synthetic aperture method to commercially available microscopes has been previously reported in Ref. 32. The optical setup (see Fig. 2) is an adaptation of the Mach–Zehnder interferometer. It consists of the object and reference arm, which contain optically equivalent microscope systems. The functionality of this microscope depends on

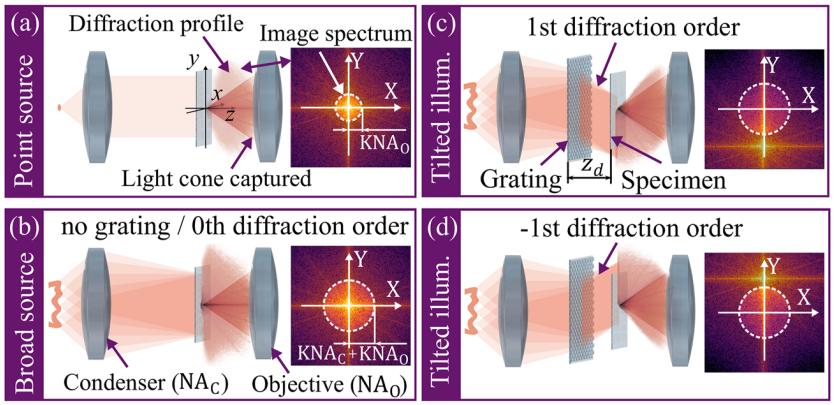

FIG. 1. Illumination and detection schemes with (a) point source and (b)–(d) broad source in the Köhler illumination arrangement. Each scheme depicts the transmitted object's spatial information by the imaging system in spatial frequency coordinates *X*, *Y* (note larger frequency bandpass when using Köhler illumination). The band limit values are explained in the text. (c) and (d) Diffraction grating introducing a spectrum shift in the regime of Köhler illumination (images illustrate only one of the diffraction orders).

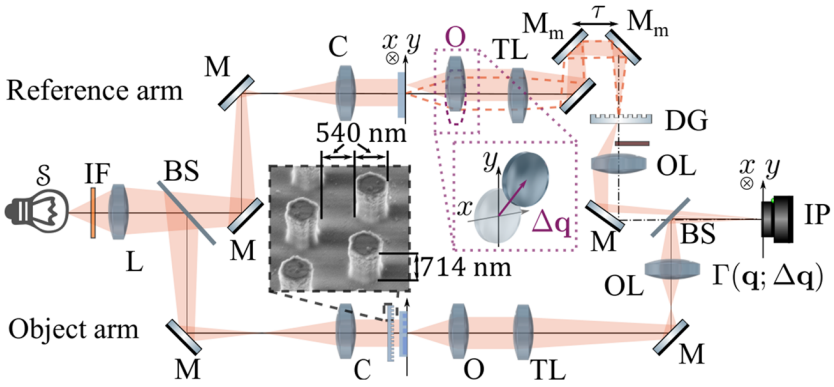

FIG. 2. Optical setup of the coherence-controlled holographic microscope: S: light source; IF: interference filter; L: relay lens; BS: beam splitters; M: mirrors; Mm: movable mirrors; C: condensers; O: objective lenses; TL: tube lenses; DG: diffraction grating; OL: output lenses; IP: interference plane; and PG: phase grating (the inset shows the image of the PG obtained by a scanning electron microscope).

the diffraction grating (DG, transmission phase grating with groove frequency 150 mm^{-1}, blazed at 760 nm for the first diffraction order) implemented in the reference arm according to principles proposed by Leith and Upatnieks[33] (for the details about the DG choice, see Ref. 30). It guarantees off-axis hologram formation in the interference plane (IP) for sources of an arbitrary degree of coherence. The role the coherence plays in the CCHM imaging process has been described in detail.[34] In our system, a halogen lamp is used for illumination to provide thermal, spatially broad source, and we filter the illuminating light by an interference filter (IF) with central wavelength 650 and 10 nm full width at half maximum to achieve also quasi-monochromatic illumination. The most important properties of the source for the method discussed in this work are low spatial coherence and the size of the source. Therefore, an LED or coherent (laser) source with a rotating diffuser could also be used instead of a halogen lamp and IF. The source is imaged by a pair of achromatic doublets (simplified as L in Fig. 2, focal lengths 63.5 and 350 mm) through a beam splitter (BS) to the front focal planes of the condensers (C, Nikon LWD condenser lens NA 0.52 with adjustable aperture stop), forming Köhler illumination. The fundamental image properties depend on the parameters of condensers and objective lenses (O, Nikon Plan Fluorite Objectives, 10×/0.3 NA/16 mm WD and 20×/0.5 NA/2.1 mm WD) in couples with tube lenses (TL, Nikon focal length 200 mm) characterized by the pupil functions (see Ref. 34) P_C and P_O, respectively. The output lenses (OL) are objectives with focal lengths 35 mm and f/2. If we assume circular lens apertures, then pupil functions are limited by the numerical apertures of condensers NA_C and objectives NA_O. These two parameters define the spatial frequency band limit $|\mathbf{K}_{max}|$ of our optical setup [see Fig. 1(b)] as $|\mathbf{K}_{max}| = K(NA_C + NA_O)$, where $K = 1/\lambda$ with λ being the wavelength of light and $NA_C \leq NA_O$. Stepper and piezo motors provide fine adjustment of the microscope optical components. The holograms are recorded in IP using the MR4021MC-BH XIMEA CCD camera.

To achieve subdiffraction-limited resolution in the above-described configuration, we placed the PG in experiments according to Figs. 1(c) and 1(d), and Fig. 2 on the illumination side of the specimen. The distance z_d between the specimen and PG was defined by a cover slip placed between them. We have designed the PG to diffract light into six directions with the scattering vector size of 926 mm^{-1}. The first step of production was the creation of chromium hexagonal structures on the fused silica substrate (thickness 700 μm) using electron-beam lithography. These served as a mask for reactive ion etching of the underlying substrate. We designed the etching depth to produce elements causing phase retardation of π for the 650 nm wavelength. After removing the residual chromium mask, we measured the height of the hexagonal fused silica pillars using a scanning electron microscope to be 714 nm, the side-to-side pillar dimensions and pillar separation are both ~540 nm; see the inset of Fig. 2. The PG predominantly scatters light into zeroth and ±first diffraction orders of each direction. It can be calculated[35] that the diffraction efficiency of the second diffraction orders is for our PG design four times lower than the efficiency of the first diffraction order. As we will further show, the light scattered into higher diffraction orders is effectively eliminated from the image formation process by the coherence gating and only contributes to the background intensity taking a small amount of the camera dynamic range. Therefore, we further assume that the spatial frequency spectrum of the PG is discrete and has significant values only for seven spatial frequencies corresponding to each dominant diffraction order. The same phase grating was used in all experiments presented in this paper.

III. THEORY

To separate light scattered into a single diffraction order, i.e., one illumination direction, we utilize intrinsic coherence-gating effects of the PC illumination in CCHM.[31] Therefore, we start by describing the coherence-gating properties of the PC light by the mutual coherence function (MCF). MCF is a quantity measured in partially coherent interferometers, and we obtain it from holograms, time-averaged intensity measurements in IP. They contain the cross correlation information between object-scattered and reference light, which we retrieve by a carrier removal in the Fourier plane.[30] For the PC light, the cross correlation term depends on the transversal displacement $\Delta\mathbf{q} = (\Delta x, \Delta y)$ and relative time-delay τ of the object-scattered and reference field and can be understood as their mutual coherence function[31] $\Gamma(\mathbf{q}, \mathbf{q} - \Delta\mathbf{q}, \tau)$. Here, $\mathbf{q} = (x, y)$ is the position of a point in the image plane specified by the coordinates of the optically conjugated point in the object plane. We call the interferometric imaging for a given time-delay τ and transverse displacement $\Delta\mathbf{q}$ a partial MCF measurement. Modulus and phase image for particular $\Delta\mathbf{q}$ and τ are obtained as modulus and argument

of Γ, respectively. The complete MCF is acquired by measuring and reconstructing holograms for all accessible $\Delta\mathbf{q}$ and τ. Every partially coherent interferometric system is, in principle, capable of measuring complete MCF if the reference field position and optical path difference can be manipulated. In CCHM, we control these parameters by the reference arm elongation and objective shift (see Fig. 2). As we use in experiments quasi-monochromatic illumination (central wavelength 650 nm and 10 nm full width at half maximum), the influence of temporal coherence (the coherence length[36] of ~42 μm) is minimal and manifests mainly as a speckle noise reduction. Before each experiment, we set τ to zero, which corresponds to the highest contrast of interference fringes. Our further analysis will stay within the limits of paraxial approximation. We will, therefore, discuss mainly effects interconnected with spatial coherence. Given a complete spatial incoherence of the source, the expression for the measured MCF for $\tau = 0$ has, according to Eq. (4.4–31) in Ref. 36, the form

$$\Gamma(\mathbf{q}, \mathbf{q} - \Delta\mathbf{q}) = \iint_{-\infty}^{\infty} |P_C(\mathbf{K}_S)|^2 \times h_o(\mathbf{q}, \mathbf{K}_S) h_r^*(\mathbf{q} - \Delta\mathbf{q}, \mathbf{K}_S) \mathrm{d}^2\mathbf{K}_S, \quad (1)$$

where $h_o(\mathbf{q}, \mathbf{K}_t)$ and $h_r(\mathbf{q}, \mathbf{K}_t)$ describe the propagation of a plane wave with transverse wave vector $\mathbf{K}_t$ behind the condenser lenses through the object and reference arm, respectively. The transverse wave vector coordinates $\mathbf{K}_S$ of a plane wave behind condensers are assumed to be proportional to the respective source point coordinates in the front focal planes of the condensers. For this reason, the source properties can be characterized by a function of $\mathbf{K}_S$. We use reduced wave vector notation $|\mathbf{K}| = K = 1/\lambda$, which is assumed to be a constant here and $\mathbf{K} = (\mathbf{K}_t, K_z) = (K_x, K_y, K_z)$, where $\mathbf{K}_t$ is the transverse wave vector and $K_z = \sqrt{|\mathbf{K}|^2 - |\mathbf{K}_t|^2}$.

We derive $h_o(\mathbf{q}, \mathbf{K}_t)$ such that the specimen $t_o(\mathbf{q})$ is placed in the objective lens front focal plane, and the PG is at a distance z_d from the specimen; see Fig. 1(c). We assume single scattering of the plane wave formed by the condenser lens by the grating and the imaged specimen and no back-scattering, i.e., the light undertakes two successive scattering events. Using similar approach as in Ref. 31, the propagation of the plane wave through the object arm can be described by

$$h_o(\mathbf{q}, \mathbf{K}_t) = \mathrm{e}^{2\pi\mathrm{i}\mathbf{q}\cdot\mathbf{K}_t} \iint \iint P_O(\mathbf{K}_t + \mathbf{Q}_d + \mathbf{Q}_o) \times T_d'(\mathbf{Q}_d) T_o(\mathbf{Q}_o) \mathrm{e}^{2\pi\mathrm{i}\mathbf{Q}_d\cdot(\mathbf{K}_t z_d/K + \mathbf{q})} \times \mathrm{e}^{2\pi\mathrm{i}\mathbf{Q}_o\cdot\mathbf{q}} \mathrm{d}^2\mathbf{Q}_d \mathrm{d}^2\mathbf{Q}_o, \quad (2)$$

where $T_d'(\mathbf{Q}) = T_d(\mathbf{Q}) \exp(\pi\mathrm{i} z_d |\mathbf{Q}|^2/K)$ is a discrete spatial frequency spectrum of the defocused grating, $T_o(\mathbf{Q}_o)$ is a spatial frequency spectrum of the specimen, and $\mathbf{Q} = (X, Y)$ is a scattering vector. The propagation of a plane wave in the reference arm is described by $h_r(\mathbf{q}, \mathbf{K}_t) = P_O(\mathbf{K}_t) \exp(2\pi\mathrm{i}\mathbf{K}_t \cdot \mathbf{q})$. Next, we substitute this expression and Eq. (2) into Eq. (1), and to reflect the discrete and sparse nature of the PG spatial frequency spectrum, we replace the integration over $\mathbf{Q}_d$ with a summation over $\mathbf{Q}_j$, where $j = 0, 1, \ldots, 6$ corresponds to the grating diffraction orders. After simple manipulations, we obtain the expression

$$\Gamma(\mathbf{q}; \Delta\mathbf{q}) = \sum_{\mathbf{Q}_j} [t_o(\mathbf{q}) \mathrm{e}^{2\pi\mathrm{i}\mathbf{Q}_j\cdot\mathbf{q}}] \otimes h(\mathbf{q}; \Delta\mathbf{q}, \mathbf{Q}_j) T_d'(\mathbf{Q}_j), \quad (3)$$

where ⊗ denotes convolution and $h(\mathbf{q}; \Delta\mathbf{q}, \mathbf{Q}_j) = \mathcal{G}^*(\mathbf{q} - \Delta\mathbf{q} - \mathbf{Q}_j z_d/K) p_o(\mathbf{q})$, where functions $\mathcal{G}(\mathbf{q}) = \iint |P_C(\mathbf{K}_t)|^2 P_O(\mathbf{K}_t) \exp(2\pi\mathrm{i}\mathbf{K}_t \cdot \mathbf{q}) \mathrm{d}^2\mathbf{K}_t$ and $p_o(\mathbf{q}) = \iint P_O(\mathbf{K}_t) \exp(2\pi\mathrm{i}\mathbf{K}_t \cdot \mathbf{q}) \mathrm{d}^2\mathbf{K}_t$ can be approximated using the Bessel function of the first kind as $\mathcal{G}(\mathbf{q}) = 2J_1(\mu)/\mu$ and $p_o(\mathbf{q}) = 2J_1(\nu)/\nu$, where $\mu = 2\pi K \mathrm{NA}_C |\mathbf{q}|$ and $\nu = 2\pi K \mathrm{NA}_O |\mathbf{q}|$.

We call the function $\mathcal{G}$ a coherence-gating function[31] (CGF) because it significantly reduces the effects of the defocused objects on the image of the focused specimen. Gating properties of the CGF are interconnected with the spatial degree of coherence. The CGF principal maximum width increases (decreases) with increasing (decreasing) spatial coherence. CGF shape and position $\Delta\mathbf{q}$ affects the function $h(\mathbf{q}; \Delta\mathbf{q}, \mathbf{Q}_j)$, which dictates the degree of contribution of particular spatial frequencies $\mathbf{Q}_j$ of the grating. The function $h(\mathbf{q}; \Delta\mathbf{q}, \mathbf{Q}_j)$ has non-negligible values only for $\mathbf{Q}_j$, which are in relation to the CGF position $\Delta\mathbf{q}$ such that $\mathbf{Q}_j \approx -\Delta\mathbf{q}K/z_d$. Otherwise, $h(\mathbf{q}; \Delta\mathbf{q}, \mathbf{Q}_d)$ is effectively zero. Due to the sparsely distributed PG spatial frequency spectrum, a specific choice of CGF position allows us to eliminate the effects of all but one PG spatial frequency. This filtration would not be possible if a spatially coherent source was used. In that case, the grating would be projected to the specimen plane.

Sequential acquisition of seven holograms for CGF positions $\Delta\mathbf{q}_j = -\mathbf{Q}_j z_d/K$ corresponding to PG spatial frequencies gives us parts of MCF in the form $\Gamma_j = \Gamma(\mathbf{q}; \Delta\mathbf{q}_j) = [t_o(\mathbf{q}) \exp(2\pi\mathrm{i}\mathbf{Q}_j \cdot \mathbf{q})] \otimes h(\mathbf{q}) T_d'(\mathbf{Q}_j)$. Each of these MCF parts is an image of $t_o(\mathbf{q})$. The phase ramp $\exp(2\pi\mathrm{i}\mathbf{Q}_j \cdot \mathbf{q})$ causes a shift of the object's spectrum $T_o(\mathbf{Q} - \mathbf{Q}_j)$. The term $T_d'(\mathbf{Q}_j)$ represents a simple phase offset and scaling by diffraction efficiency of the grating. The convolution by $h(\mathbf{q}) = \mathcal{G}^*(\mathbf{q}) p_o(\mathbf{q})$ is in the Fourier space a linear filtration of $T_o(\mathbf{Q} - \mathbf{Q}_j)$ by the coherent transfer function (CTF) centered at $\mathbf{Q} = (0, 0)$. CTF is defined as a Fourier transform of $h(\mathbf{q})$, and its support radius equals $K(\mathrm{NA}_C + \mathrm{NA}_O)$. The CTF is similar to the one of the standard optical transfer function of the incoherent system[34] and can be calculated as a cross correlation of $P_O(\mathbf{K}_t)$ and $|P_C(\mathbf{K}_t)|^2 P_O(\mathbf{K}_t)$. For simplicity, we can approximate the pupil functions with a step-like profile such that $P_O(\mathbf{K}_t) = 1$ for $|\mathbf{K}_t| \le K\mathrm{NA}_O$ and $P_C(\mathbf{K}_t) = 1$ for $|\mathbf{K}_t| \le K\mathrm{NA}_C$, and otherwise, these functions are zero. The cross correlation then yields a conical shape of the CTF, suggesting that the contrast of the image spatial frequency content is decreasing for higher spatial frequencies.

We illustrate the outlined theoretical principles using simulated data with the resolution target as the specimen and phase grating composed of hexagonal elements. In Fig. 3(a), there is the spatial frequency spectrum of the resolution target, and in Fig. 3(b), there is the spectrum of the grating. Dashed circles in Fig. 3(a) have the size corresponding to the CTF support, and they illustrate which part of the object spectrum is sampled by Γ_j. The image represented by Γ_0 is the standard diffraction-limited image of $t_o(\mathbf{q})$, and as illustrated by Fig. 3(a), images Γ_{1-6} contain subdiffraction information.

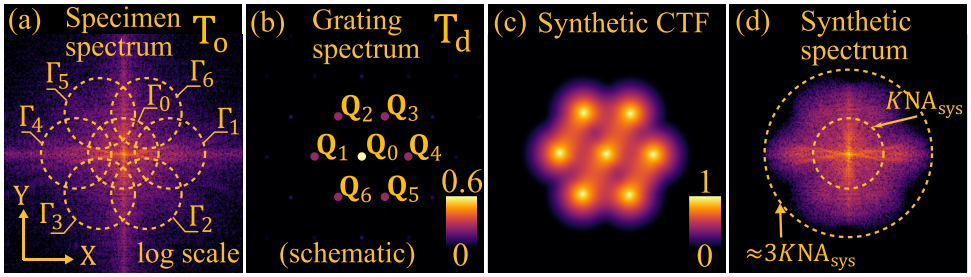

FIG. 3. Principle of the proposed synthetic aperture method. (a) The spectrum of the specimen, (b) spectrum of the grating, (c) synthetic CTF, and (d) synthetic spectrum of the specimen image, where $NA_{sys} = NA_O + NA_C$.

Spatial frequency information contained in each Γ_j is after acquisition centered at $\mathbf{Q} = (0,0)$; see Figs. 1(b) and 1(c). As shown in Fig. 3(a), the correct positions are the grating's spatial frequencies $\mathbf{Q}_j$. Therefore, the spectra of Γ_j must be appropriately translated to create a synthetic image with extended spatial frequency content. Digital removal of the phase ramp $\exp(2\pi i\mathbf{Q}_j \cdot \mathbf{q})$ achieves the correct translation of the Γ_j spectrum. To obtain an improved resolution after superposition $\sum \Gamma_j$, the phase offset and scaling caused by $T_d'(\mathbf{Q}_j)$ have to be removed.

The phase ramp, scaling, and phase offset can be in an ideal case removed if we divide Γ_j by the MCF measured for the same CGF positions with the grating present but the specimen absent. This means that $t_o(\mathbf{q}) = 1$ in Eq. (3). We denote measurement without specimen by $\Gamma_B(\mathbf{q};\Delta\mathbf{q}_j)$. Therefore, we can obtain an image $\Gamma_{SA}(\mathbf{q})$ that corresponds to imaging by a synthetic aperture system in the following way:

$$\Gamma_{SA}(\mathbf{q}) = \sum_j \frac{\Gamma(\mathbf{q};\Delta\mathbf{q}_j)}{\Gamma_B(\mathbf{q};\Delta\mathbf{q}_j)} = t_o(\mathbf{q}) \otimes h_{SA}(\mathbf{q}), \tag{4}$$

where $h_{SA}(\mathbf{q})$ is an inverse Fourier transform of the synthetic CTF of the system; see Fig. 3(c). In Fig. 3(d) is displayed the spatial frequency spectrum of the synthetic image. If we consider only the first diffraction orders of the PG corresponding to spatial frequencies $|\mathbf{Q}_j| = 2K(NA_C + NA_O)$, our method can theoretically provide up to a three-fold increase in the cut-off frequency of the imaging system. However, in experimental situations, noise from various sources limits the detection of low-contrast spatial frequencies, and setting $|\mathbf{Q}_j| = 2K(NA_C + NA_O)$ would result in loss of information from some parts of the image spatial frequency spectrum. Therefore, the $|\mathbf{Q}_j|$ values of the PG should be designed with respect to image noise levels and to allow for creation of reasonably uniform synthetic CTF [see Fig. 3(c)]. It is important to note that the contrast of spatial frequency information at points of CTF with lower amplitude can be enhanced by deconvolution.[37] We chose in this work to avoid any excessive digital post-processing (including deconvolution) unnecessary for aperture synthesis to better demonstrate the performance improvement provided by the proposed method.

IV. METHODOLOGY

The measurement and image reconstruction methodology differ for the cases when the grating's spatial frequencies $\mathbf{Q}_j$ are within and outside the bandpass of the microscope. The PG described in Sec. II allows us to demonstrate both cases. We have designed the PG to increase performance of a setup using $10\times/NA_O = 0.30$ objectives and condensers with $NA_C = 0.30$ such that the synthetic aperture approach should produce a synthetic CTF delivering an effective spatial resolution corresponding to a setup with $20\times/NA_O = 0.50$ objectives and $NA_C = 0.50$. Without loss of generality, we further demonstrate both cases using the same PG but different imaging objectives.

The measurement and reconstruction methodology outlined in Sec. III is straightforward to implement if the grating's spatial frequencies $\mathbf{Q}_j$ are within the bandpass of the microscope. This is satisfied if we use in our experimental system $20\times/NA_O = 0.50$ objectives and condensers with $NA_C = 0.30$, giving us the theoretical cut-off frequency $|\mathbf{K}_{max}| = 1230\ mm^{-1}$, and the PG with $|\mathbf{Q}_j| = 926\ mm^{-1}$. The data supporting methodology explanation shown in Fig. 4 is obtained from an experiment with a phase resolution target [phase image shown in Fig. 4(a)] illuminated through the hexagonal PG. In order to image by the light scattered in one of the diffraction orders other than zeroth, we have to find the exact reference objective positions $\Delta\mathbf{q}_j = -\mathbf{Q}_j z_d/K$. These positions change for each experiment as they depend on the PG orientation and the defocus z_d. We determine the positions $\Delta\mathbf{q}_j$ from the complete MCF measurement. As the $\Delta\mathbf{q}_j$ positions linearly scale with the defocus z_d, we show, for demonstration purposes, complete MCF measurement with smaller z_d than in an actual experiment. Each peak in the modulus of complete MCF [see Fig. 4(b)] for a point P [marked in Fig. 4(a)] corresponds to one of the PG diffraction orders. Positions with maximal modulus values of the peaks are the reference arm objective shifts $\Delta\mathbf{q}_j$ [see Fig. 4(b)]. We use these positions to image by the coherence-gated light corresponding to each diffraction order the blank FOV $[\Gamma_B(\mathbf{q};\Delta\mathbf{q}_j)]$ and the specimen $[\Gamma(\mathbf{q};\Delta\mathbf{q}_j)]$. The modulus value of the peaks is proportional to the distribution $|T_d(\mathbf{Q})|$ of the illumination amplitude between diffraction orders.

The phase and modulus images of a resolution target section, marked by the dashed line in Fig. 4(a), obtained for $\Delta\mathbf{q}_0$, i.e., zeroth diffraction order, are shown in Figs. 4(c) and 4(d), respectively. The spatial frequency spectrum corresponding to the full FOV image is shown in Fig. 4(e). We can see the effects of the oblique illumination by comparing the zeroth-order images in Figs. 4(c)–4(e) with the images in Figs. 4(f)–4(h) obtained for $\Delta\mathbf{q}_1$, i.e., diffraction

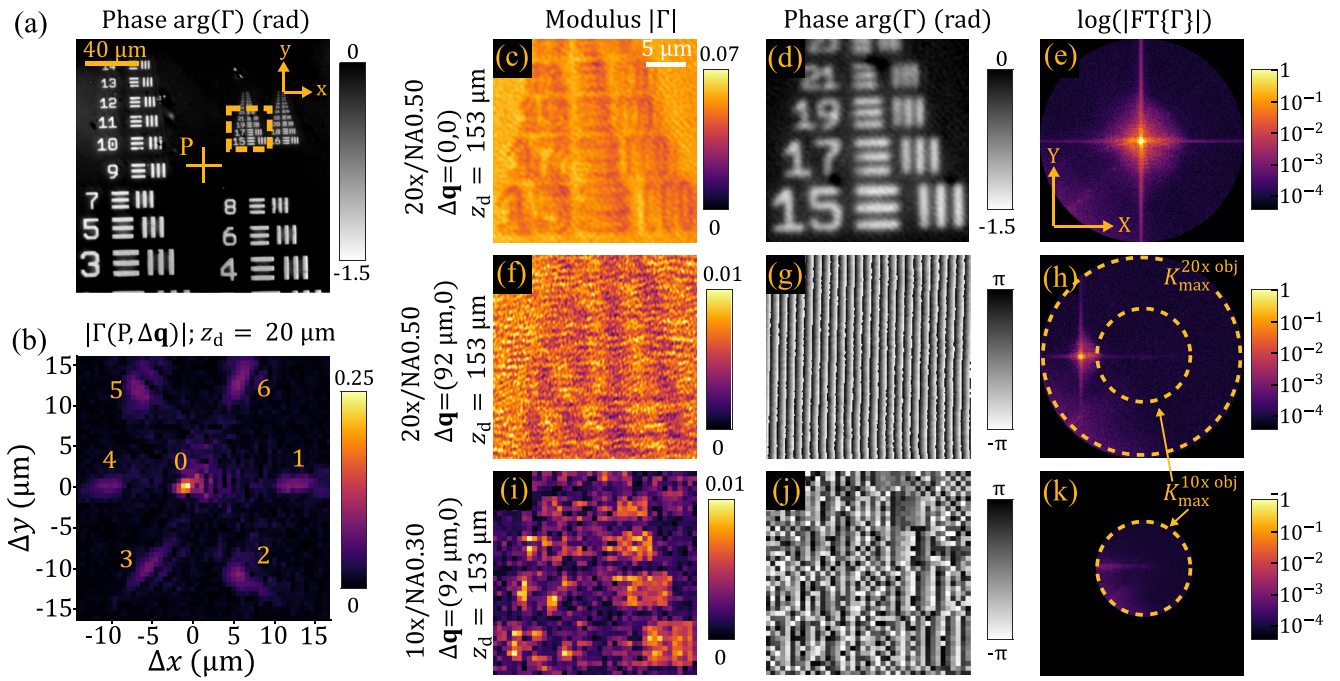

FIG. 4. Measurement of MCF with the phase resolution target in focus illuminated through the hexagonal grating. (a) Image of the phase resolution target obtained with 20×/NA_O = 0.50 objectives, NA_C = 0.30. The dashed line marks the section of the resolution target, which the images in (c) (d) (f) (g) (i)and (j) are based on. (b) Modulus of the complete MCF measured at point P with 20× objectives plotted as a function of $\Delta\mathbf{q}$ with defocus z_d = 20 µm. (c) Modulus and (d) phase image obtained with 20× objectives for $\Delta\mathbf{q} = (0, 0)$. (e) Modulus of the corresponding spatial frequency spectrum in the logarithmic scale. (f) Modulus, (g) phase, and (h) spectrum image obtained with 20× objectives for $\Delta\mathbf{q}$ = (92 µm, 0). (i) Modulus, (j) phase, and (k) spectrum image obtained with 10×/NA_O = 0.30 objectives and NA_C = 0.30 for $\Delta\mathbf{q}$ = (92 µm, 0).

order corresponding to the peak one in Fig. 4(b). When comparing Figs. 4(c) and 4(f), we see that the drop in the modulus value results in higher image noise. The phase image in Fig. 4(g) contains a phase ramp proportional to the spatial frequency spectrum shift shown in Fig. 4(h). Similar phase ramp and spectrum shift proportional to $\Delta\mathbf{q}_j$ experience also images corresponding to peaks 2–6. We can apply procedure described by Eq. (4) to obtain the synthetic aperture image. The need for blank FOV images $\Gamma_B(\mathbf{q};\Delta\mathbf{q}_j)$ limits the bandwidth widening up to a two-fold increase. In this limiting case, the PG would have to be designed with spatial frequencies $\mathbf{Q}_j$ matching the cut-off frequency of the system $|\mathbf{K}_{max}|$.

For a further (up to three-fold) bandwidth increase, we have to choose a different approach because the PG needs to have spatial frequencies outside the optical system band limit. The same PG as used in the previous experiment has the spatial frequencies $|\mathbf{Q}_j|$ outside the bandwidth of the system when using 10×/NA_O = 0.30 objectives and condensers with NA_C = 0.30. The system's cut-off frequency is $|\mathbf{K}_{max}| = 923\ mm^{-1}$ and $|\mathbf{Q}_j| = 926\ mm^{-1}$; therefore, the expected bandwidth increase is slightly more than two-fold. However, the methodology described further is applicable also to cases when the PG would be designed with spatial frequencies up to $|\mathbf{Q}_j| = 2|\mathbf{K}_{max}|$, which would provide the three-fold bandwidth enhancement. In this optical arrangement, the images formed by the light corresponding to one of the diffraction orders 1–6 are dark-field because the objectives do not transmit the oblique unscattered illuminating light; see the modulus [Fig. 4(i)] and phase [Fig. 4(j)] image and spatial frequency spectrum [Fig. 4(k)] for $\Delta\mathbf{q}_1$. Therefore, it is impossible to measure blank FOV images $\Gamma_B(\mathbf{q};\Delta\mathbf{q}_j)$ and subsequently apply Eq. (4). To acquire dark-field images captured for $\Delta\mathbf{q}_{1-6}$ and to achieve their correct spectrum shift and scaling, we use the information from the experiment with 20× objectives. The complete MCF measurement provides us $\Delta\mathbf{q}_j$ positions and modulus scaling values. The images obtained for $\Delta\mathbf{q}_j$ with 10× objectives contain the same phase ramp as the images obtained with 20× objectives. As mentioned before, the compensation of the phase ramp causes the correct spectrum shift. Therefore, we find the phase ramps that create flat phase images obtained with 20× objectives for $\Delta\mathbf{q}_j$ and use these phase ramps to shift the spectrum of dark-field images obtained with 10× objectives to their correct positions.

The final part of the image synthesis for both cases is phase matching. The phase offset in each image is generally random due to small fluctuations of the optical system parameters between individual hologram acquisitions. The phase matching is the process of adjusting the phase of Γ_j by multiplying it by $\exp[i(A_j + B_j x + C_j y)]$ where $A_j, B_j,$ and C_j are parameters different for each image. This way we remove the random phase offset and slightly move the image spectra to more correct positions. Previous works have shown that poor phase matching leads to creation of image

artifacts[38] and can even entirely prevent resolution improvement.[39] The phase can be matched by visual evaluation of the superposed image[8] or by programmatic maximization of image sharpness metrics.[39] We approach the phase matching of the seven complex-valued images as a minimization problem. During the optimization, the parameters A_j, B_j, and C_j are adjusted to find the minimal value of the negative image variation[40] of the synthetic aperture phase image $[\arg(\sum \Gamma_j)]$. To solve this minimization problem, we used MATLAB and its non-linear solver fmincon from Optimization Toolbox.

V. RESULTS AND DISCUSSION

We demonstrate the feasibility of the proposed method in the optical system utilizing $10\times/\mathrm{NA_O} = 0.30$ objectives and condensers with $\mathrm{NA_C} = 0.30$. As mentioned in Sec. IV, the PG design (540 nm features) allows us to create a synthetic aperture image with a two-fold increase in the spatial frequency bandwidth, i.e., a 50% resolution improvement. During the PG design, we aimed to balance out the achievable resolution improvement and the uniformity of the CTF in order to avoid image artifacts due to the missing lower spatial frequency content. This was performed with respect to camera readout noise levels and the dynamic range, and the resulting synthetic CTF shape is shown in Fig. 3(c).

We demonstrate the resolution improvement using the phase resolution target first. We measured and combined the images obtained for each diffraction order using the methodology explained in Sec. IV. As expected, the comparison of the diffraction-limited [Fig. 5(a)] and synthetic aperture [Fig. 5(b)] image shows the resolution improvement. The diffraction-limited image [Fig. 5(a)] is represented by the image obtained for $\Delta\mathbf{q}_0$. The smallest resolvable features in the diffraction-limited image marked by the number 20 are 0.65 μm wide. This means the resolution is 1.3 μm. In the synthetic image, the smallest resolvable features (number 23) are 0.47 μm wide. It is important to note that the contrast of the number

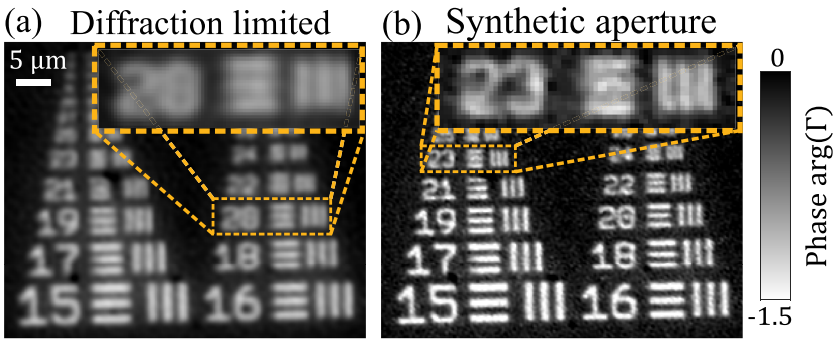

FIG. 5. Comparison of (a) the diffraction-limited and (b) synthetic aperture image of the phase resolution target.

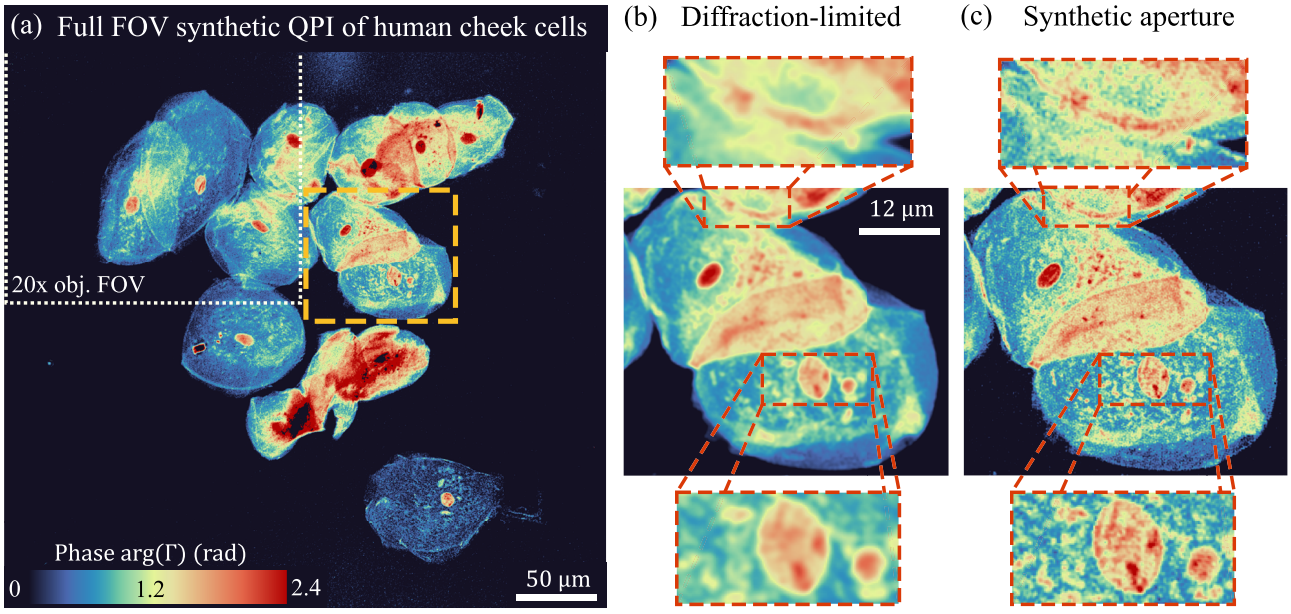

FIG. 6. Results of the proposed method from imaging of human cheek epithelial cells. (a) Full FOV synthetic aperture QPI. (b) A section [marked by the dashed line in (a)] of the diffraction-limited phase image. (c) A section of the synthetic aperture phase image. The insets in (b) and (c) show (upper) the magnified cell interface and (lower) magnified nucleus and other intracellular content.

23 features is better than the contrast of the smallest resolved features in the diffraction-limited image. Therefore, the spatial resolution is between 0.94 and 0.86 μm (unresolved number 24 has 0.43 μm wide elements), and the resolution improvement is from 28% to 34%. We attribute the slightly lower resolving power than expected to the optical aberrations and lowered hologram contrast due to the multiplexing of light from all illumination directions in intensity. The aberrations are caused by the thick PG substrate and by the reference arm off-axis optical arrangement introducing coma and shearing[41] to the reference beam.

We demonstrate the feasibility of our approach for biological experiments by imaging human cheek epithelial cells first. We squeezed the cells with a drop of water between two coverslips, then placed the PG on top of the upper cover slip, and applied the proposed method. Figure 6(a) shows the full FOV synthetic aperture QPI capturing several cells simultaneously with high resolution. White dashed lines in Figs. 6(a) and 7(a) mark the practical FOV of the 20× objectives, which provide spatial resolution similar to resolution achieved by our synthetic aperture approach with 10× objectives. As the resolution is comparable, the enlargement of the effective FOV is proportional to the SBP increase, which reaches values significantly beyond its limit (imposed by diffraction). We demonstrate the increased information content in the synthetic aperture image by comparing its section Fig. 6(c) to the diffraction-limited variant Fig. 6(b). The comparison shows that the synthetic aperture image allows for observation of previously unresolved fine features inside the nuclei and other intracellular content [see the lower insets of Figs. 6(b) and 6(c)]. Furthermore, the enhanced resolution increases the cell membrane sharpness [see the upper insets of Figs. 6(b) and 6(c)]. In high-throughput studies, well-resolved cell membranes, especially in the regions of cells in contact with each other, are crucial for automated cell segmentation.[42]

Next, we show the performance of our method for the creation of the synthetic aperture QPI of rat embryo fibroblasts in Fig. 7. We used LW13K2 cells from a cell line of spontaneously transformed rat embryo fibroblasts LW13 of inbred strain Lewis. Cells were cultivated at 37 °C in a humidified incubator with 3.5% CO_2 in standard minimum essential medium eagle with Hanks' salts supplemented with 10% fetal bovine serum and 20 μM gentamicin and 2 mM *L*-glutamine. The cells were subsequently fixed using 4% formaldehyde in phosphate-buffered saline for 20 min and then washed and incubated with phosphate-buffered saline. The full FOV diffraction-limited image in Fig. 7(a) shows that the 10× objectives capture a large number of cells. This property is crucial when monitoring, for example, the motility of live cancer cells.[43] However, as can be seen from magnified sections of diffraction-limited QPI in Figs. 7(b) and 7(d), the standard resolution of 10× objectives is insufficient for simultaneous observation of intracellular processes. Comparing the sections of diffraction-limited [Figs. 7(b) and 7(d)] and synthetic aperture [Figs. 7(c) and 7(e)] images, we see that our method provides, in addition to the large FOV, also, in many applications required, high resolution.

The benefits of the proposed method can be better understood from the following acquisition time discussion. We compare our synthetic aperture approach using 10× objectives (requires five to seven holograms) with the FOV scanning using 20× objectives (requires four holograms). First, we analyze the time consumption regardless of aspects interconnected with particular experimental situations and focus only on the impact of the exposure time and the position changing speed of the reference arm objective and

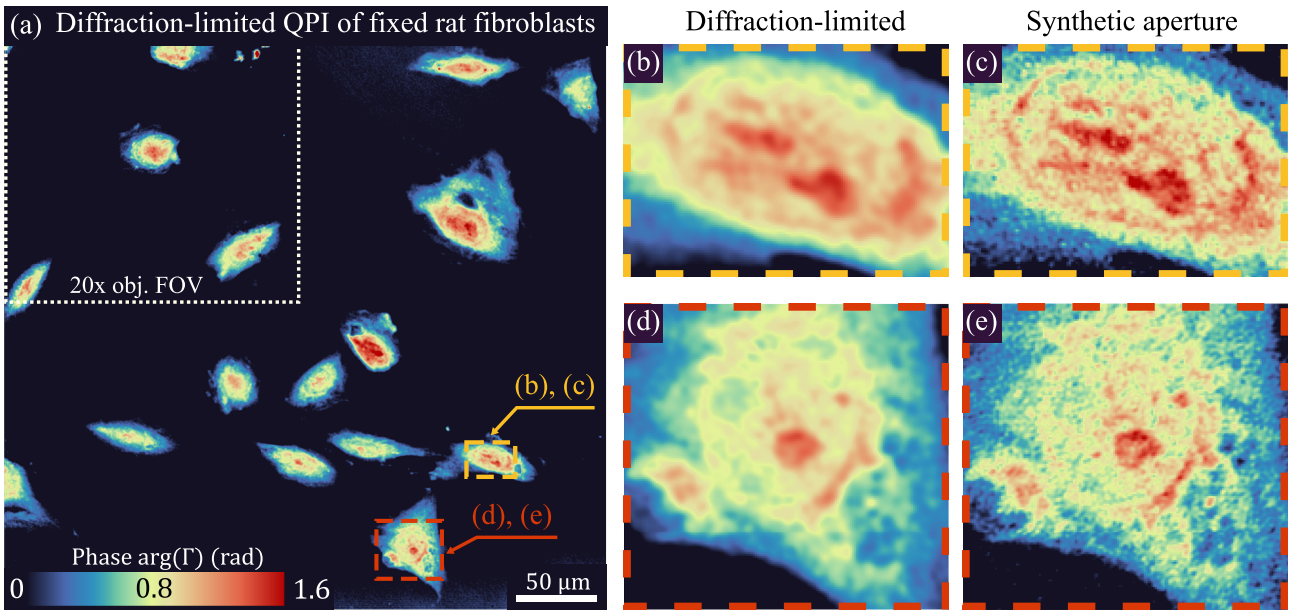

FIG. 7. Results of the proposed method for imaging of rat embryo fibroblasts. (a) Full FOV diffraction-limited QPI. (b) A section [marked by the yellow dashed line in (a)] of the diffraction-limited image. (c) A section [same as (b)] of the synthetic aperture image. (d) A section [marked by the red dashed line in (a)] of the diffraction-limited image. (e) A section [same as (d)] of the synthetic aperture image.

microscopy stage, and then, we discuss the limitations due to other experimental aspects of QPI. In the presented experiments, we used exposure time of 100ms. The speeds of modern piezo stages provide scanning speeds significantly over 20 mm/s. Therefore, with the speed of 20 mm/s, the time to change the position of the reference arm objective by 92 μm (from $\Delta\mathbf{q}_0$ to $\Delta\mathbf{q}_1$) is about 5 ms, and the time to move the microscopy stage by a distance 189 μm (FOV width for 20× objectives) is about 10 ms. The acquisition of seven holograms for the proposed approach with 10× objectives is in this case more time consuming than acquiring four neighboring fields of views with 20× objectives. We can make the proposed approach faster by increasing the illumination source power and using higher quality camera, which would allow us to reach exposure times of the order of milliseconds. As explained in Sec. III, the distance between $\Delta\mathbf{q}_j$ positions over which the reference objective must be shifted to the image by the illumination light scattered into different diffraction orders of the PG is inversely proportional to the distance z_d between the PG and the specimen. By placing the PG closer to the specimen, we can reduce the scanning time of the reference objective below 1 ms. It is important to note that more sophisticated mechanisms can be designed for the quick reference field manipulation, and this is subject of our future work. Therefore, when exposure times of the order of milliseconds can be reached the FOV scanning will start to present the bottleneck. Our method will then provide faster image acquisition than FOV scanning with higher NA objectives.

However, we see the potential of the proposed approach even with higher exposure times especially in specific experiments where mechanical specimen scanning is unwanted and where high resolution, long working distance, or depth of focus cannot be compromised. A long working distance is necessary, for example, when imaging a thick tissue,[31] cells in an extracellular matrix,[3,44] or a microfluidic channel. When using high NA objectives, a very sophisticated autofocus[45] has to be employed to optimize time between acquisitions. In addition, CCHM specific disadvantage is the need for slight readjustment of the microscope for different FOVs due to varying specimen thicknesses, which affect CCHM performance more significantly with higher NA objectives. QPI, in general, is prone to unstable surrounding environment; therefore, abrupt rapid microscopy stage movement may affect the phase image quality. For this reason, the commercial CCHM (Telight Q-phase) limits the speed of FOV position changing to allow for stabilization, which, in practice, dramatically reduces the speed of the FOV scanning method. It is important to note that the high acquisition speed is of interest mainly in the experimental situations when quasi-real-time acquisition is needed. This means that the specimen stage position changing in very short time intervals would result in continuous specimen vibrations. Even though it has been shown that short-term exposure to mechanical vibrations changes behavior of living cells minimally, long term mechanical stress can cause, for example, an increase in motility[46] or it can disrupt the collagen compactness of the extracellular matrix and corrupt the monitoring of tumor cell invasiveness.[3]

VI. CONCLUSION

In this paper, we have presented a method for generating a synthetic aperture QPI in holographic microscopes with partially coherent illumination. Our solution to overcoming the diffraction limit is very simple to implement because it does not require any changes in the microscope's optical system. It relies on oblique illumination provided by the diffraction on a simple phase grating placed in proximity of the specimen and intrinsic coherence-gating properties of the partially coherent light. We sequentially coherence gate the light scattered into each diffraction order of the PG, and we use the acquired images to synthesize quantitative phase images with significantly increased spatial frequency bandwidth. This paper presents a thorough theoretical treatment of the coherence-gated imaging process as well as a detailed methodology of the measurement. To the best of our knowledge, we utilize the coherence gate for the first time for a purpose different than imaging through or in turbid media.

We envision the proposed method to provide an easily implementable super-resolution QPI, which is particularly suitable for high-throughput biomedical applications. The possibility to obtain large FOV datasets with moderate-to-high spatial resolution and very high quantitative information quality can have a significant impact, for example, on stem cell research[4] or the development of migrastatics.[47] Furthermore, our work aims to satisfy the need for extensive high-quality datasets required for rapidly developing automated analysis using artificial intelligence.[5]

ACKNOWLEDGMENTS

The work was supported by the Grant Agency of the Czech Republic (Grant No. 21-01953S), the Specific Research grant of Brno University of Technology (Grant No. FSI-S-20-6353), and the MEYS CR (Large RI Project No. LM2018129 Czech-BioImaging). M.Ď. is a Brno Ph.D. Talent Scholarship holder—Funded by the Brno City Municipality—and is supported by the Specific Research grant of Brno University of Technology (Grant No. CEITEC VUT-J-21-7456). We thank Veronika Jůzová for help in the preparation of biological samples.

AUTHOR DECLARATIONS

Conflict of Interest

R.C. is a co-author of patents covering Q-Phase (EA 018804 B1, US 8526003 B2, JP 5510676 B2, CN102279555A, EP 2378244 B1, and CZ302491) and a recipient of related royalties from Telight.

DATA AVAILABILITY

The data that support the findings of this study are available from the corresponding author upon reasonable request.

REFERENCES

[1]P. Lang, K. Yeow, A. Nichols, and A. Scheer, "Cellular imaging in drug discovery," Nat. Rev. Drug Discovery **5**, 343–356 (2006).

[2]B. Gál, M. Veselý, J. Čolláková, M. Nekulová, V. Jůzová, R. Chmelík, and P. Veselý, "Distinctive behaviour of live biopsy-derived carcinoma cells unveiled using coherence-controlled holographic microscopy," PLoS One **12**, e0183399 (2017).

[3]O. Tolde, A. Gandalovičová, A. Křížová, P. Veselý, R. Chmelík, D. Rosel, and J. Brábek, "Quantitative phase imaging unravels new insight into dynamics of mesenchymal and amoeboid cancer cell invasion," Sci. Rep. **8**(1), 12020 (2018).

[4]M. R. Costa, F. Ortega, M. S. Brill, R. Beckervordersandforth, C. Petrone, T. Schroeder, M. Götz, and B. Berninger, "Continuous live imaging of adult neural stem cell division and lineage progression in vitro," Development **138**, 1057–1068 (2011).
[5]L. Strbkova, D. Zicha, and P. Vesely, "Automated classification of cell morphology by coherence-controlled holographic microscopy," J. Biomed. Opt. **22**, 086008 (2017).
[6]Y. Jo, H. Cho, S. Y. Lee, G. Choi, G. Kim, H.-s. Min, and Y. Park, "Quantitative phase imaging and artificial intelligence: A review," IEEE J. Sel. Top. Quantum Electron. **25**, 6800914 (2019).
[7]A. W. Lohmann, R. G. Dorsch, D. Mendlovic, C. Ferreira, and Z. Zalevsky, "Space–bandwidth product of optical signals and systems," J. Opt. Soc. Am. A **13**, 470 (1996).
[8]V. Micó, Z. Zalevsky, C. Ferreira, and J. García, "Superresolution digital holographic microscopy for three-dimensional samples," Opt. Express **16**, 19260–19270 (2008).
[9]V. Mico, O. Limon, A. Gur, Z. Zalevsky, and J. García, "Transverse resolution improvement using rotating-grating time-multiplexing approach," J. Opt. Soc. Am. A **25**, 1115–1129 (2008).
[10]T. Gutzler, T. R. Hillman, S. A. Alexandrov, and D. D. Sampson, "Coherent aperture-synthesis, wide-field, high-resolution holographic microscopy of biological tissue," Opt. Lett. **35**, 1136 (2010).
[11]M. Paturzo, F. Merola, S. Grilli, S. De Nicola, A. Finizio, and P. Ferraro, "Super-resolution in digital holography by a two-dimensional dynamic phase grating," Opt. Express **16**, 17107 (2008).
[12]S. Chowdhury, W. J. Eldridge, A. Wax, and J. A. Izatt, "Structured illumination multimodal 3D-resolved quantitative phase and fluorescence sub-diffraction microscopy," Biomed. Opt. Express **8**, 2496–2518 (2017).
[13]K. Wicker and R. Heintzmann, "Resolving a misconception about structured illumination," Nat. Photonics **8**, 342–344 (2014).
[14]Y. Park, W. Choi, Z. Yaqoob, R. Dasari, K. Badizadegan, and M. S. Feld, "Speckle-field digital holographic microscopy," Opt. Express **17**, 12285–12292 (2009).
[15]Y. Baek, K. Lee, and Y. Park, "High-resolution holographic microscopy exploiting speckle-correlation scattering matrix," Phys. Rev. Appl. **10**, 024053 (2018).
[16]Y. Choi, T. D. Yang, C. Fang-Yen, P. Kang, K. J. Lee, R. R. Dasari, M. S. Feld, and W. Choi, "Overcoming the diffraction limit using multiple light scattering in a highly disordered medium," Phys. Rev. Lett. **107**, 023902 (2011).
[17]W. Bishara, T.-W. Su, A. F. Coskun, and A. Ozcan, "Lensfree on-chip microscopy over a wide field-of-view using pixel super-resolution," Opt. Express **18**, 11181–11191 (2010).
[18]W. Xu, M. H. Jericho, I. A. Meinertzhagen, and H. J. Kreuzer, "Digital in-line holography for biological applications," Proc. Natl. Acad. Sci. U. S. A. **98**, 11301–11305 (2001).
[19]J. Garcia-Sucerquia, W. Xu, S. K. Jericho, P. Klages, M. H. Jericho, and H. J. Kreuzer, "Digital in-line holographic microscopy," Appl. Opt. **45**, 836–850 (2006).
[20]V. Micó and Z. Zalevsky, "Superresolved digital in-line holographic microscopy for high-resolution lensless biological imaging," J. Biomed. Opt. **15**, 046027 (2010).
[21]L. Granero, C. Ferreira, Z. Zalevsky, J. García, and V. Micó, "Single-exposure super-resolved interferometric microscopy by RGB multiplexing in lensless configuration," Opt. Lasers Eng. **82**, 104–112 (2016).
[22]G. Zheng, R. Horstmeyer, and C. Yang, "Wide-field, high-resolution Fourier ptychographic microscopy," Nat. Photonics **7**, 739–745 (2013).
[23]L. Tian, Z. Liu, L.-H. Yeh, M. Chen, J. Zhong, and L. Waller, "Computational illumination for high-speed *in vitro* Fourier ptychographic microscopy," Optica **2**, 904 (2015).
[24]J. R. Fienup, "Reconstruction of a complex-valued object from the modulus of its Fourier transform using a support constraint," J. Opt. Soc. Am. A **4**, 118–123 (1987).
[25]C. J. R. Sheppard, "Fundamentals of superresolution," Micron **38**, 165–169 (2007).
[26]C. Yuan, H. Zhai, and H. Liu, "Angular multiplexing in pulsed digital holography for aperture synthesis," Opt. Lett. **33**, 2356–2358 (2008).
[27]S. K. Mirsky and N. T. Shaked, "First experimental realization of six-pack holography and its application to dynamic synthetic aperture superresolution," Opt. Express **27**, 26708–26720 (2019).
[28]N. T. Shaked, V. Micó, M. Trusiak, A. Kuś, and S. K. Mirsky, "Off-axis digital holographic multiplexing for rapid wavefront acquisition and processing," Adv. Opt. Photonics **12**, 556–611 (2020).
[29]G. Dardikman and N. T. Shaked, "Is multiplexed off-axis holography for quantitative phase imaging more spatial bandwidth-efficient than on-axis holography? [Invited]," J. Opt. Soc. Am. A **36**, A1–A11 (2019).
[30]T. Slabý, P. Kolman, Z. Dostál, M. Antoš, M. Lošťák, and R. Chmelík, "Off-axis setup taking full advantage of incoherent illumination in coherence-controlled holographic microscope," Opt. Express **21**, 14747 (2013).
[31]M. Ďuriš and R. Chmelík, "Coherence gate manipulation for enhanced imaging through scattering media by non-ballistic light in partially coherent interferometric systems," Opt. Lett. **46**, 4486–4489 (2021).
[32]J. Á. Picazo-Bueno, Z. Zalevsky, J. García, and V. Micó, "Superresolved spatially multiplexed interferometric microscopy," Opt. Lett. **42**, 927 (2017).
[33]E. N. Leith and J. Upatnieks, "Holography with achromatic-fringe systems," J. Opt. Soc. Am **57**, 975 (1967).
[34]R. Chmelik, M. Slaba, V. Kollarova, T. Slaby, M. Lostak, J. Collakova, and Z. Dostal, "The role of coherence in image formation in holographic microscopy," Prog. Opt. **59**, 267–335 (2014).
[35]A. Y. Meshalkin, V. V. Podlipnov, A. V. Ustinov, and E. A. Achimova, "Analysis of diffraction efficiency of phase gratings in dependence of duty cycle and depth," J. Phys.: Conf. Ser. **1368**, 22047 (2019).
[36]L. Mandel and E. Wolf, *Optical Coherence and Quantum Optics* (Cambridge University Press, 1995), p. 1194.
[37]Y. Cotte, M. F. Toy, N. Pavillon, and C. Depeursinge, "Microscopy image resolution improvement by deconvolution of complex fields," Opt. Express **18**, 19462 (2010).
[38]K. Wicker, O. Mandula, G. Best, R. Fiolka, and R. Heintzmann, "Phase optimisation for structured illumination microscopy," Opt. Express **21**, 2032–2049 (2013).
[39]V. Micó, J. Zheng, J. Garcia, Z. Zalevsky, and P. Gao, "Resolution enhancement in quantitative phase microscopy," Adv. Opt. Photonics **11**, 135 (2019).
[40]H. Jiang, J. Zhao, J. Di, and C. Qin, "Numerically correcting the joint misplacement of the sub-holograms in spatial synthetic aperture digital Fresnel holography," Opt. Express **17**, 18836–18842 (2009).
[41]J. Bělín and J. Courtial, "Imaging with two skew ideal lenses," J. Opt. Soc. Am. A **36**, 132–141 (2019).
[42]T. Vicar, J. Balvan, J. Jaros, F. Jug, R. Kolar, M. Masarik, and J. Gumulec, "Cell segmentation methods for label-free contrast microscopy: Review and comprehensive comparison," BMC Bioinf. **20**, 360 (2019).
[43]C. D. Paul, P. Mistriotis, and K. Konstantopoulos, "Cancer cell motility: Lessons from migration in confined spaces," Nat. Rev. Cancer **17**, 131–140 (2017).
[44]A. Zoumi, A. Yeh, and Bj. Tromberg, "Imaging cells and extracellular matrix *in vivo* by using second-harmonic generation and two-photon excited fluorescence," Proc. Natl. Acad. Sci. U. S. A. **99**, 11014–11019 (2002).
[45]F. W. Schenk, N. Brill, U. Marx, D. Hardt, N. König, and R. Schmitt, "High-speed microscopy of continuously moving cell culture vessels," Sci. Rep. **6**, 34038 (2016).
[46]R. Hartmann-Petersen, P. S. Walmod, A. Berezin, V. Berezin, and E. Bock, "Individual cell motility studied by time-lapse video recording: Influence of experimental conditions," Cytometry **40**, 260–270 (2000).
[47]A. Gandalovičová, D. Rosel, M. Fernandes, P. Veselý, P. Heneberg, V. Čermák, L. Petruželka, S. Kumar, V. Sanz-Moreno, and J. Brábek, "Migrastatics—Anti-metastatic and anti-invasion drugs: Promises and challenges," Trends Cancer **3**, 391–406 (2017).

Chapter 8

Super-resolution in QPI allowed by superoscillations

In this section, we discuss the possibilities of the resolution improvement of CCHM utilizing superoscillations. Superoscillations are a counter-intuitive phenomenon that gives rise to wave oscillations locally faster than the highest Fourier component of the band-limited signal [115, 116]. A typical implementation of superoscillations in super-resolution imaging relies on a precisely engineered mask that, when illuminated by coherent light, creates a focal spot much smaller than allowed by the Abbe-Rayleigh limit [115]. However, direct imaging with a superoscillatory focal spot is not possible in practice due to high sideband intensity [117]. Rogers et al. [118] proposed a microscope setup with superoscillatory sample illumination and confocal detection with pinhole to suppress the light scattered from sidebands. They reported resolution improvement equivalent to 25% increase in numerical aperture.

In the course of the thesis, we have developed a novel method of producing and shaping a superoscillatory mutual coherence function, i.e., a superoscillatory coherence gate. This is possible only in partially coherent systems such as CCHM; to our best knowledge, it has not been investigated before. The imaging processes in CCHM resemble a confocal system because the CCHM point spread function (PSF) is a product of the coherence gate and the spot created by the objective lens in the object arm [12]. The standard role of the coherence gate in turbid media imaging is analogous to the detection pinhole of a confocal microscope. The coherence gate size is also diffraction-limited, but even our preliminary simulations suggested we can shape the coherence gate almost arbitrarily and even make it superoscillatory.

We use the coherence gate with a superoscillatory central spot and strong sidebands. Since the CCHM PSF is the product of the coherence gate and the Airy spot produced by the aperture of the objective lens in the object arm, the sidebands are significantly suppressed. As a result, the central spot can be sub-diffraction limited. Successful implementation of this concept into CCHM promises a huge advantage over the method proposed by Rogers et al. [118] by providing single-shot non-scanning super-resolution with at least the same resolution increase, i.e. 25%. Moreover, implementation into practice is expected to be very simple and straightforward.

Our coherence-gate shaping is based on the Fourier-transform relation between the incoherent source image in the front focal plane of the condenser lens and the mutual coherence function in its rear focal plane. In the theory of optical coherence,

this relation is known as the Van Cittert–Zernike theorem [35]. We expect to obtain appropriate source plane modulation by placing specially designed filters with complex transmittance in the reference arm plane conjugated with the source, which will result in shaping the coherence gate. A promising candidate for such a filter appears to be the Toraldo filters [119], composed of concentric complex annuli [120].

8.1 Single-shot super-resolution quantitative phase imaging allowed by coherence gate shaping

8.1.1 Motivation

Holography with partially coherent illumination is popular for optical sectioning by coherence-gating, providing speckle-free high-quality quantitative phase images (QPI). We build on the theory of partially coherent light and aim to develop coherence gate shaping inspired by optical superoscillation. Superoscillation gained popularity with the recent expansion of plasmonic metasurfaces. However, their applications to super-resolution imaging remain limited by unwanted sidelobes surrounding subdiffraction hotspots [115, 116, 121]. Recent works [118, 122] revealed that super-resolution microscopy could be achieved by demanding confocal filtration of the superoscillatory hotspots. Alternatively, the imaging limits an impractical small field of view given by the distance of the sidelobes. Thus, practical superoscillatory imaging remains a challenge for standard microscopy not yet approached by any QPI techniques.

While the synthetic aperture approach presented in Chapter 7 excels at increasing the resolution of low-NA objectives (large FOV moderate resolving power), the resolution improvement beyond diffraction limit is using superoscillations feasible also for high-NA objectives. Our preliminary results show that utilizing superoscillations in CCHM can provide single-shot super-resolved images. This means that the potential application of superoscillations to QPI will open new avenues in biomedical and dielectric metasurface research. We will be able to observe unseen features of live cells, and in addition to that, we will benefit from quantitative information provided by QPI. Also similarly as the synthetic aperture method described in detail in Chapter 7, the utilization of superoscillations for imaging with low-NA objectives would provide increased space-bandwidth product.

8.1.2 Outcomes

We demonstrate the implementation of superoscillatory coherence gate shaping in holography with partially coherent light, creating images composed of subdiffraction hotspots with suppressed sidelobes. During the imaging process, the sidelobes are mitigated in parallel throughout the entire field of view by intrinsic effects of the partially coherent illumination. The proposed method solves the problem of sidelobes in superoscillatory imaging, retains the quantitative information, and is thus the first to provide single-shot super-resolution QPI to the best of our knowledge. The practical

implementation builds on the fact that the point spread function of a partially coherent holographic system is a product of the coherence gating function (CGF) and the function describing the diffraction-limited image spot (typically Airy pattern). While the modulation of CGF delivers subdiffraction hotspots, the Airy pattern mitigates its sidelobes and mimics parallel confocal filtration of all image points. The resulting point spread function of the holographic system has a central peak narrower than the diffraction limit, while the strength of the sidelobes is negligible. We shape the CGF by manipulating the illumination in the plane optically conjugated with the light source by a specially designed mask of concentric annuli with varying complex transmissions. Our theory supports clear experimental evidence, showing single-shot super-resolved QPI with up to 19% resolving power improvement. The direct applicability demonstrates super-resolution QPI of phase resolution target and biological specimens.

8.1.3 Article 3

The article **Single-shot super-resolution quantitative phase imaging allowed by coherence gate shaping** was published in **APL Photonics** (2022 Impact factor: 5.6, Q1 in Optics) in March 2023.

APL Photonics ARTICLE scitation.org/journal/app

Single-shot super-resolution quantitative phase imaging allowed by coherence gate shaping

Cite as: APL Photon. 8, 046103 (2023); doi: 10.1063/5.0127950
Submitted: 25 September 2022 • Accepted: 10 March 2023 •
Published Online: 3 April 2023

Miroslav Ďuriš,[1,a)] Petr Bouchal,[1,2] and Radim Chmelík[1,2]

AFFILIATIONS

[1] CEITEC–Central European Institute of Technology, Brno University of Technology, Purkyňova 656/123, 61200 Brno, Czech Republic

[2] Institute of Physical Engineering, Faculty of Mechanical Engineering, Brno University of Technology, Technická 2896/2, 61669 Brno, Czech Republic

[a)] **Author to whom correspondence should be addressed:** miroslav.duris@ceitec.vutbr.cz

ABSTRACT

Biomedical and metasurface researchers repeatedly reach for quantitative phase imaging (QPI) as their primary imaging technique due to its high-throughput, label-free, quantitative nature. So far, very little progress has been made toward achieving super-resolution in QPI. However, the possible super-resolving QPI would satisfy the need for quantitative observation of previously unresolved biological specimen features and allow unprecedented throughputs in the imaging of dielectric metasurfaces. Here we present a method capable of real-time super-resolution QPI, which we achieve by shaping the coherence gate in the holographic microscope with partially coherent illumination. Our approach is based on the fact that the point spread function (PSF) of such a system is a product of the diffraction-limited spot and the coherence-gating function, which is shaped similarly to the superoscillatory hotspot. The product simultaneously produces the PSF with a super-resolution central peak and minimizes sidelobe effects commonly devaluating the superoscillatory imaging. The minimization of sidelobes and resolution improvement co-occur in the entire field of view. Therefore, for the first time, we achieve a single-shot widefield super-resolution QPI. We demonstrate here resolution improvement on simulated as well as experimental data. A phase resolution target image shows a resolving power improvement of 19%. Finally, we show the practical feasibility by applying the proposed method to the imaging of biological specimens.

I. INTRODUCTION

Far-field fluorescent super-resolution techniques such as stimulated emission depletion,[1] structured illumination microscopy,[2] photoactivated localization microscopy,[3] and stochastic optical reconstruction microscopy[4] have become, over recent years, a standard in biomedical imaging. These methods produce images with spatial resolution reaching values way below the diffraction limit of light. The techniques mentioned above exploit sub-diffraction limited imaging of non-linear specimen responses achieved by labeling with fluorescent dyes or quantum dots. Artificial labeling is also popular for providing a high degree of specificity. However, several studies have shown that labeling changes the behavior of the studied biological specimen.[5,6] Therefore, label-free imaging techniques are a more appropriate choice in many biomedical applications. No need for labeling also allows for studying artificial micro and nanostructures.[7,8] Nonetheless, breaking the diffraction limit in label-free imaging techniques is more challenging because of the missing non-linear specimen response.[9]

Quantitative phase imaging (QPI) has established an irreplaceable role among label-free imaging techniques thanks to its capability to quantitatively measure morphology and intrinsic specimen contrast with nanoscale sensitivity.[10] The possible super-resolution QPI will satisfy the need for quantitative observation of previously unresolved specimen features and allow increasing the space-bandwidth product (SBP),[11] crucial for high-throughput studies. High SBP is important in identifying rare events, for example, in drug discovery,[12] cancer-cell biology,[13,14] or stem-cell

research.[15] The recent development of automated data analysis and classification by artificial intelligence[16,17] exaggerates this ever-increasing demand for high-resolution quantitative data. So far, the proposed approaches to QPI super-resolution are based on oblique illumination,[18,19] structured illumination,[20] and speckle illumination,[21,22] which, combined with post-processing, provide synthetic images with an effectively enlarged numerical aperture (NA). These synthetic aperture methods enhance resolving power by essentially multiplexing the spatial-frequency content of the object spectrum into an unused degree of freedom in the system, sacrificing acquisition speed, quantitative information accuracy, or a field of view (FOV).

Recent advances in superoscillatory hotspot creation[23–25] that allowed the development of novel approaches to coherent label-free super-resolution microscopy could also be adopted for QPI. However, current implementations of superoscillations also sacrifice some of the valuable microscope properties similar to the synthetic aperture methods. Band-limited fields containing superoscillations oscillate locally faster than the highest Fourier component. When carried over to optical imaging, this means that the focal spot can be made much smaller than allowed by the Abbe–Rayleigh limit. This was first investigated in 1952 by di Francia,[26] but only recently have these principles been applied to practical microscopy.[27,28] A superoscillatory sub-diffraction limited focal hotspot can be produced, for example, by coherently illuminating a specially designed mask of concentric annuli of varying complex transmission and widths.[27] The concentric annuli mask design can push the central hotspot radius significantly beyond the diffraction limit, but at the cost of high-intensity sidelobes,[27] which degrade the image quality in standard wide-field imaging. An alternative approach to amplitude and phase modulation is the application of light states with spatially structured polarization, such as the focusing of radially and azimuthally polarized Laguerre–Gaussian beams.[29,30] The pioneering experimental research utilizing superoscillations initially demonstrated the super-resolution imaging only in a very small FOV[27] dictated by the distance of the first high-intensity sidelobe. To remove the FOV constraint, Rogers *et al.*[28] combined confocal detection with superoscillatory illumination. They create the super-resolution image thanks to the coherent illumination pattern with a sub-diffraction limited central hotspot and strong sidelobes. Subsequently, confocal detection eliminates the image distorting sidelobe effects at the cost of scanning the illumination pattern. Despite the great potential for resolution improvement, intensity imaging does not apply to most biological and other weakly scattering specimens and lacks quantitative information. Implementation of similar principles in QPI is thus a desirable yet challenging task due to the complexity and susceptibility of interferometric systems.

In this paper, we propose a method that does not have to sacrifice any of the favorable microscope properties to achieve super-resolved QPI. To the best of our knowledge, we show for the first time that partially coherent broad-source interferometers are capable of single-shot widefield super-resolution imaging by shaping the so-called coherence gate.[31] Our approach is based on the fact that the point spread function (PSF) of the partially coherent system is a product of the shaped coherence-gating function[19] (CGF) and the function describing the diffraction-limited image spot (Airy pattern). We shape the CGF by manipulating the illumination in the conjugated source plane similarly to the superoscillatory hotspot creation techniques. The product of the superoscillatory CGF with the Airy spot created by the objective in the object arm minimizes the sidelobes in the unbounded region while the CGF central peak delivers the super-resolving power. The minimization of sidelobes and resolution improvement co-occur in the entire field of view and allow single-shot widefield imaging. The imaging thus resembles confocal detection but with parallel filtration of all image points in the field of view. The images maintain quantitative phase information and extend the potential of superoscillations toward the QPI.

We first demonstrate the effects of the superoscillatory CGF using simulated data. Then, due to the highly aberrated pupil plane of our experimental setup, we focus in the experimental part on a limiting case between the superoscillatory and super-resolution CGF. In both situations, the hotspot width is below the Rayleigh criterion. The distinction criterion between the super-resolution function and the superoscillatory one was proposed by Huang *et al.*[24] (we provide more details on the definition of the superoscillatory and super-resolution focal spot in the supplementary material). We create the CGF in this limiting case by using a simple amplitude annular mask, which proves experimentally robust. We demonstrate experimentally QPI resolution enhancement using only the limiting case, but the principle of our method is extendable to the superoscillatory focal spot region, promising higher resolution improvement. An experiment with a phase resolution target shows a resolving power improvement of 19%, and we show practical feasibility by applying the proposed method to the imaging of biological specimens.

II. OPTICAL SETUP DESCRIPTION

The proposed principles generally apply to various partially coherent interferometric systems. Without loss of generality, we will further describe the optical setup and theoretical framework of the used coherence-controlled holographic microscope[32] (CCHM), commercially available as the Telight Q-Phase. The optical setup (see Fig. 1) is an adaptation of the Mach–Zehnder interferometer. It consists of an object and reference arm containing two optically equivalent microscope systems. This holographic setup guarantees off-axis hologram formation in the interference plane (IP) for broad sources of an arbitrary degree of coherence. The possibility of using

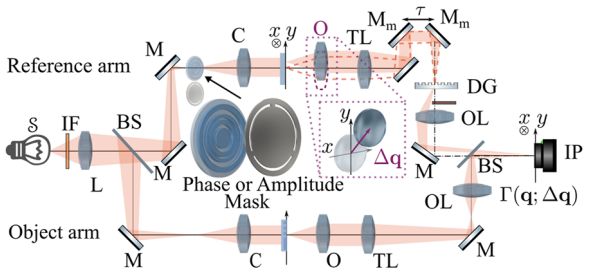

FIG. 1. Optical setup of the coherence-controlled holographic microscope: S, light source; IF, interference filter; L, relay lens; BS, beam splitters; M, mirrors; Mm, movable mirrors; C, condensers; O, objective lenses; TL, tube lenses; DG, diffraction grating; OL, output lenses; IP, interference plane.

partially coherent sources is provided by the diffraction grating (DG; transmission phase grating with groove frequency 150 mm^{-1}, blazed at 760 nm for the first diffraction order) implemented in the reference arm according to principles proposed by Leith and Upatnieks.[33] In our system, an LED (LED Engin LZ4-00R208, peak wavelength at 660 nm, power up to 2.9 W) is used for illumination to provide a spatially broad incoherent source, and the illuminating light is made quasi-monochromatic after passing the interference filter (IF) with a central wavelength of 660 and 10 nm full width at half maximum. The source is imaged by a pair of achromatic doublets (simplified as L in Fig. 1; focal lengths 63.5 and 350 mm) through a beam splitter (BS) to the front focal planes of the condensers (C; Nikon LWD condenser lenses, 0.52 NA, with adjustable aperture stop). This plane in object and reference arms and respective condenser properties can be described according to Ref. 34 by the pupil functions $P_{\mathrm{Co}}(\mathbf{K}_{\mathrm{t}})$ and $P_{\mathrm{Cr}}(\mathbf{K}_{\mathrm{t}})$, respectively, where $\mathbf{K}_{\mathrm{t}} = (K_x, K_y)$ is the transverse wave vector of a plane wave behind condensers. The coordinates of $\mathbf{K}_{\mathrm{t}}$ are proportional to the respective source point (pupil-plane) coordinates. For this reason, pupil properties can be characterized by a function of $\mathbf{K}_{\mathrm{t}}$. We use reduced wave vector notation $|\mathbf{K}| = 1/\lambda$, where λ is the wavelength of light, and $\mathbf{K} = (\mathbf{K}_{\mathrm{t}}, K_z) = (K_x, K_y, K_z)$, where $K_z = \sqrt{|\mathbf{K}|^2 - |\mathbf{K}_{\mathrm{t}}|^2}$. We modulate the condenser pupil planes to produce the sub-diffraction limited coherence gate, as explained in Sec. III. The fundamental image properties also depend on the parameters of the object and reference arm objective lenses (O; Nikon Plan Fluorite Objectives, 10x/0.3 NA/16 mm WD) in combination with tube lenses (TL; Nikon, focal length 200 mm), characterized by the pupil functions $P_{\mathrm{Oo}}(\mathbf{K}_{\mathrm{t}})$ and $P_{\mathrm{Or}}(\mathbf{K}_{\mathrm{t}})$. Stepper and piezo motors provide fine adjustment of the microscope optical components, which we use for the measurement of the coherence-gating function. The holograms are recorded in IP using an Andor Zyla 4.2 sCMOS camera.

As shown in Fig. 1, we place the phase or amplitude mask in one or both of the front focal planes of the condensers. We designed the masks to shape the CGF when imaging with 10x/0.3 NA objective lenses. In simulations, we assume the phase mask is composed of concentric annuli, with the phase shift being either 0 or π radians. We also carried out simulations with the amplitude mask subsequently used in experiments. The amplitude mask is a single annulus cut by a laser cutter into a metal sheet. An inner circle of the annulus has a diameter of 16.4 mm. The outer circle diameter is about 18 mm, but more importantly, the pupil diameter in the front focal plane of the condensers is limited by the aperture stop to ~17.3 mm (corresponding to 0.30 condenser NA).

III. THEORY

Quantitative phase information can be extracted from the measured holograms. As we work with the off-axis holographic setup, we reconstruct holograms by carrier removal in the Fourier plane.[32] In partially coherent systems, the hologram cross-correlation term depends on the transversal displacement $\Delta\mathbf{q} = (\Delta x, \Delta y)$ and relative time-delay τ of the object-scattered and reference fields. The cross-correlation function is conveniently described by a mutual coherence function[31] (MCF) $\Gamma(\mathbf{q}, \mathbf{q} - \Delta\mathbf{q}, \tau)$ of the two fields, where $\mathbf{q} = (x, y)$ is the position of a point in the image plane specified by the coordinates of the optically conjugated point in the object plane. The modulus and phase image for particular $\Delta\mathbf{q}$ and τ are obtained as the modulus and argument of Γ, respectively. The interferometric imaging for a given time-delay τ and transverse displacement $\Delta\mathbf{q}$ can be called a partial MCF measurement.[31] The complete MCF is acquired by measuring and reconstructing holograms for all accessible $\Delta\mathbf{q}$ and τ. In this work, we use in experiments quasi-monochromatic illumination. Therefore, the influence of temporal coherence is minimal and manifests mainly as a speckle noise reduction. We set $\tau = 0$ at the beginning of each experiment. The standard imaging conditions in low-coherence interferometers are when $\Delta\mathbf{q} = (0, 0)$. We use this setting for the majority of our experiments. However, as we show further, the complete MCF measurement and hence the manipulation with $\Delta\mathbf{q}$ is crucial for a measurement of the coherence-gating function. Our further analysis will stay within the limits of scalar wave approximation. More detailed mathematical derivations of the following equations are provided in the supplementary material. If we assume complete spatial source incoherence, $\tau = 0$, and $\Delta\mathbf{q}$ as a parameter, the expression for the measured MCF, has according to Ref. 19, the form

$$\Gamma(\mathbf{q}; \Delta\mathbf{q}) = t(\mathbf{q}) \otimes h(\mathbf{q}; \Delta\mathbf{q}), \tag{1}$$

where $t(\mathbf{q})$ is a complex transmission of the specimen, the symbol $\otimes$ denotes convolution, and $h(\mathbf{q}; \Delta\mathbf{q}) = p_{\mathrm{o}}(\mathbf{q})\mathcal{G}^*(\mathbf{q} - \Delta\mathbf{q})$ is a PSF of the imaging system, where $p_{\mathrm{o}}(\mathbf{q}) = \iint P_{\mathrm{Oo}}(\mathbf{K}_{\mathrm{t}}) \exp(2\pi i \mathbf{K}_{\mathrm{t}} \cdot \mathbf{q}) \mathrm{d}^2\mathbf{K}_{\mathrm{t}}$ and

$$\mathcal{G}(\mathbf{q}) = \iint P^*_{\mathrm{Co}}(\mathbf{K}_{\mathrm{t}}) P_{\mathrm{Cr}}(\mathbf{K}_{\mathrm{t}}) P_{\mathrm{Or}}(\mathbf{K}_{\mathrm{t}}) \exp(2\pi i \mathbf{K}_{\mathrm{t}} \cdot \mathbf{q}) \mathrm{d}^2\mathbf{K}_{\mathrm{t}}. \tag{2}$$

We call function $\mathcal{G}(\mathbf{q})$ the coherence-gating function[19,31] (CGF). The integration regions in $p_{\mathrm{o}}(\mathbf{q})$ and $\mathcal{G}(\mathbf{q})$ are given by the extent of the pupil functions $P_{\mathrm{Oo}}(\mathbf{K}_{\mathrm{t}})$ and $P^*_{\mathrm{Co}}(\mathbf{K}_{\mathrm{t}}) P_{\mathrm{Cr}}(\mathbf{K}_{\mathrm{t}}) P_{\mathrm{Or}}(\mathbf{K}_{\mathrm{t}})$, respectively. These boundaries define the band-limit of $p_{\mathrm{o}}(\mathbf{q})$ and $\mathcal{G}(\mathbf{q})$. The CGF provides filtering of multiply scattered light when imaging through turbid media.[31,32] Here we do not intend to use the coherence gate to mitigate unwanted scattering effects, but we unconventionally shape the coherence gate to obtain sub-diffraction limited PSF. For circular apertures, we can describe the CGF $\mathcal{G}(\mathbf{q})$ and $p_{\mathrm{o}}(\mathbf{q})$ using the Bessel function of the first kind as $\mathcal{G}(\mathbf{q}) = 2J_1(\mu)/(\mu)$ and $p_{\mathrm{o}}(\mathbf{q}) = 2J_1(\nu)/(\nu)$, where $\mu = 2\pi K \mathrm{NA}_{\mathrm{C}} |\mathbf{q}|$ and $\nu = 2\pi K \mathrm{NA}_{\mathrm{O}} |\mathbf{q}|$, with $\mathrm{NA}_{\mathrm{C}} \leq \mathrm{NA}_{\mathrm{O}}$.

To obtain the sub-diffraction limited resolution of QPI $\arg\{\Gamma[\mathbf{q}; \Delta\mathbf{q} = (0, 0)]\}$, systems's PSF $h(\mathbf{q}) = p_{\mathrm{o}}(\mathbf{q})\mathcal{G}^*(\mathbf{q})$ must have the central peak radius below the diffraction limit. To maintain quantitative phase information in the image, the sidelobes of the PSF must also be negligible. Numerous studies[24,26,27,35] have shown that a superoscillatory focal spot can be created by coherently illuminating a phase or amplitude mask composed of concentric annuli of different widths and complex transmission. Superoscillations are then formed by constructive and destructive interference near the focal spot. As we use partially coherent illumination in our microscope system, it is not possible to create the superoscillatory focal spot observable in the field's intensity by interference as proposed for coherent light. However, we can adopt the principles normally applied to coherent systems and shape the system's PSF, the product of $\mathcal{G}^*(\mathbf{q} - \Delta\mathbf{q})$ and $p_{\mathrm{o}}(\mathbf{q})$, by altering one or both of these functions. By modulating the pupil function $P_{\mathrm{Oo}}(\mathbf{K}_{\mathrm{t}})$ of

the object-arm objective, we can affect $p_o(\mathbf{q})$, but as Eq. (2) suggests, we have more options for $\mathcal{G}(\mathbf{q})$, because this function can be shaped by modulating one or more pupil functions $P_{Co}(\mathbf{K}_t)$, $P_{Cr}(\mathbf{K}_t)$ and $P_{Or}(\mathbf{K}_t)$ of the condensers and the reference-arm objective, respectively. It is also experimentally easier to modulate the condenser pupil planes. Therefore, we will focus on shaping the CGF. However, similar results can be achieved by shaping $p_o(\mathbf{q})$, or both at the same time. Equation (2) describing CGF formation shows that $\mathcal{G}(\mathbf{q})$ can be shaped similarly to coherent imaging even though the plane waves $\exp(2\pi i\mathbf{K}_t \cdot \mathbf{q})$ superposed in Eq. (2) are mutually incoherent. The $P^*_{Co}(\mathbf{K}_t)P_{Cr}(\mathbf{K}_t)P_{Or}(\mathbf{K}_t)$ dictates whether these plane waves are constructively or destructively superposed. This allows us to use approaches designed for coherent imaging even in a system operating with partially coherent light. The expression in Eq. (2) is in fact van Cittert–Zernike theorem,[36] which describes the relationship between the mutual coherence function (CGF in our case) and the modulation of the pupil plane for partially coherent broad source illumination. As we can control the constructiveness of the plane wave superposition, theoretically, it should be possible to create observable superoscillations in partially coherent systems. However, not in the field's intensity but in the mutual coherence of two fields (in our case, the CGF), hence the need for the interferometric system.

For demonstration, we simulate the imaging and calculate the PSFs for three cases with different CGF shapes: first, the diffraction-limited case, when a full unmodulated condenser aperture is assumed; second, the limiting case of the superoscillation, when the amplitude mask with narrow annulus is used and the CGF is represented by the Bessel function $J_0(2\pi K\mathrm{NA}_C|\mathbf{q}|)$; and third, the case with a superoscillatory CGF produced by three-zone phase modulation. For all three cases, we assume that the $p_o(\mathbf{q})$ function is the Airy pattern for $\mathrm{NA}_O = \mathrm{NA}_C = 0.30$, and this function is represented in Figs. 2(a)–2(c) by yellow dashed curves. The CGF $\mathcal{G}(\mathbf{q})$ for the diffraction limited case is also the Airy pattern [see the red dashed curve in Fig. 2(a)]. The CCHM PSF [the product of $p_o(\mathbf{q})$ and $\mathcal{G}(\mathbf{q})$] is in Figs. 2(a)–2(c) depicted by solid purple curves. The CGF described by $J_0(2\pi K\mathrm{NA}_C|\mathbf{q}|)$, shown in Fig. 2(b), can be produced in the Köhler arrangement by an annular incoherent source with an infinitesimally narrow annulus and a radius corresponding to the condenser numerical aperture NA_C. Our phase modulation approach [Fig. 2(c)] to the creation of superoscillatory CGF is inspired by the results from Ref. 35. We assume modulation of $P_{Cr}(\mathbf{K}_t)$ by concentric annuli with phase modulation being either 0 or π. We have found by a few adjustments and visual evaluation that a superoscillatory CGF can be created by a three-zone annular modulation produced in the following manner: two circles with radii corresponding to $0.35\mathrm{NA}_C$ and $0.72\mathrm{NA}_C$ define the geometry of the three zones, while the phase modulation is 0 for the inner-most and outer-most zones, and the middle annulus has the phase shift of π radians. The full width at half maximum of the central peak and the first zero value of the PSF define the system's resolving power. The three-zone phase modulation and annular amplitude modulation (annular source) of the pupil function $P_{Cr}(\mathbf{K}_t)$ produce the CGF with the sub-diffraction limited central peak at the cost of stronger sidelobes [see the red dashed curves in Figs. 2(b) and 2(c)]. It is important to note that even though these functions themselves are superoscillatory, if the PSF with such strong sidelobes is used directly for imaging, it produces unwanted image artifacts that corrupt the improved resolving power.[37] However, as we demonstrate, the partially coherent systems provide an elegant way to suppress the sidelobe effects.

The Airy spot created by the objective in the object arm has a broad central peak with weak side lobes. As shown in this section, the PSF of the system (the solid purple curves in Fig. 2) is the product of the CGF and the Airy pattern. In both annular source [Fig. 2(b)] and phase-modulated [Fig. 2(b)] condenser pupil cases, the CGF central peak dictates the sub-diffraction limited properties of the focal spot, and sidelobes are attenuated by weak sidelobes of the Airy pattern distribution. Therefore, these approaches should provide sub-diffraction limited powers and deliver single-shot super-resolution images.

We performed imaging simulations comparing three cases corresponding to Figs. 2(a)–2(c) to evaluate the phase imaging performance. We simulated the phase resolution target imaging as a coherent convolution of its complex transmission function by the calculated PSFs, and the simulated phase images are shown in Figs. 3(a)–3(c). The insets in Figs. 3(b) and 3(c) show the potential experimental design of the masks producing the simulated modulation corresponding to Figs. 2(b) and 2(c). The smallest resolved element in the diffraction-limited case is element 5 from group −2. In the superoscillatory case [Fig. 3(c)], the smallest resolved element is number 1 from group −1, and for the annular pupil [Fig. 3(b)], this element can be considered resolved with very poor contrast. The cross-sections of the features of element 6 from group −2 in Fig. 3(d) show that this element is not resolved in a diffraction-limited image but well resolved in both the annular pupil and superoscillatory cases. However, the superoscillatory PSF produces an image with significantly better contrast. The feature width of element 1 from

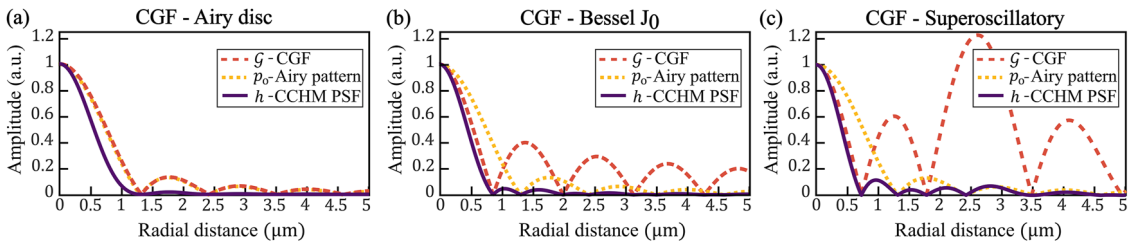

FIG. 2. The point spread function (PSF) is the product of the coherence-gating function (CGF) and the Airy pattern. (a) The standard imaging condition with a full aperture condenser. (b) An annular pupil condenser produces sub-diffraction limited CGF. (c) Phase modulated pupil plane delivers superoscillatory CGF and super-resolution PSF.

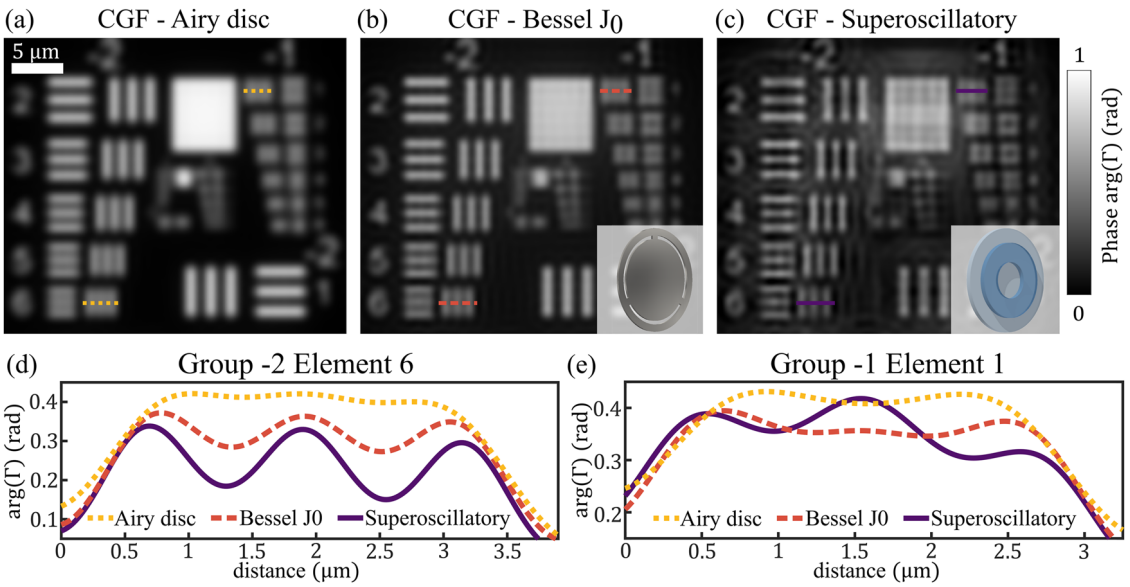

FIG. 3. Numerical simulations of phase resolution target imaging show that the superoscillatory coherence-gating function (CGF) created by phase modulation provides higher resolving powers, but amplitude modulation is more robust in experimental situations. (a) Diffraction-limited quantitative phase image (QPI) of the phase resolution target computed for the full aperture condenser pupil. (b) QPI of the resolution target for amplitude-modulated condenser pupil plane. (c) QPI of the resolution target corresponding to the case of superoscillatory CGF created by phase modulation. (d) and (e) Profiles of cross-sections through element 6 of group −2 and element 1 of group −1, respectively. More details about our simulations can be found in the supplementary material.

group −1 is ~20% lower than the feature width of element 5 from group −2. We can conclude that the resolution improvement is slightly less than 20% because the lines of element 1 from group −1 have very poor contrast. As can be seen by comparing Figs. 3(b) and 3(c) and the cross-sections in Fig. 3(e), the contrast is better in the superoscillatory case. We expected the resolution for the case with superoscillatory CGF to be better because the annular pupil produces the limiting case CGF between superoscillatory and sub-diffraction limited ones. Even though we achieve higher resolving power with superoscillatory CGF, the overall image quality of the superoscillatory case is lower due to incomplete sidelobe attenuation. It is important to note that, for simplicity of demonstration, we have not used any sophisticated methods to optimize the condenser pupil function. Generation of superoscillatory hotspots with state-of-the-art parameters usually employs iterative and computationally expensive procedures such as particle swarm,[27] genetic algorithm,[38] or phase retrieval[39] optimizations. We expect to achieve higher resolution improvement and better phase image quality by employing one of these methods.

Additionally to spot size, the superoscillatory focal spot design always involves optimizing the ratio of the central peak and the sidelobe intensities.[29] Without taking this into account, practical applications of superoscillatory focusing for imaging are not possible due to the poor signal-to-noise ratio. A similar principle applies also to optimizing the parameters of the CGF. To reconstruct QPI from holograms with reasonable phase quality, the hologram contrast must be higher than the noise levels. When phase modulation of the pupil planes is used, the amplitude of the CGF is redistributed from the central peak to the sidelobes due to the destructive interference of light from the object and reference arm. The hologram contrast is proportional to the central peak amplitude of the PSF $h(\mathbf{q})$. Therefore, one must consider the achievable hologram contrast when designing the superoscillatory CGF. We have discovered that for the combination of high-quality phase and highest resolution improvement, it is important to optimize the whole product of $p_o(\mathbf{q})$ and $\mathcal{G}(\mathbf{q})$, not only CGF $\mathcal{G}(\mathbf{q})$. Consequently, the objective function for an optimization procedure must be defined differently than for a standard intensity imaging system. One can easily deduce that the optimal solutions found for fluorescence and confocal microscopy do not apply to the proposed case.

The creation of the superoscillatory CGF requires a very precise design of the phase modulation of $P_{\mathrm{Cr}}(\mathbf{K}_t)$. This is easily achieved in simulations when unaberrated pupils are assumed. However, we have to account for aberrations in real experimental systems and compensate for them while also providing the modulation for CGF shaping. Aberrations can be perceived in the context of the theory outlined in this section as modulations of pupil functions $P_{\mathrm{Co}}(\mathbf{K}_t)$, $P_{\mathrm{Cr}}(\mathbf{K}_t)$, and $P_{\mathrm{Or}}(\mathbf{K}_t)$ in Eq. (2). As the creation of superoscillations is very susceptible to even subtle deviations from the designed phase shift provided by the phase mask, the aberrations prevent us from using simple symmetric phase masks in real systems. Due to the difficulty of measuring and compensating for aberration in our system, we chose to utilize the amplitude mask in experiments instead of the phase mask.

As Fig. 3 shows, the effect of the modulation by the mask can be assessed indirectly from the system's imaging performance. However, we can directly measure the shape of the CGF. When no specimen is present in the object arm, and we assume that the objective

lens in the object arm has negligible aberrations, then we get from Eq. (1) the following expression:

$$\Gamma_B(\Delta\mathbf{q}) = \mathcal{G}^*(\Delta\mathbf{q}). \tag{3}$$

This equation shows that the complete MCF measurement $\Gamma_B(\Delta\mathbf{q})$ with no objects present in both arms provides us with information about the CGF as a function of $\Delta\mathbf{q}$. Therefore, we will use the measurement described by Eq. (3) to directly evaluate the CGF shape created by the designed mask.

IV. EXPERIMENTAL RESULTS

We experimentally demonstrate the feasibility of the principles proposed in Sec. III utilizing the optical setup with $10x/NA_O = 0.30$ objectives and the condenser aperture set to $NA_C = 0.30$. Our initial efforts to take advantage of the phase modulation provided by simple phase masks similar to the one in the inset of Fig. 3(c) have shown that aberrations in our system prevent the CGF from being shaped as designed. However, amplitude modulation by an annular mask [shown in Fig. 3(b) and the design parameters in Sec. II] has proven relatively robust to the aberrated pupils. Therefore, we used it in the presented experiments. We placed two identical amplitude masks into the reference and object arms to balance the light powers in the arms in order to achieve a better contrast of holographic fringes. The total power fraction that is transmitted to the specimen through the mask can be calculated as a ratio of the transparent mask area to the full aperture area. As stated in Sec. II, the diameter of the inner circle of the amplitude annulus is 16.4 mm, and the effective condenser aperture diameter in the front focal plane of the condenser is 17.3 mm. Therefore, the ratio of the light transmitted to the light incident on the mask is ~0.1. Even though 90% light loss seems significant, our LED source is powerful enough to compensate for that. In experiments with the amplitude mask, we operated the source at about 10% of its maximum power, while the camera exposure times did not exceed tens of milliseconds.

First, we evaluate whether the amplitude modulation provides us with a CGF resembling the designed shape of $J_0(2\pi K NA_C|\mathbf{q}|)$. We measured the complete MCF for a case with [Fig. 4(b)] and without [Fig. 4(a)] the mask placed in the front focal plane of condensers, i.e., for annular and full aperture. We measured the complete MCF by acquiring and reconstructing a hologram for each reference arm objective position from a predefined grid. The grid of $\Delta\mathbf{q}$ positions for each CGF measurement was the same, and we used a 41×41 grid centered at $\Delta\mathbf{q} = 0$ with a 0.3 μm spacing. We display in Fig. 4 the normalized modulus of the MCF for a FOV point $\mathbf{q} = (0, 0)$ μm. Comparing the measured CGF in Figs. 4(a) and 4(b) with the corresponding simulated CGF in Figs. 4(c) and 4(d), we see the effects of the aberrated pupils (mainly due to the off-axis holographic setup). The measurement with full condenser apertures in Fig. 4(a) shows clear signs of a primary coma aberration. We can conclude that the annular aperture is not very susceptible to aberrations, as there is a notable agreement between the measured [Fig. 4(b)] and simulated [Fig. 4(d)] CGF profiles. We have fitted the Airy function to the measured CGF amplitude, shown in Fig. 4(a), with significantly better sampling than the measured data. Then, we determined the full width at half maximum (FWHM) of the central peak to be 1.60 μm. Similarly, we fitted the data obtained for the case with

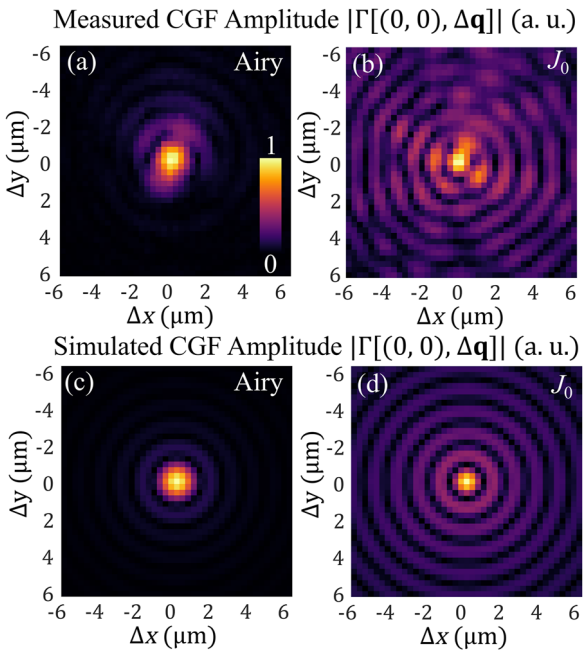

FIG. 4. Comparison of the measured and simulated coherence-gating function (CGF) shows the effects of optical aberrations in the experimental setup on CGF. (a) Measured CGF for full condenser aperture. (b) Measured sub-diffraction limited CGF for annular condenser aperture. (c) Simulated CGF for full condenser aperture. (d) Simulated CGF for annular condenser aperture.

the annular aperture, shown in Fig. 4(b), with the J_0 function and determined the FWHM to be 1.08 μm. The measurement in Fig. 4(b) and the FWHM values show that the CGF created by the amplitude mask has a central peak narrower than the one of the Airy pattern. Therefore, the CGF is, in this sense, sub-diffraction limited.

The complete measurement of the MCF, as shown in Fig. 4, can be used to assess the optical system aberrations. This indicates that we could design and manufacture a phase mask that would simultaneously compensate for aberrations and provide the modulation needed for superoscillatory CGF. However, we decided to postpone these efforts for follow-up work as the current experimental setup limits the practical feasibility of this approach. To obtain

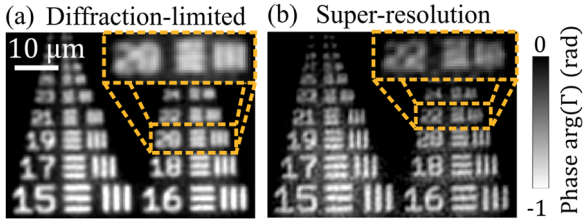

FIG. 5. Comparison of (a) the diffraction-limited image (obtained with the full aperture condenser) and (b) the super-resolution image (obtained with the annular mask) of the phase resolution target.

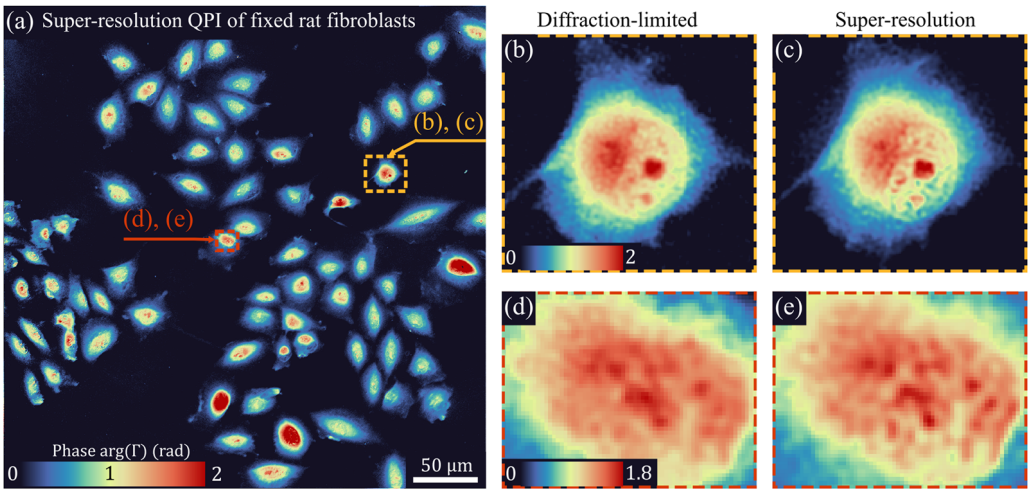

FIG. 6. Results of the proposed method for imaging rat embryo fibroblasts. (a) Full FOV super-resolution QPI obtained with sub-diffraction limited CGF. (b) A section [marked by the yellow dashed line in (a)] of the diffraction-limited image. (c) A section [the same as in (b)] of the super-resolution image. (d) A section [marked by the red dashed line in (a)] of the diffraction-limited image. (e) A section [the same as in (d)] of the super-resolution image.

the superoscillatory response provided by a specifically manufactured asymmetric mask, one must place it precisely in the correct position. Several degrees of freedom (parameters) must be set to optimize the phase mask position: axial, x-y transversal, and two angular positions. For this, we would need automatic alignment with a feedback loop. The amplitude mask is easier to align as we can partially see its effect in the intensity image formed by light from a single microscope arm. However, the phase mask effect is not visible in the intensity image. We can take advantage of the complete MCF measurement described by Eq. (3) to assess the phase mask effect and its position. Unfortunately, this measurement in the current setup takes tens of minutes. Therefore, it is currently unsuitable for implementing it into a necessary automatic alignment procedure with a feedback loop.

We imaged a phase resolution target with both the full and annular condenser apertures to assess the improvement in the resolving power. The full (unmodulated) aperture phase image in Fig. 5(a) represents the diffraction-limited image. The phase image in Fig. 5(b) is obtained using the amplitude mask, which we refer to as a super-resolution image. The insets in both images show details of the smallest resolved features in each image. A visual comparison of Fig. 5(a) with Fig. 5(b) shows a clear resolution improvement. The smallest resolvable features in the diffraction-limited image [Fig. 5(a)] marked by the number 20 are 0.65 μm wide. This means the resolution with the full aperture is ~1.3 μm. Whereas the smallest resolvable features in the super-resolution image [Fig. 5(b)] are marked by the number 22 and are 0.53 μm wide. The improvement of the spatial resolution to about 1.06 μm is a gain of ~19%.

Next, we show the performance of our method when used to image complex specimens such as rat embryo fibroblasts in Fig. 6. The presented experiment involved LW13K2 cells from a cell line of spontaneously transformed rat embryo fibroblasts LW13 of the inbred strain Lewis. Cells were cultivated at 37 °C in a humidified incubator with 3.5% CO_2 in standard Minimum Essential Medium Eagle with Hanks' salts supplemented with 10% fetal bovine serum, 20 μM gentamicin, and 2 mM L-glutamine. Subsequently, the cells were fixed using 4% formaldehyde in phosphate-buffered saline for 20 min, then washed and incubated in phosphate-buffered saline. Again, we imaged the specimen with and without the annular amplitude masks in the front focal condenser planes. The QPI in Fig. 6(a) experiences super-resolution throughout the entire FOV and can be obtained from a single hologram measurement. Having a large FOV and sufficient resolution for cell segmentation or even observation of intracellular processes is crucial when monitoring, for example, the motility of live cancer cells.[40] Comparing the sections of diffraction-limited [Figs. 6(b) and 6(d)] and super-resolution [Figs. 6(c) and 6(e)] images, we see that our method provides the improved resolution required in many applications in addition to the large FOV.

V. CONCLUSION

In this paper, we have presented a method for single-shot label-free super-resolution QPI in holographic microscopes with partially coherent illumination. Our solution to overcoming the diffraction limit is straightforward to implement because it does not require any changes to the microscope's optical system. The proposed method relies on the intrinsic partially coherent illumination properties giving rise to the coherence-gating. We propose that by introducing a phase or amplitude modulation of the planes conjugated with the light source, e.g., the front focal plane of the condenser, we can generate sub-diffraction limited CGF. We demonstrate for the first time theoretically and in numerical simulations a superoscillatory CGF shaped by phase and amplitude modulation. Due to experimental challenges, we chose to experimentally show the proposed principles using modulation provided by an amplitude mask, which has

proven more robust to optical aberrations than phase masks. We demonstrated almost 20% resolving power improvement in phase imaging of the model specimen and complex objects such as cancer cells. However, the theoretical spatial resolution improvement is not in principle limited, and we expect to obtain significantly over 20% resolution gain with more sophisticated modulation techniques. For example, a spatial light modulator can be introduced into the optical setup to provide simultaneous compensation of pupil aberrations and the modulation needed to create the superoscillatory CGF.

We envision our method delivering an easily implementable super-resolution QPI, particularly suitable for high-throughput biomedical applications. Further extension of the CGF shaping theory beyond the limits of the scalar approximation will allow reaching an unprecedented spatial resolution of QPI. The possibility to monitor a large FOV in real-time with spatial super-resolution and very high quantitative information quality can significantly impact cancer research,[14,41] as previously unseen intracellular processes can now be observed. Furthermore, our work satisfies the need for time-series high-quality datasets required for rapidly developing automated analysis using artificial intelligence.[16,42]

SUPPLEMENTARY MATERIAL

See the supplementary material for a detailed derivation of the equations in Sec. III, a definition of the superoscillatory and super-resolution focal spot that is assumed throughout this article, and additional information about simulations producing some of the presented data.

ACKNOWLEDGMENTS

The work was supported by the Grant Agency of the Czech Republic (Grant No. 21-01953S), the specific research grants of Brno University of Technology (Grant Nos. FSI-S-20-6353 and FSI-S-23-8389), and the MEYS CR (Large RI Project No. LM2023050 Czech-BioImaging). We thank Veronika Jůzová for help in the preparation of biological samples.

AUTHOR DECLARATIONS

Conflict of Interest

R.C. is a co-author of patents covering Q-Phase (EA 018804 B1, US 8526003 B2, JP 5510676 B2, CN102279555A, EP 2378244 B1, and CZ302491) and a recipient of related royalties from Telight.

Author Contributions

Miroslav Ďuriš: Conceptualization (equal); Data curation (lead); Formal analysis (lead); Investigation (lead); Methodology (equal); Software (lead); Visualization (lead); Writing – original draft (lead); Writing – review & editing (equal). **Petr Bouchal**: Conceptualization (equal); Funding acquisition (equal); Investigation (equal); Methodology (equal); Supervision (equal); Validation (equal); Writing – review & editing (equal). **Radim Chmelík**: Conceptualization (equal); Formal analysis (equal); Funding acquisition (equal); Project administration (equal); Resources (equal); Supervision (equal); Writing – review & editing (equal).

DATA AVAILABILITY

The data that support the findings of this study are available from the corresponding author upon reasonable request.

REFERENCES

[1]S. W. Hell and J. Wichmann, "Breaking the diffraction resolution limit by stimulated emission: Stimulated-emission-depletion fluorescence microscopy," Opt. Lett. **19**(11), 780–782 (1994).
[2]R. Heintzmann and T. Huser, "Super-resolution structured illumination microscopy," Chem. Rev. **117**(23), 13890–13908 (2017).
[3]S. Manley, J. M. Gillette, G. H. Patterson, H. Shroff, H. F. Hess, E. Betzig, and J. Lippincott-Schwartz, "High-density mapping of single-molecule trajectories with photoactivated localization microscopy," Nat. Methods **5**(2), 155–157 (2008).
[4]M. J. Rust, M. Bates, and X. Zhuang, "Sub-diffraction-limit imaging by stochastic optical reconstruction microscopy (STORM)," Nat. Methods **3**(10), 793–796 (2006).
[5]U. Schnell, F. Dijk, K. A. Sjollema, and B. N. G. Giepmans, "Immunolabeling artifacts and the need for live-cell imaging," Nat. Methods **9**(2), 152–158 (2012).
[6]Z. Xiaoling, L. Yuchi, Z. Meirong, N. Xiaobing, and H. Yinguo, "Calibration of a fringe projection profilometry system using virtual phase calibrating model planes," J. Opt. A: Pure Appl. Opt. **7**(4), 192–197 (2005).
[7]P. Bouchal, P. Dvořák, J. Babocký, Z. Bouchal, F. Ligmajer, M. Hrtoň, V. Křápek, A. Faßbender, S. Linden, R. Chmelík, and T. Šikola, "High-resolution quantitative phase imaging of plasmonic metasurfaces with sensitivity down to a single nanoantenna," Nano Lett. **19**(2), 1242–1250 (2019).
[8]T. Fordey, P. Bouchal, P. Schovánek, M. Baránek, Z. Bouchal, P. Dvořák, M. Hrtoň, K. Rovenská, F. Ligmajer, R. Chmelík, and T. Šikola, "Single-shot three-dimensional orientation imaging of nanorods using spin to orbital angular momentum conversion," Nano Lett. **21**(17), 7244–7251 (2021).
[9]K. Wicker and R. Heintzmann, "Resolving a misconception about structured illumination," Nat. Photonics **8**(5), 342–344 (2014).
[10]Y. Park, C. Depeursinge, and G. Popescu, "Quantitative phase imaging in biomedicine," Nat. Photonics **12**(10), 578–589 (2018).
[11]A. W. Lohmann, R. G. Dorsch, D. Mendlovic, C. Ferreira, and Z. Zalevsky, "Space–bandwidth product of optical signals and systems," J. Opt. Soc. Am. A **13**(3), 470 (1996).
[12]P. Lang, K. Yeow, A. Nichols, and A. Scheer, "Cellular imaging in drug discovery," Nat. Rev. Drug Discovery **5**(4), 343–356 (2006).
[13]B. Gál, M. Veselý, J. Čolláková, M. Nekulová, V. Jůzová, R. Chmelík, and P. Veselý, "Distinctive behaviour of live biopsy-derived carcinoma cells unveiled using coherence-controlled holographic microscopy," PLoS One **12**(8), e0183399 (2017).
[14]O. Tolde, A. Gandalovičová, A. Křížová, P. Veselý, R. Chmelík, D. Rosel, and J. Brábek, "Quantitative phase imaging unravels new insight into dynamics of mesenchymal and amoeboid cancer cell invasion," Sci. Rep. **8**(1), 012020 (2018).
[15]M. R. Costa, F. Ortega, M. S. Brill, R. Beckervordersandforth, C. Petrone, T. Schroeder, M. Götz, and B. Berninger, "Continuous live imaging of adult neural stem cell division and lineage progression *in vitro*," Development **138**(6), 1057–1068 (2011).
[16]L. Strbkova, D. Zicha, P. Vesely, and R. Chmelik, "Automated classification of cell morphology by coherence-controlled holographic microscopy," J. Biomed. Opt. **22**(8), 1–9 (2017).
[17]Y. Jo, H. Cho, S. Y. Lee, G. Choi, G. Kim, H.-s. Min, and Y. Park, "Quantitative phase imaging and artificial intelligence: A review," IEEE J. Sel. Top. Quantum Electron. **25**(1), 1–14 (2019).

[18]V. Micó, Z. Zalevsky, C. Ferreira, and J. García, "Superresolution digital holographic microscopy for three-dimensional samples," Opt. Express **16**(23), 19260–19270 (2008).
[19]M. Ďuriš, P. Bouchal, K. Rovenská, and R. Chmelík, "Coherence-encoded synthetic aperture for super-resolution quantitative phase imaging," APL Photonics **7**(4), 046105 (2022).
[20]S. Chowdhury, W. J. Eldridge, A. Wax, and J. A. Izatt, "Structured illumination multimodal 3D-resolved quantitative phase and fluorescence sub-diffraction microscopy," Biomed. Opt. Express **8**(5), 2496–2518 (2017).
[21]Y. Park, W. Choi, Z. Yaqoob, R. Dasari, K. Badizadegan, and M. S. Feld, "Speckle-field digital holographic microscopy," Opt. Express **17**(15), 12285–12292 (2009).
[22]Y. Baek, K. Lee, and Y. Park, "High-resolution holographic microscopy exploiting speckle-correlation scattering matrix," Phys. Rev. Appl. **10**(2), 024053 (2018).
[23]F. M. Huang and N. I. Zheludev, "Super-resolution without evanescent waves," Nano Lett. **9**(3), 1249–1254 (2009).
[24]K. Huang, H. Ye, J. Teng, S. P. Yeo, B. Luk'yanchuk, and C.-W. Qiu, "Optimization-free superoscillatory lens using phase and amplitude masks," Laser Photonics Rev. **8**(1), 152–157 (2014).
[25]G. Chen, Z.-Q. Wen, and C.-W. Qiu, "Superoscillation: From physics to optical applications," Light: Sci. Appl. **8**(1), 56 (2019).
[26]G. T. di Francia, "Super-gain antennas and optical resolving power," Il Nuovo Cimento **9**(3), 426–438 (1952).
[27]E. T. F. Rogers, J. Lindberg, T. Roy, S. Savo, J. E. Chad, M. R. Dennis, and N. I. Zheludev, "A super-oscillatory lens optical microscope for subwavelength imaging," Nat. Mater. **11**(5), 432–435 (2012).
[28]E. T. F. Rogers, S. Quraishe, K. S. Rogers, T. A. Newman, P. J. S. Smith, and N. I. Zheludev, "Far-field unlabeled super-resolution imaging with superoscillatory illumination," APL Photonics **5**(6), 066107 (2020).
[29]Y. Kozawa, D. Matsunaga, and S. Sato, "Superresolution imaging via superoscillation focusing of a radially polarized beam," Optica **5**(2), 86–92 (2018).
[30]X. Liu, W. Yan, Z. Nie, Y. Liang, Y. Wang, Z. Jiang, Y. Song, and X. Zhang, "Longitudinal magnetization superoscillation enabled by high-order azimuthally polarized Laguerre-Gaussian vortex modes," Opt. Express **29**(16), 26137–26149 (2021).
[31]M. Ďuriš and R. Chmelík, "Coherence gate manipulation for enhanced imaging through scattering media by non-ballistic light in partially coherent interferometric systems," Opt. Lett. **46**(18), 4486–4489 (2021).
[32]T. Slabý, P. Kolman, Z. Dostál, M. Antoš, M. Lošťák, and R. Chmelík, "Off-axis setup taking full advantage of incoherent illumination in coherence-controlled holographic microscope," Opt. Express **21**(12), 14747–14762 (2013).
[33]E. N. Leith and J. Upatnieks, "Holography with achromatic-fringe systems," J. Opt. Soc. Am. **57**(8), 975 (1967).
[34]R. Chmelik, M. Slaba, V. Kollarova, T. Slaby, M. Lostak, J. Collakova, and Z. Dostal, "The role of coherence in image formation in holographic microscopy," Prog. Opt. **59**, 267–335 (2014).
[35]N. Reza and L. Hazra, "Toraldo filters with concentric unequal annuli of fixed phase by evolutionary programming," J. Opt. Soc. Am. A **30**(2), 189–195 (2013).
[36]L. Mandel and E. Wolf, *Optical Coherence and Quantum Optics* (Cambridge University Press, 1995).
[37]C. Snoeyink and S. Wereley, "Single-image far-field subdiffraction limit imaging with axicon," Opt. Lett. **38**(5), 625–627 (2013).
[38]K. S. Rogers, K. N. Bourdakos, G. H. Yuan, S. Mahajan, and E. T. F. Rogers, "Optimising superoscillatory spots for far-field super-resolution imaging," Opt. Express **26**(7), 8095–8112 (2018).
[39]A. Sanjeev, N. Shabairou, A. Attar, D. Scherbaum, Y. Kapellner, M. Sinvani, and Z. Zalevsky, "Generation and manipulation of superoscillatory hotspots using virtual fourier filtering and CTF shaping," Sci. Rep. **10**(1), 4755 (2020).
[40]C. D. Paul, P. Mistriotis, and K. Konstantopoulos, "Cancer cell motility: Lessons from migration in confined spaces," Nat. Rev. Cancer **17**(2), 131–140 (2017).
[41]J. Balvan, A. Krizova, J. Gumulec, M. Raudenska, Z. Sladek, M. Sedlackova, P. Babula, M. Sztalmachova, R. Kizek, R. Chmelik, and M. Masarik, "Multimodal holographic microscopy: Distinction between apoptosis and oncosis," PLoS One **10**(3), e0121674 (2015).
[42]L. Strbkova, B. B. Carson, T. Vincent, P. Vesely, and R. Chmelik, "Automated interpretation of time-lapse quantitative phase image by machine learning to study cellular dynamics during epithelial–mesenchymal transition," J. Biomed. Opt. **25**(8), 086502 (2020).

Single-shot super-resolution quantitative phase imaging allowed by coherence gate shaping

Miroslav Ďuriš,[1] Petr Bouchal[1, 2] and Radim Chmelík[1, 2]
[1)] *CEITEC – Central European Institute of Technology, Brno University of Technology, Purkyňova 656/123, 61200 Brno, Czech Republic*
[2)] *Institute of Physical Engineering, Faculty of Mechanical Engineering, Brno University of Technology, Technická 2896/2, 61669 Brno, Czech Republic*

(*Electronic mail: miroslav.duris@ceitec.vutbr.cz)

Supplementary Information

I. MATHEMATICAL DERIVATION OF THE COHERENCE-GATING FUNCTION IN PARTIALLY COHERENT HOLOGRAPHIC MICROSCOPE

Our mathematical derivations are based on the works[1,2]. For more general derivation of the 3D coherent transfer function and 3D point spread functions (PSF) of a partially coherent interferometric system see work done by Chmelik et al.[1]. Here we assume that the optical system is an adaptation of the Mach-Zehnder interferometer as depicted in Fig. 1 of the manuscript. We assume that object and reference arm contain two optically equivalent microscope systems. Standard off-axis holographic setups require highly coherent illumination in order to achieve interference in the whole field of view. However, our experimental setup puts principles proposed by Leith[3] in practice, which guarantees off-axis hologram formation in the interference plane for broad sources of an arbitrary degree of coherence. Therefore, we can further assume fully spatially incoherent quasi-monochromatic illumination in our derivations. The hologram intensity $\mathrm{i}(\mathbf{q})$ recorded by the camera in the interference plane at the point $\mathbf{q} = (x, y)$ can be described as

$$\mathrm{i}(\mathbf{q}) = \iint_{-\infty}^{\infty} |P_{\mathrm{Cr}}(\mathbf{K}_\mathrm{t})h_\mathrm{r}(\mathbf{q}) + P_{\mathrm{Co}}(\mathbf{K}_\mathrm{t})h_\mathrm{o}(\mathbf{q})|^2 \mathrm{d}^2\mathbf{K}_\mathrm{t} = \iint_{-\infty}^{\infty} P_{\mathrm{Cr}}^2(\mathbf{K}_\mathrm{t})h_\mathrm{r}^2(\mathbf{q}) + P_{\mathrm{Co}}^2(\mathbf{K}_\mathrm{t})h_\mathrm{o}^2(\mathbf{q}) + P_{\mathrm{Cr}}(\mathbf{K}_\mathrm{t})h_\mathrm{r}(\mathbf{q})P_{\mathrm{Co}}^*(\mathbf{K}_\mathrm{t})h_\mathrm{o}^*(\mathbf{q}) + P_{\mathrm{Cr}}^*(\mathbf{K}_\mathrm{t})h_\mathrm{r}^*(\mathbf{q})P_{\mathrm{Co}}(\mathbf{K}_\mathrm{t})h_\mathrm{o}(\mathbf{q})\mathrm{d}^2\mathbf{K}_\mathrm{t}, \quad \text{(S1)}$$

where $h_\mathrm{r}(\mathbf{q})$ and $h_\mathrm{o}(\mathbf{q})$ is the optical response of the reference and object arm observed in the interference plane to the illumination by a point source producing a plane wave with the transversal wave vector $\mathbf{K}_\mathrm{t} = (K_x, K_y)$ behind the condensers. We use reduced wave vector notation $|\mathbf{K}| = 1/\lambda$, where λ is the wavelength of light, and $\mathbf{K} = (\mathbf{K}_\mathrm{t}, K_z) = (K_x, K_y, K_z)$, where $K_z = \sqrt{|\mathbf{K}|^2 - |\mathbf{K}_\mathrm{t}|^2}$. Next, $P_{\mathrm{Cr}}(\mathbf{K}_\mathrm{t})$ and $P_{\mathrm{Co}}(\mathbf{K}_\mathrm{t})$ are pupil functions[1] of the condensers in the reference and object arm, respectively. As we deal with the broad source we integrate over its area. This is indicated by the double integral in Eq. (S1). The integration is limited by the extent of the smaller pupil function of $P_{\mathrm{Cr}}(\mathbf{K}_\mathrm{t})$ and $P_{\mathrm{Co}}(\mathbf{K}_\mathrm{t})$. The interference law gives us four terms, from which the first two are intensity terms, and the third and fourth term are the so-called interference terms. The holographic setup allows us to easily retrieve by spatial filtering in Fourier plane one of the two interferometric terms. So, for example, we take the fourth term. In the partially coherent systems (our case) we can refer to this term as the mutual coherence function (MCF) Γ between the object and reference arm[2]. In addition to position $\mathbf{q}$, the MCF depends also on the transversal displacement $\Delta\mathbf{q} = (\Delta x, \Delta y)$ and can be for a case, when a planar object is placed in the object arm expressed as

$$\Gamma(\mathbf{q};\Delta\mathbf{q}) = \iint_{-\infty}^{\infty}\iint_{-\infty}^{\infty} P_{\mathrm{Cr}}^{*}(\mathbf{K}_\mathrm{t})P_{\mathrm{Or}}^{*}(\mathbf{K}_\mathrm{t})P_{\mathrm{Co}}(\mathbf{K}_\mathrm{t})P_{\mathrm{Oo}}(\mathbf{K}_\mathrm{t}+\mathbf{Q}_\mathrm{o})T_\mathrm{o}(\mathbf{Q}_\mathrm{o})\mathrm{e}^{2\pi\mathrm{i}(\mathbf{Q}_\mathrm{o}\cdot\mathbf{q}+\mathbf{K}_\mathrm{t}\cdot\Delta\mathbf{q})}\mathrm{d}^2\mathbf{K}_\mathrm{t}\,\mathrm{d}^2\mathbf{Q}_\mathrm{o}\,, \quad \text{(S2)}$$

where $P_{\mathrm{Oo}}(\mathbf{K}_\mathrm{t})$ and $P_{\mathrm{Or}}(\mathbf{K}_\mathrm{t})$ are pupil functions of the objectives in the object and reference arm, respectively. The planar object has a spatial frequency spectrum $T_\mathrm{o}(\mathbf{Q}_\mathrm{o})$, where $\mathbf{Q}_\mathrm{o} = (X, Y)$ is spatial frequency. After a bit of manipulation one can obtain simplified expression for MCF in the following form

$$\Gamma(\mathbf{q};\Delta\mathbf{q}) = t(\mathbf{q})\otimes h(\mathbf{q};\Delta\mathbf{q}), \quad \text{(S3)}$$

where $t(\mathbf{q})$ is a complex transmission of the specimen (the Fourier transform of $T_\mathrm{o}(\mathbf{Q}_\mathrm{o})$), the symbol $\otimes$ denotes convolution and $h(\mathbf{q};\Delta\mathbf{q})$ is a PSF of the imaging system. The PSF of the whole interferometric system can be decomposed into a product of two functions as follows

$$h(\mathbf{q};\Delta\mathbf{q}) = p_\mathrm{o}(\mathbf{q})\mathcal{G}^{*}(\mathbf{q}-\Delta\mathbf{q}), \quad \text{(S4)}$$

where $p_\mathrm{o}(\mathbf{q}) = \iint P_{\mathrm{Oo}}(\mathbf{K}_\mathrm{t})\exp(2\pi\mathrm{i}\mathbf{K}_\mathrm{t}\cdot\mathbf{q})\,\mathrm{d}^2\mathbf{K}_\mathrm{t}$ is the image of a coherent point source in the specimen plane of the object arm produced by the object arm objective and

$$\mathcal{G}(\mathbf{q}) = \iint P_{\mathrm{Co}}^{*}(\mathbf{K}_\mathrm{t})P_{\mathrm{Cr}}(\mathbf{K}_\mathrm{t})P_{\mathrm{Or}}(\mathbf{K}_\mathrm{t})\exp(2\pi\mathrm{i}\mathbf{K}_\mathrm{t}\cdot\mathbf{q})\,\mathrm{d}^2\mathbf{K}_\mathrm{t}\,. \quad \text{(S5)}$$

We call function $\mathcal{G}(\mathbf{q})$ the coherence-gating function (CGF).

II. MEASUREMENT OF THE COHERENCE-GATING FUNCTION

To show the possibility of measuring CGF we start derivation from Eq. (S2). We want to show that it is possible to measure CGF if no specimen is present in the object arm. To simulate such a situation, we substitute the spatial frequency spectrum $T_\mathrm{o}(\mathbf{Q}_\mathrm{o})$ of the specimen in the object arm by the Dirac delta function $\delta(\mathbf{Q}_\mathrm{o}-\boldsymbol{o})$, where $\boldsymbol{o} = (0,0)$**.** So for a blank object arm we obtain the MCF in a form

$$\Gamma(\mathbf{q};\Delta\mathbf{q}) = \iint_{-\infty}^{\infty}\iint_{-\infty}^{\infty} P_{\mathrm{Cr}}^{*}(\mathbf{K}_\mathrm{t})P_{\mathrm{Or}}^{*}(\mathbf{K}_\mathrm{t})P_{\mathrm{Co}}(\mathbf{K}_\mathrm{t})P_{\mathrm{Oo}}(\mathbf{K}_\mathrm{t}+\mathbf{Q}_\mathrm{o})\delta(\mathbf{Q}_\mathrm{o}-\boldsymbol{o})\mathrm{e}^{2\pi\mathrm{i}(\mathbf{Q}_\mathrm{o}\cdot\mathbf{q}+\mathbf{K}_\mathrm{t}\cdot\Delta\mathbf{q})}\mathrm{d}^2\mathbf{K}_\mathrm{t}\,\mathrm{d}^2\mathbf{Q}_\mathrm{o}\,, \quad \text{(S6)}$$

which reduces by integrating over $\mathbf{Q}_\mathrm{o}$ to

$$\Gamma(\mathbf{q};\Delta\mathbf{q}) = \iint_{-\infty}^{\infty} P_{\mathrm{Cr}}^{*}(\mathbf{K}_\mathrm{t})P_{\mathrm{Or}}^{*}(\mathbf{K}_\mathrm{t})P_{\mathrm{Co}}(\mathbf{K}_\mathrm{t})P_{\mathrm{Oo}}(\mathbf{K}_\mathrm{t})\mathrm{e}^{2\pi\mathrm{i}\mathbf{K}_\mathrm{t}\cdot\Delta\mathbf{q}}\mathrm{d}^2\mathbf{K}_\mathrm{t}\,. \quad \text{(S7)}$$

Now in real experimental situation we strive to use in the object arm of the microscope an objective with minimal aberrations. Therefore, we assume that object arm objective pupil function $P_{\mathrm{Oo}}(\mathbf{K}_\mathrm{t})$ is modulated negligibly in comparison to other pupil functions in Eq. (S7). Then setting $P_{\mathrm{Oo}}(\mathbf{K}_\mathrm{t}) = 1$ we obtain MCF in the following form

$$\Gamma(\mathbf{q};\Delta\mathbf{q}) = \iint_{-\infty}^{\infty} P_{\mathrm{Cr}}^{*}(\mathbf{K}_\mathrm{t})P_{\mathrm{Or}}^{*}(\mathbf{K}_\mathrm{t})P_{\mathrm{Co}}(\mathbf{K}_\mathrm{t})\mathrm{e}^{2\pi\mathrm{i}\mathbf{K}_\mathrm{t}\cdot\Delta\mathbf{q}}\mathrm{d}^2\mathbf{K}_\mathrm{t} = \mathcal{G}^{*}(\Delta\mathbf{q}), \quad \text{(S8)}$$

which shows that we can measure the CGF for a particular optical setup by measuring holograms for positions $\Delta\mathbf{q}$**.**

III. COHERENT SOURCE AND ITS EFFECT ON THE COHERENCE-GATING FUNCTION

Having a coherent source means that the specimen is illuminated only by a single plane wave. Therefore, to illustrate this, we multiply the integrand of the Eq. (S5) by a delta function $\delta(\mathbf{K}_\mathrm{t} - \boldsymbol{o})$, where $\boldsymbol{o} = (0,0)$. We obtain

$$\mathcal{G}(\mathbf{q}) = \iint P^*_{\mathrm{Co}}(\mathbf{K}_\mathrm{t}) P_{\mathrm{Cr}}(\mathbf{K}_\mathrm{t}) P_{\mathrm{Or}}(\mathbf{K}_\mathrm{t}) \delta(\mathbf{K}_\mathrm{t} - \boldsymbol{o}) \exp\left(2\pi \mathrm{i} \mathbf{K}_\mathrm{t} \cdot \mathbf{q}\right) \mathrm{d}^2\mathbf{K}_\mathrm{t} \,. \tag{S9}$$

After carrying out integration the $\mathcal{G}(\mathbf{q})$ function reduces to a constant and the PSF of the system becomes $h(\mathbf{q}; \Delta\mathbf{q}) = p_\mathrm{o}(\mathbf{q})$. The PSF is for a coherent illumination also independent of the transversal field shift $\Delta\mathbf{q}$ of the reference and object arm fields.

IV. SUPER-RESOLUTION VS SUPEROSCILLATORY REGIME OF A FOCAL SPOT

In this manuscript we adopt the definition of the superoscillatory spot in the context of optical focusing proposed by Huang et al.[4] The spot sizes (central peak of a focal spot) in orange area in Fig. S1 are called super-resolution ones because their diameters are below the Rayleigh resolution criterion (black curve in Fig. S1). The the zero-order Bessel function $J_0(2\pi K \mathrm{NA}_\mathrm{C}|\mathbf{q}|)$ of the first kind (orange curve in Fig. S1) has the central peak radius $0.38 K \mathrm{NA}_\mathrm{C}$. And a spot that has the central peak narrower than the $J_0(2\pi K \mathrm{NA}_\mathrm{C}|\mathbf{q}|)$ function can be referred to as a super-oscillatory spot. We carried out simulations and experiments with the coherence-gating functions corresponding to three positions on the white dashed line in Fig. S1. One corresponding to the diffraction-limited case, second corresponds to the limiting case $J_0(2\pi K \mathrm{NA}_\mathrm{C}|\mathbf{q}|)$ between super-resolution and super-oscillatory focal spot; and third, we present in the manuscript simulations with the superoscillatory CGF.

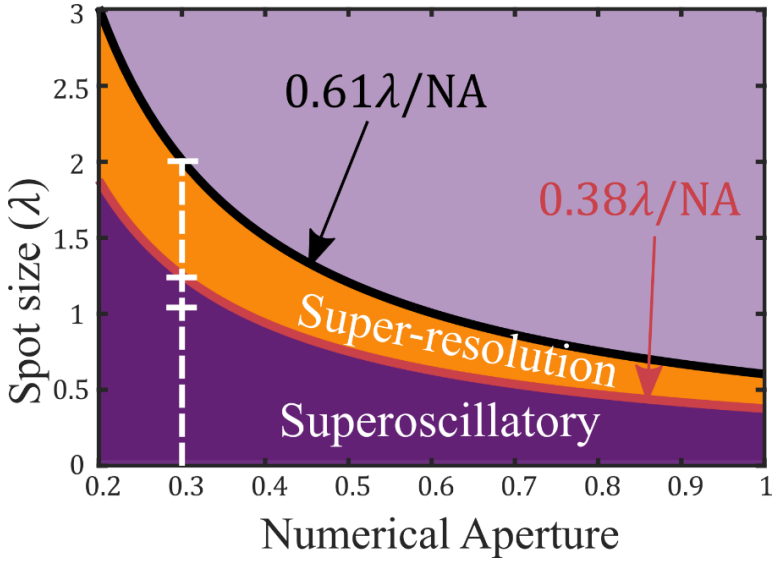

Figure S1. Superoscillatory criterion in optical focusing according to Huang et al.[4] The spot size as a function of numerical aperture. The two curves, which are the Rayleigh (black) and superoscillatory (orange) criterions, divide the focusing spot into three parts: sub-resolved (light violet), super-resolution (orange) and superoscillation (dark violet).

V. SIMULATION DETAILS

First, we simulated the coherence-gating function and PSF cross-sections using an approach presented in Ref. [5] modified to our case. Then the cross-sections presented in Fig. 2 were used to create 2D PSFs. Imaging simulation (depicted in Fig. 3 of the manuscript) was done simply by convolving the complex transmission of the resolution target by the PSFs. We assumed in simulations for both PSF design and imaging simulation by convolution a 2048×2048 pixel grid with pixel side size of $\lambda/40$, where $\lambda = 0.650$ μm. We imitated the real experiment, so we set $\mathrm{NA_C} = \mathrm{NA_O} = 0.30$.

We simulated the amplitude annulus mask by setting the inner circle radius of the transparent area to $0.9\mathrm{NA_C}$, and the outer to $1.0\mathrm{NA_C}$.

The three-zone phase mask producing superoscillatory CGF was simulated with radii of the circles corresponding $0.35\mathrm{NA_C}$, $0.72\mathrm{NA_C}$, $1.0\mathrm{NA_C}$. The phase modulation was 0 for the inner-most and outer-most zone, and the middle annulus had the phase shift of π radians.

VI. EXAMPLE HOLOGRAMS

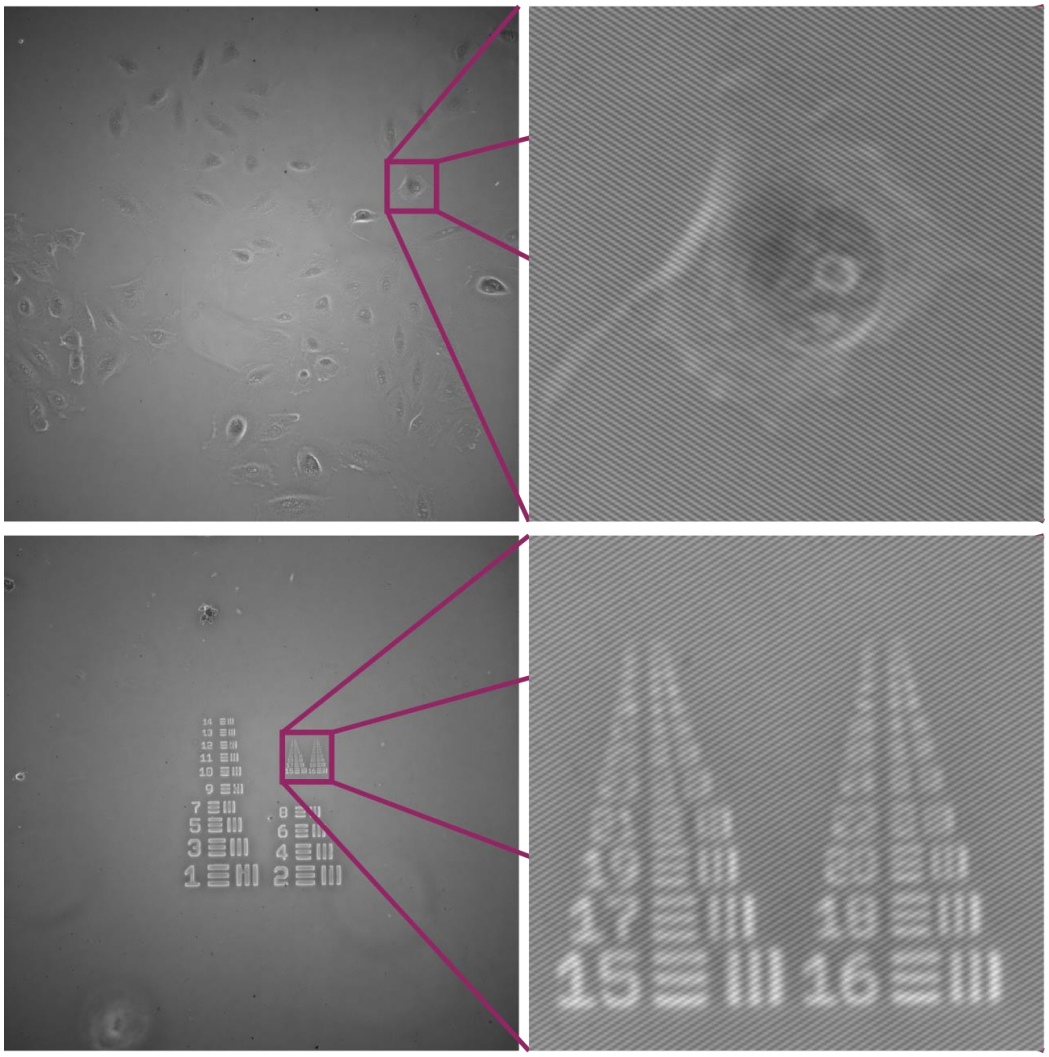

Figure S2. Example images of holograms (intensity) acquired using annular mask in the condenser pupil plane.

BIBLIOGRAPHY

(1) Chmelik, R.; Slaba, M.; Kollarova, V.; Slaby, T.; Lostak, M.; Collakova, J.; Dostal, Z. The Role of Coherence in Image Formation in Holographic Microscopy. *Progress in Optics* **2014**, *59*, 267–335. https://doi.org/10.1016/B978-0-444-63379-8.00005-2.

(2) Ďuriš, M.; Chmelík, R. Coherence Gate Manipulation for Enhanced Imaging through Scattering Media by Non-Ballistic Light in Partially Coherent Interferometric Systems. *Opt. Lett.* **2021**, *46* (18), 4486–4489. https://doi.org/10.1364/OL.432484.

(3) Leith, E. N.; Upatnieks, J. Holography with Achromatic-Fringe Systems. *J Opt Soc Am* **1967**, *57* (8), 975. https://doi.org/10.1364/JOSA.57.000975.

(4) Huang, K.; Ye, H.; Teng, J.; Yeo, S. P.; Luk'yanchuk, B.; Qiu, C.-W. Optimization-Free Superoscillatory Lens Using Phase and Amplitude Masks. *Laser Photon Rev* **2014**, *8* (1), 152–157. https://doi.org/https://doi.org/10.1002/lpor.201300123.

(5) Reza, N.; Hazra, L. Toraldo Filters with Concentric Unequal Annuli of Fixed Phase by Evolutionary Programming. *J. Opt. Soc. Am. A* **2013**, *30* (2), 189–195. https://doi.org/10.1364/JOSAA.30.000189.

Chapter 9

3D object refractive index reconstruction

Imaging of biological cells and tissues is an inherent part of biological research and medical diagnosis. Digital holographic microscopy has proven to be a valuable method for the investigation of these biological specimens by providing their quantitative phase image [63] (QPI). QPI delivers quantitative information of unlabeled specimens, therefore it is complementary, or in some cases superior, to established non-quantitative fluorescence microscopy. It has been shown that it is critical to observe and analyze cancer cell behavior in a 3D environment for a full understanding of the mechanisms of cancer cell invasion [18]. Therefore, there is a high demand for imaging techniques capable of capturing quantitative 3D information about the specimen.

Weakly scattering objects is a class of specimens, which are usually just single cells, satisfy 1st Born or Rytov approximation [52]. It is possible to image and reconstruct 3D refractive index (RI; n) distribution by optical diffraction tomography (ODT) where the inverse reconstruction process is a well-established procedure. ODT combines images acquired by digital holography for different sample angular positions or illumination angles to reconstruct the 3D refractive index distribution [123]. The feasibility of this method is constrained to the weak (single) scattering regime. Light passing through more complex specimen experience multiple scattering events and the regular ODT reconstruction method fails to deliver reliable quantitative 3D object representation.

Coherence-controlled holographic microscope developed in our research group utilizes temporally and spatially incoherent light source to illuminate a sample. The spatially broad source produces a wide angular range of plane waves incident on the studied specimen at the same time. Solely this property gives CCHM ability to produce a 2D QPI of a single cell in a turbid 3D medium [18, 79, 84], which is far in the multiple scattering regime. However, there is not a procedure to produce a 3D representation of a sample using CCHM, but its unique properties make it a good candidate to be a tool that could image even strongly (multiple) scattering 3D specimens.

It has been shown recently that training an artificial neural network on ODT measurements can reconstruct the refractive index of 3D phase objects [3]. The network is designed such that the voxel values of the refractive index of the 3D object are the adapted variables during the training process. The same principle can be applied to measurements from CCHM. Instead of different angular positions of the object or different illumination directions, a set of QPIs from different axial focal positions (so-

called z-stack) can be used as an input for the training part of the algorithm. There is 3D information about the specimen already encoded in the z-stack measurement. It can be converted to the refractive index distribution by properly modeling non-linear light propagation through a complex object in combination with the training process. This way a novel method that goes beyond current limits (weak scattering regime) in studied objects complexity could be developed.

9.1 Methods

The primary objective of this thesis section is to develop a method capable of reconstructing the 3D refractive index distribution of multiply scattering samples, where standard Optical Diffraction Tomography (ODT) fails to provide reliable results. The approach chosen is similar to the one presented in [3]. Hence, a computationally efficient model of light propagation suitable for CCHM is essential. Computational efficiency is crucial, as an iterative simulation of CCHM images for different refractive index distributions is necessary for acquiring the 3D reconstruction.

The approach described in [3] resembles *backpropagation*, commonly used for training neural networks. However, in essence, it involves a minimization problem that requires iterative solutions. To address these challenges, a software tool was developed as part of this thesis to simulate light propagation through 3D specimens. This software is capable of simulating CCHM and optical diffraction tomography images (quantitative phase) for multiply scattering samples. To ensure computational efficiency, light propagation models were carefully selected.

State-of-the-art methods in this field primarily rely on the Multi-Slice (MS) Beam Propagation Method (BPM) [3, 124, 125], with minor adjustments to enhance accuracy without compromising computational time. Prominent beam propagation models include split-step non-paraxial [126] and multi-layer Born [59] (MLB) methods.

In this thesis, we implemented in the software both the standard multi-slice model (BPM) and the MLB method [59]. In the these methods, the sample is approximated as a sequence of thin planar slices perpendicular to the optical axis. Each slice is modeled with an infinitesimally thin layer containing a 2D complex transmission function representing the refractive index distribution within the slice. The second part of the slice consists of a finite section of medium with a uniform refractive index, separating it from the next slice (see Fig. 9.1 for visual representation).

Light propagation through the entire specimen is simulated in a loop through all slices. At each slice, the light undergoes refraction on the infinitesimally thin 2D layer, followed by free space propagation in the uniform medium. The refraction and propagation models differ between the MS BPM and the MLB methods. The MS BPM employs a paraxial approximation for both refraction and propagation. At the same time, the MLB method also models non-paraxial scattering effects at each slice using the first Born approximation [59], which is entirely valid for such thin slices.

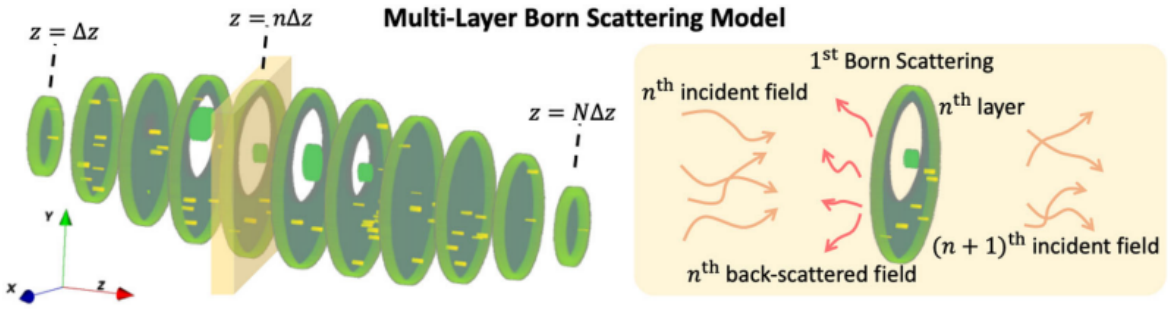

Figure 9.1: Multi-Slice model of the specimen, adapted from [59].

9.1.1 Optical diffraction tomography vs CCHM z-stack

In optical diffraction tomography, a sample is illuminated sequentially from different directions, and a hologram (complex-valued image or QPI) is acquired by off-axis holography. This can be accomplished by sequential sample rotation and acquisition or by illumination tilting followed by the acquisition. The oblique illumination is achieved utilizing galvanometers [123] (fast scanning mirrors) or by wave modulation by spatial light modulators or digital micromirror devices [85,88]. The sequence of holograms for different oblique illumination directions is then used to compute the refractive index distribution of the studied specimen [123].

In CCHM, we utilize the Köhler illumination with a spatially broad source. This gives us simultaneous illumination by oblique waves from all the directions that the ODT would use sequentially. This provides the CCHM with inherent optical sectioning capabilities, which allow the production of 3D object representations only stacking several phase images in optical axis (z-axis) direction [18]. However, this approach does not provide such good object separation in the z-direction as ODT because the information from all the oblique illuminations is multiplexed in one image. Complex deconvolution [2, 32] is a great candidate that would, in theory, at least meet the performance of ODT. The complex deconvolution in CCHM is yet to be explored, even though initial experiments and simulations were done in the course of this thesis. However, as the recent progress [3] in ODT shows, it is better to focus on non-linear computational iterative deconvolution, which is also able to capture multiple scattering effects. Therefore, we directed our efforts to iterative computational 3D refractive index distribution reconstruction. We record the so-called z-stack of QPI for different z-positions of the specimen, which is in experiments facilitated by piezo manipulators providing us nanometer-level movement precision. The QPI z-stack is then fed into the reconstruction algorithm.

9.1.2 Refractive index distribution reconstruction algorithm

The reconstruction of the refractive index distribution is basically a minimization of the difference between the measured and simulated z-stack data. The optical model of the microscope, along with the light propagation model (MS or MLB), is used to simulate the QPI z-stack from the predicted 3D RI distribution. For minimization, one can

use a range of different algorithms such as the proximal gradient method, alternative direction method of multipliers, or second-order Newton's methods [59]. For many of them, a gradient computation is needed, which can usually be found as an explicit expression defining the gradient with respect to the measured and simulated data difference. However, contemporary neural network frameworks (e.g., TensorFlow or PyTorch) provide efficient auto-gradient computations. These frameworks can be used out of the box to compute the gradients, even using GPU. Therefore, we chose to utilize TensorFlow and its implementation of ADAM optimizer [127] to minimize the difference between simulated and measured data. It is important to note that minimization alone is not enough for successful 3D RI object representation reconstruction. One has to use some apriori knowledge about the specimen and include it in the minimization procedure, e.g., in the form of sparsity or total variation regularization.

9.2 Simulations

9.2.1 Two polystyrene beads

To verify that we can revert the scattering and imaging process by the reconstruction described in Sec. 9.1.2 we simulated z-stack data by one of the algorithms MS or MLB for various model samples. The standard MS model assumes only small light-propagation angles. Therefore, it is suitable for simulations/reconstructions when objectives and illumination (condensers) have numerical apertures $\mathrm{NA_C}$ and $\mathrm{NA_O}$ up to 0.5. The higher precision of the MLB algorithm lies in its ability to capture scattering effects beyond paraxial approximation. Therefore, we used MLB, when we wanted to achieve higher accuracy with illumination and detection reaching $\mathrm{NA_C}$ and $\mathrm{NA_O}$ values close to 1. One of the model samples we used is two beads (with optical properties similar to polystyrene) situated along the optical axis of the microscope and separated by distance similar to their size. One of the simulated case is displayed in Fig. 9.2. This model is used to assess the ability to reconstruct multiply scattering specimen. The Fig. 9.2 shows the model of the sample on the left image, which is two $2\,\mu\mathrm{m}$ beads with the distance between them $4\,\mu\mathrm{m}$. Their refractive index is $n = 1.54$, while the surrounding medium is $n = 1.50$. The voxel size is $d_x = 0.3\,\mu\mathrm{m}, d_y = 0.3\,\mu\mathrm{m}, d_z = 0.3\,\mu\mathrm{m}$. The simulated phase measurements are computed with the same sampling as the modeled refractive index distribution and microscope imaging properties are defined by the wavelength $\lambda = 0.65\,\mu\mathrm{m}$ and numerical apertures of condensers and objectives, $\mathrm{NA_C} = 0.9$ and $\mathrm{NA_O} = 0.95$. The right image in Fig. 9.2 shows the result of the minimization procedure that transformed the phase measurement to the refractive index distribution. The elongation in the z-direction is caused by the so-called missing cone problem (common to all ODT techniques), which also causes under-estimation of reconstructed RI values [128, 129].

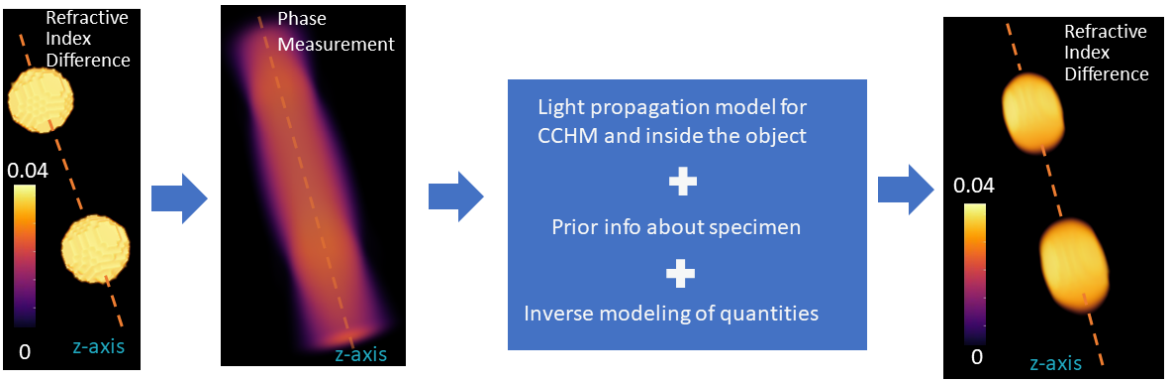

Figure 9.2: Two 2 µm beads ($n = 1.54$) with the distance between them 4 µm in medium with $n = 1.50$. Simulated data (quantitative phase images for each z-position) is created by one of the implemented beam propagation models. The simulated data is then used to invert the scattering process to obtain back the refractive index distribution.

9.2.2 Comparison of ODT and CCHM z-stack using cell model

Performance comparison of ODT and the proposed CCHM z-stack method can be done using the simulated data as well. For ODT, we simulated holographic images for various illumination directions for a single z-position of the sample. For CCHM, we simulated the images as a sum of the separate images for each illumination direction used as ODT measurement, but in addition to that, CCHM images are simulated for various object z-positions. One can deduce from the image formation (and simulation) process that the CCHM z-stack dataset should contain more information overall than the ODT dataset. In the comparison simulation experiment, we compared the performance of ODT and CCHM z-stack by imaging the complex cell model (see Fig. 9.3(a)) and reconstructing its refractive index distribution (see Fig. 9.3(b, c)). For these simulations, we chose microscope imaging properties such that the wavelength is $\lambda = 0.65$ µm, and numerical apertures of condensers and objectives are $\mathrm{NA_C} = 0.9$ and $\mathrm{NA_O} = 0.95$. Simulation grid was $64 \times 64 \times 44$ voxels large with the voxel size $d_x = 0.225$ µm, $d_y = 0.225$ µm, $d_z = 0.266$ µm. The refractive index for each cell feature was designed as depicted by arrows in Fig. 9.3(a).

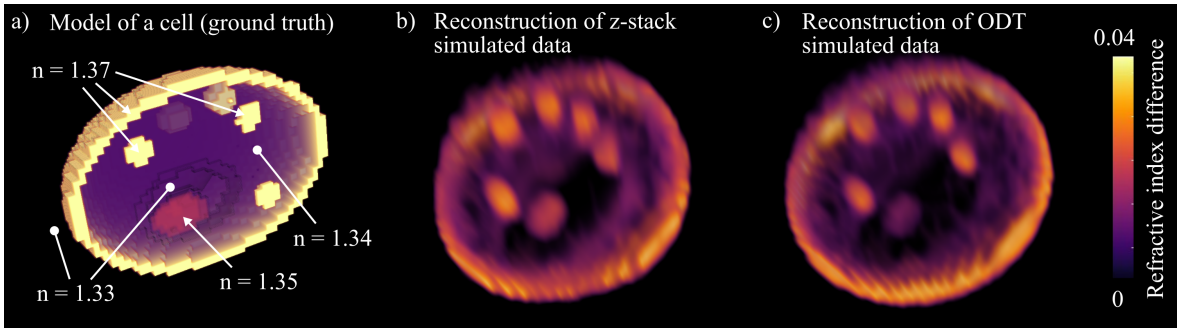

Figure 9.3: 3D cell model reconstruction from simulated data. a) The modeled refractive index distribution of the cell model. b) Reconstruction of the 3D RI distribution from CCHM z-stack data. c) Reconstruction of the 3D RI distribution from simulated optical diffraction tomography data.

Reconstruction for both methods was done with the same iterative minimization approach described in Sec. 9.1.2. We used for simulation and reconstruction the MLB method. For reliable results, we also chose the appropriate degree of sparsity regularization. As can be seen from reconstructed RI distributions in Fig. 9.3(b) and Fig. 9.3(c), the differences between the two methods are very subtle. After carefully examining the 3D representations, we concluded that the reconstruction from the CCHM z-stack provides a more accurate RI distribution in x-y directions. At the same time, ODT performs slightly better in z-direction information reconstruction. A crucial metric to consider for real-world experiments is the number of images required for reconstruction. This number is lower for the CCHM z-stack. In ODT, one has to obtain tens or hundreds of images for the reconstruction algorithm to work reliably. However, for CCHM z-stack, the number of acquisitions is 1 or 2 orders lower than for ODT, which can play a significant role when choosing the observation method of real-time 3D processes. For example, in our simulation comparison we generated 14 images for z-stack dataset and 2449 images for ODT, while the reconstruction result is very similar. We believe that making the ODT measurements more sparse would not reduce the reconstruction quality, but reducing down to 14 images would render ODT reconstruction impossible.

9.3 Experimental results

We have verified our method by capturing QPI z-stack of a red blood cell with a modified Q-Phase optical setup. We have switched condenser lenses for water dipping objectives with $\mathrm{NA_C} = 1.0$, and we used water immersion imaging objectives with $\mathrm{NA_O} = 1.2$. From the full FOV, we chose only a single red blood cell, for which we reconstructed its refractive index distribution. The input dataset to the reconstruction algorithm was $92 \times 92 \times 18$ large. The reconstructed refractive index, shown in Fig. 9.4, has the same grid size with the voxel dimensions $d_x = 0.105\,\mu\mathrm{m}, d_y = 0.105\,\mu\mathrm{m}, d_z = 0.4\,\mu\mathrm{m}$. The refractive index of the surrounding medium was $n = 1.331$. Figure 9.4(a) shows the perspective of the reconstructed 3D RI distribution, and Fig. 9.4(b) and Fig. 9.4(c) display cross-sections of the RI distribution marked by A and B, respectively.

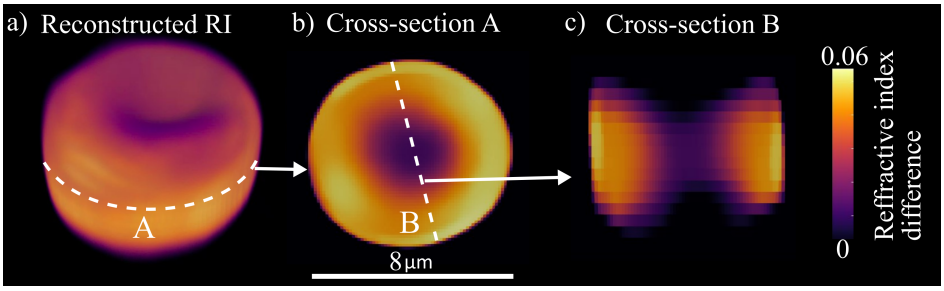

Figure 9.4: Reconstruction of the refractive index distribution from experimental z-stack data of a red blood cell. a) The perspective of the reconstructed red blood cell. b) and c) display cross-section through the red blood cell depicted by white dashed lines A and B, respectively.

The results in Fig. 9.4 can be compared to the mean refractive index values of a

healthy human red blood cell published in [130]. The study [130] found out that the mean RI value is 1.373, which complies with the values we measured (1.331-1.39).

9.4 Summary

We have proven that the developed refractive index tomography from CCHM z-stack measurements is a feasible and reliable method similar to optical diffraction tomography. We experimentally validated that the reconstruction is possible on model samples such as polystyrene beads and red blood cells and provides accurate quantitative estimates of the refractive index distribution. However, it is important to note that our comparison of ODT to CCHM z-stack shows several characteristics that favor the CCHM z-stack. Reconstruction utilizing z-stack requires 1-2 orders lower number of hologram acquisitions to achieve the same result. Based on this outcome, we see the most significant potential for the proposed method in quasi-real-time observation of 3D processes inside the cells, which is yet to be implemented in real-world applications.

Chapter 10

Summary and conclusions

The aim of the thesis was to systematically investigate the imaging possibilities provided by the CCHM technique and its coherence gating effect, especially with regard to imaging through scattering media, super-resolution, and 3D imaging. The focused work on the partial objectives outlined in Chapter 3 helped approach the broad focus of this thesis systematically, which resulted in several pioneering papers regarding the use of coherence-gating in digital holography. It can be concluded that the aims and goals of the thesis were successfully achieved as the possibilities of the CCHM and its coherence-gating effects were thoroughly investigated. Moreover, the investigations led to the development of novel imaging techniques, which we have successfully applied to practical biomedical applications.

This thesis began with an introduction to the optical coherence theory and a description of the cross-correlation properties of light. The approach to describing classical interference experiments and interferometric setups in terms of optical coherence provided the often missing link between the idealized coherent description of light and the theory of partial coherence. The theory, together with an overview of the existing partially coherent interferometric imaging techniques showed the state of art exploitation of the coherence-gating effect, which is an extraordinary property of partially coherent interferometric systems.

The major part of the thesis concerning the description of the coherence-controlled holographic microscope using the optical coherence theory in combination with appropriate light propagation models showed the interconnection between complete mutual coherence function measurement and holographic recording under controlled coherence gate manipulation. Expressions describing the mutual coherence function of the object-scattered and reference field measurement were derived, and we showed that complex image acquisition for different coherence gate positions obtains the same form. Including the multi-slice light propagation model proved to be an excellent way of multiple scattering description. We provided a theoretical description proving that complete mutual coherence function measurement contains beneficial information for 3D imaging, imaging through turbid media, and imaging with sub-diffraction limited resolution. The extraction of information from a complete mutual coherence function was demonstrated in numerous experiments, and this thesis significantly expands the potential of partially coherent holographic microscopes in several different areas (3D imaging, imaging through turbid media, and super-resolution QPI).

Imaging through turbid media was first demonstrated either theoretically and ex-

perimentally on a two-layer object. One layer is a planar object of interest and the other layer being a random strongly scattering layer. Reconstruction of the object image from mutual coherence function measurement was achieved with excellent quality. The same approach to reconstruction was used to synthesize an image when imaging through two scattering layers and through volumetric diffuser - a slab of chicken breast (0.8 mm thick). We achieved high-quality synthetic QPI even when imaging through such a thick scattering layer of tissue.

The multiply scattered light was also used to enhance the resolving power of CCHM. First, the feasibility of imaging by multiply scattered light through diffraction gratings was demonstrated, which we used to adapt an approach from structured illumination microscopy to produce an image with a superior lateral resolution in comparison to the ballistic light image. In the thesis, we introduced a method for generating synthetic aperture quantitative phase images in holographic microscopes with partially coherent illumination. The proposed solution overcomes the diffraction limit and is remarkably simple to implement, as it does not require any modifications to the CCHM optical system. The technique relies on oblique illumination supplied by diffraction on a phase grating positioned near the specimen, coupled with the intrinsic coherence-gating properties of the partially coherent light. The process involves sequentially coherence-gating the light scattered into each diffraction order of the phase grating. Using the acquired images, we synthesize quantitative phase images with significantly enhanced spatial frequency bandwidth. The paper attached in the thesis thoroughly explores the theoretical aspects of the coherence-gated imaging process and provides a detailed methodology for the measurement. Notably, our study represents the first application of coherence gating for purposes other than imaging through or in turbid media. The proposed method is envisioned to offer an easily implementable super-resolution QPI, especially beneficial for high-throughput biomedical applications. By obtaining large field-of-view datasets with moderate-to-high spatial resolution and excellent quantitative information quality, this approach can have a significant impact on fields such as stem cell research and the development of migrastatics. Moreover, this work addresses the pressing need for extensive, high-quality datasets essential for accelerating automated analysis using artificial intelligence techniques.

Additionally to the synthetic aperture approach, we present a method for achieving single-shot label-free super-resolution quantitative phase imaging (QPI). This approach is also very straightforward to implement without requiring modifications to the microscope's optical system. We generate a sub-diffraction limited coherence-gating function by introducing phase or amplitude modulation to the planes conjugated with the light source, such as the front focal plane of the condenser. Through theoretical analysis, numerical simulations, and experiments, we demonstrate the first-ever superoscillatory CGF shaped by phase and amplitude modulation. For experimental validation, we use an amplitude mask for modulation, as it proves to be more robust to optical aberrations than phase masks. Our experimental results show almost 20% improvement in resolving power for phase imaging of model specimens and complex objects like cancer cells. The potential spatial resolution improvement is not limited in principle, and we anticipate achieving over 20% resolution gain with more sophisticated modulation techniques. For

instance, incorporating a spatial light modulator into the optical setup would enable simultaneous compensation of pupil aberrations and the modulation required to create the superoscillatory CGF. We believe that our method offers an easily implementable super-resolution QPI, particularly well-suited for high-throughput biomedical applications. Expanding the CGF shaping theory beyond the scalar approximation will enable unprecedented spatial resolution for QPI. This capability can significantly impact cancer research, as it allows observation of previously unseen intracellular processes in real-time with spatial super-resolution and high-quality quantitative information.

It is important to emphasize the difference between our QPI super-resolution and standard fluorescent techniques. Our both methods are wide-field methods in contrast to (in the majority) scanning fluorescent methods. This gives our techniques an advantage in terms of acquisition speed. The synthetic aperture method is quasi-real time, and the method utilizing superoscillatory CGF is a single-shot (real-time) technique. Therefore, we can achieve imaging throughputs unseen in fluorescent imaging. Moreover, we build on top of digital holography providing QPI, a quantitative, non-invasive, and label-free imaging technique.

As part of the thesis, we have developed software for 3D refractive index reconstruction from CCHM z-stack measurements. This software can simulate QPI produced by coherent or partially coherent systems such as CCHM or oblique illumination images for optical diffraction tomography. The reconstruction software was verified on simulated data. Experimental validation was performed on model samples such as polystyrene beads and red blood cells. We have proven that reconstruction from the CCHM z-stack dataset it is possible to obtain similar results to optical diffraction tomography. However, CCHM requires 1-2 orders lower number of acquisitions to achieve the same result. We see the most significant potential for the proposed method in quasi-real-time observation of 3D processes inside the cells.

List of Abbreviations

2D ..... Two dimensional

3D ..... Three dimensional

BPM ..... Beam propagation method

CCHM ..... Coherence-controlled holographic microscope

CGF ..... Coherence-gating function

FOV ..... Field of view

FPM ..... Fourier ptychografic microscopy

GPU ..... Graphics processing unit

FWHM ..... Full width at half maximum

MCF ..... Mutual coherence function

MLB ..... Multi-layer Born

MS ..... Multi-slice

PSF ..... Point spread function

ODT ..... Optical diffraction tomography

QPI ..... Quantitative phase image/imaging

SBP ..... Space bandwidth product

SIM ..... Structured illumination microscopy

NA ..... Numerical aperture

Author's publications and outputs

ŠURÁŇOVÁ, M.; **ĎURIŠ, M.**; NETÍKOVÁ, I. Š.; BRÁVEK, J; HORÁK, T.; JUZOVÁ, V.; CHMELÍK, R.; VESELÝ, P. Primary assessment of medicines for expected migrastatic potential with holographic incoherent quantitative phase imaging Biomedical Optics Express 2023; 14, 2689-2708

ĎURIŠ, M.; BOUCHAL, P.; CHMELÍK, R. Single-shot super-resolution quantitative phase imaging allowed by coherence gate shaping. APL Photonics 1 April 2023; 8 (4): 046103.

ĎURIŠ, M. Phase in Brno 2022, Super-resolution in quantitative phase imaging (Invited lecture)

ĎURIŠ, M.; BOUCHAL, P.; ROVENSKÁ, K.; CHMELÍK, R. Coherence-encoded synthetic aperture for super-resolution quantitative phase imaging. APL Photonics 1 April 2022; 7 (4): 046105.

ĎURIŠ, M.; CHMELÍK, R. Super-Resolution in coherence-controlled holographic microscope using synthetic aperture approach. OSA Optical Sensors and Sensing Congress 2021, OSA Technical Digest (Optica Publishing Group, 2021), ISBN: 978-1-943580-90-3. (Summary and poster)

ĎURIŠ, M.; CHMELÍK, R. Coherence gate manipulation for enhanced imaging through scattering media by non-ballistic light in partially coherent interferometric systems. Optics Letters 2021; 46, 4486-4489

ĎURIŠ, M.; CHMELÍK, R. Quantitative phase image enhancement by smart coherence gate manipulation in partially coherent holographic microscope. Cz-BI Scientific Conference – Imaging Principles of Life 2020. (Talk)

ĎURIŠ, M.; CHMELÍK, R. Robust Method for Quantitative Phase Image Synthesis out of Coherence-gated Multiply Scattered Light. 19th international ELMI meeting, 4-7 June 2019, Brno, Czech Republic. (Summary, Invited Flash talk, and poster)

ĎURIŠ, M.; CHMELÍK, R. Robust Method for Quantitative Phase Image Synthesis out of Coherence-gated Multiply Scattered Light. Digital Holography and Three-Dimensional Imaging 2019. OSA Technical Digest (Optical Society of America, 2019), 2019. ISBN: 978-1-943580-59-0. (Summary and poster)

DORAZILOVÁ, J.; ŠTRBKOVÁ, l.; **ĎURIŠ, M.**; VOJTOVÁ, L. Biopolymeric scaffold for cell visualisation in 3D environment using Coherence-controlled holographic microscopy. 28th Biomaterials in Medicine and Veterinary Medicine, Annual Conference. Engineering of Biomaterials - Inżynieria Biomateriałów. Kraków: Scientific Publishing House AKAPIT, 2019. s. 43-43. ISSN: 1429-7248.

ĎURIŠ, M. awarded the Brno Phd Talent Award in 2018

CHMELÍK, R.; **ĎURIŠ, M.**; ŠTRBKOVÁ, L. Quantitative phase imaging in turbid media by coherence controlled holographic microscopy. In Unconventional Optical Imaging. Proceedings of SPIE. Strasbourg, France: Society of Photo-Optical Instrumentation Engineers (SPIE), 2018. s. 1-12. ISSN: 0277-786X.

ĎURIŠ, M.; BRADU, A.; PODOLEANU, A.; Hughes, M. Towards an ultra-thin medical endoscope: multimode fibre as a wide-field image transferring medium. In Proceedings of SPIE. Proceedings of SPIE. 10591. SPIE, 2018. s. 1-7. ISBN: 978-1-5106-1675-2. ISSN: 0277-786X.

Bibliography

[1] KIM, M. K.: *Digital Holographic Microscopy*. New York, NY: Springer New York, 2011, ISBN 978-1-4419-7793-9, pp. 149–190.

[2] COTTE, Y. et al.: Realistic 3D coherent transfer function inverse filtering of complex fields. *Biomedical Optics Express*, vol. 2, no. 8, 2011: p. 2216, ISSN 2156-7085.

[3] KAMILOV, U. S. et al.: Learning approach to optical tomography. *Optica*, vol. 2, no. 6, 2015: p. 517, ISSN 2334-2536, <1502.01914>.

[4] YOON, S. et al.: Deep optical imaging within complex scattering media. *Nature Reviews Physics*, vol. 2, no. 3, 2020: pp. 141–158, ISSN 25225820.

[5] LEITH, E. N. UPATNIEKS, J.: Holography with Achromatic-Fringe Systems. *Journal of the Optical Society of America*, vol. 57, no. 8, 1967: p. 975, ISSN 0030-3941.

[6] KOLMAN, P. CHMELÍK, R.: Coherence-controlled holographic microscope. *Optics Express*, vol. 18, no. 21, 2010: pp. 21990–22003, ISSN 1094-4087.

[7] SLABÝ, T. et al.: Off-axis setup taking full advantage of incoherent illumination in coherence-controlled holographic microscope. *Optics Express*, vol. 21, no. 12, 2013: pp. 14747–62, ISSN 1094-4087.

[8] AVANAKI, M. R. N. PODOLEANU, A.: En-face time-domain optical coherence tomography with dynamic focus for high-resolution imaging . *Journal of Biomedical Optics*, vol. 22, no. 5, 2017: p. 056009, ISSN 1083-3668.

[9] LEITGEB, R. A.: En face optical coherence tomography: a technology review [Invited]. *Biomedical Optics Express*, vol. 10, no. 5, 2019: p. 2177, ISSN 2156-7085.

[10] SALHOV, O., WEINBERG, G. KATZ, O.: Depth-resolved speckle-correlations imaging through scattering layers via coherence gating. *Optics Letters*, vol. 43, no. 22, 2018: p. 5528, ISSN 0146-9592.

[11] LOŠŤ'ÁK, M. et al.: Coherence-controlled holographic microscopy in diffuse media. *Optics Express*, vol. 22, no. 4, 2014: p. 4180, ISSN 1094-4087.

[12] CHMELIK, R. et al.: The Role of Coherence in Image Formation in Holographic Microscopy. *Progress in Optics*, vol. 59, 2014: pp. 267–335, ISSN 0079-6638.

[13] KOLLAROVA, V. et al.: Quantitative phase imaging through scattering media by means of coherence-controlled holographic microscope. *Journal of Biomedical Optics*, vol. 20, no. 11, 2015: p. 111206, ISSN 1083-3668.

[14] CHMELÍK, R., DURIS, M. ŠTRBKOVÁ, L.: Quantitative phase imaging in turbid media by coherence controlled holographic microscopy. *Proc.SPIE*, vol. 10677, 2018: pp. 10677 – 10677 – 11.

[15] KIM, T. et al.: White-light diffraction tomography of unlabelled live cells. *Nature Photonics*, vol. 8, no. 3, 2014: pp. 256–263, ISSN 17494885.

[16] COLLAKOVA, J. et al.: Coherence-controlled holographic microscopy enabled recognition of necrosis as the mechanism of cancer cells death after exposure to cytopathic turbid emulsion. *Journal of Biomedical Optics*, vol. 20, no. 11, 2015: p. 111213, ISSN 1083-3668.

[17] GÁL, B. et al.: Distinctive behaviour of live biopsy-derived carcinoma cells unveiled using coherence-controlled holographic microscopy. *PLOS ONE*, vol. 12, no. 8, aug 2017: p. e0183399, ISSN 1932-6203.

[18] TOLDE, O. et al.: Quantitative phase imaging unravels new insight into dynamics of mesenchymal and amoeboid cancer cell invasion. *Scientific Reports 2018 8:1*, vol. 8, no. 1, aug 2018: p. 12020, ISSN 2045-2322.

[19] MEHTA, S. B. SHEPPARD, C. J. R.: Partially coherent microscope in phase space. *Journal of the Optical Society of America A*, vol. 35, no. 8, 2018: p. 1272, ISSN 1084-7529.

[20] DOGARIU, A. POPESCU, G.: Measuring the Phase of Spatially Coherent Polychromatic Fields. *Physical Review Letters*, vol. 89, no. 24, nov 2002: p. 243902, ISSN 0031-9007.

[21] TÝČ, M. et al.: Numerical refocusing in digital holographic microscopy with extended-sources illumination. *Opt. Express*, vol. 21, no. 23, nov 2013: pp. 28258–28271.

[22] NÄRHI, M. et al.: Experimental Measurement of the Second-Order Coherence of Supercontinuum. *Physical Review Letters*, vol. 116, no. 24, 2016: p. 243901, ISSN 10797114.

[23] SHAO, Y. et al.: Spatial coherence measurement and partially coherent diffractive imaging using self-referencing holography. *Optics Express*, vol. 26, no. 4, 2018: p. 4479, ISSN 1094-4087.

[24] WOLF, E.: Solution of the phase problem in the theory of structure determination of crystals from X-ray diffraction experiments. *Physical Review Letters*, vol. 103, no. 7, 2009: p. 075501, ISSN 00319007.

[25] CLASSEN, A. et al.: Incoherent Diffractive Imaging via Intensity Correlations of Hard X Rays. *Physical Review Letters*, vol. 119, no. 5, 2017: p. 053401, ISSN 10797114, <1705.08677>.

[26] MARKS, D. L. et al.: Visible Cone-Beam Tomography Camera. *Science*, vol. 284, no. June, 1999: pp. 2164–2166.

[27] PARK, Y., DEPEURSINGE, C. POPESCU, G.: Quantitative phase imaging in biomedicine. *Nature Photonics*, vol. 12, no. 10, 2018: pp. 578–589, ISSN 1749-4893.

[28] NEWMAN, J. A., LUO, Q. WEBB, K. J.: Imaging Hidden Objects with Spatial Speckle Intensity Correlations over Object Position. *Physical Review Letters*, vol. 116, no. 7, 2016: p. 073902, ISSN 10797114.

[29] BATARSEH, M. et al.: Passive sensing around the corner using spatial coherence. *Nature Communications*, vol. 9, no. 1, 2018: pp. 1–6, ISSN 20411723.

[30] IZATT, J. A. et al.: Optical coherence microscopy in scattering media. *Optics Letters*, vol. 19, no. 8, 1994: p. 590, ISSN 0146-9592.

[31] ZICHA, D. DUNN, G. A.: An image processing system for cell behaviour studies in subconfluent cultures. *Journal of Microscopy*, vol. 179, no. 1, jul 1995: pp. 11–21, ISSN 00222720.

[32] COTTE, Y. et al.: Marker-free phase nanoscopy. *Nature Photonics*, vol. 7, no. 2, 2013: pp. 113–117.

[33] CHOI, Y. et al.: Optical imaging with the use of a scattering lens. *IEEE Journal on Selected Topics in Quantum Electronics*, vol. 20, no. 2, 2014: pp. 61–73, ISSN 1077260X.

[34] CHOI, Y. et al.: Overcoming the diffraction limit using multiple light scattering in a highly disordered medium. *Physical Review Letters*, vol. 107, no. 2, 2011: p. 023902, ISSN 00319007.

[35] MANDEL, L. WOLF, E.: *Optical Coherence and Quantum Optics*. Cambridge University Press, 1995, ISBN 9780521417112.

[36] WOLF, E. BORN, M.: A macroscopic theory of interference and diffraction of light from finite sources II. Fields with a spectral range of arbitrary width. *Proceedings of the Royal Society of London. Series A. Mathematical and Physical Sciences*, vol. 230, no. 1181, 1955: pp. 246–265.

[37] THOMPSON, B. J. WOLF, E.: Two-Beam Interference with Partially Coherent Light. *J. Opt. Soc. Am.*, vol. 47, no. 10, 1957: pp. 895–902.

[38] GABOR, D. GOSS, W. P.: Interference Microscope with Total Wavefront Reconstruction. *J. Opt. Soc. Am.*, vol. 56, no. 7, 1966: pp. 849–856, ISSN 0030-3941.

[39] BASTIAANS, M. J.: Application of the Wigner distribution function to partially coherent light. *J. Opt. Soc. Am. A*, vol. 3, no. 8, aug 1986: pp. 1227–1238.

[40] GUIGAY, J.-P.: The ambiguity function in diffraction and isoplanatic imaging by partially coherent beams. *Optics Communications*, vol. 26, no. 2, 1978: pp. 136–138, ISSN 0030-4018.

[41] BRENNER, K.-H. OJEDA-CASTAÑEDA, J.: Ambiguity Function and Wigner Distribution Function Applied to Partially Coherent Imagery. *Optica Acta: International Journal of Optics*, vol. 31, no. 2, 1984: pp. 213–223.

[42] MEHTA, S. B. SHEPPARD, C. J.: Using the phase-space imager to analyze partially coherent imaging systems: Bright-field, phase contrast, differential interference contrast, differential phase contrast, and spiral phase contrast. *Journal of Modern Optics*, vol. 57, no. 9, 2010: pp. 718–739, ISSN 09500340.

[43] MEHTA, S. B. SHEPPARD, C. J. R.: Equivalent of the point spread function for partially coherent imaging. *Optica*, vol. 2, no. 8, 2015: p. 736, ISSN 2334-2536.

[44] NAIK, D. N. et al.: Coherence holography by achromatic 3-D field correlation of generic thermal light with an imaging Sagnac shearing interferometer. *Optics Express*, vol. 20, no. 18, 2012: p. 19658, ISSN 1094-4087.

[45] LU, X. et al.: Noniterative spatially partially coherent diffractive imaging using pinhole array mask. *Advanced Photonics*, vol. 1, no. 01, jan 2019: p. 1, ISSN 2577-5421.

[46] WAX, A. THOMAS, J. E.: Optical heterodyne imaging and Wigner phase space distributions. *Optics Letters*, vol. 21, no. 18, 1996: p. 1427, ISSN 0146-9592.

[47] WALLER, L., SITU, G. FLEISCHER, J. W.: Phase-space measurement and coherence synthesis of optical beams. *Nature Photonics*, vol. 6, no. 7, 2012: pp. 474–479, ISSN 17494885.

[48] MORRILL, D., LI, D. PACIFICI, D.: Measuring subwavelength spatial coherence with plasmonic interferometry. *Nature Photonics*, vol. 10, no. 10, 2016: pp. 681–687, ISSN 17494893.

[49] CLASSEN, A. et al.: Superresolving Imaging of Arbitrary One-Dimensional Arrays of Thermal Light Sources Using Multiphoton Interference. *Physical Review Letters*, vol. 117, no. 25, 2016: p. 253601, ISSN 10797114.

[50] KANG, S. et al.: Imaging deep within a scattering medium using collective accumulation of single-scattered waves. *Nature Photonics*, vol. 9, no. 4, apr 2015: pp. 253–258, ISSN 1749-4885.

[51] KREIS, T.: Digital holographic interference-phase measurement using the Fourier-transform method. *Journal of the Optical Society of America A*, vol. 3, no. 6, 1986: p. 847, ISSN 1084-7529.

[52] BORN, M. WOLF, E.: *Principles of optics : electromagnetic theory of propagation, interference and diffraction of light*. Cambridge University Press, 1999, ISBN 9781139644181.

[53] CHMELÍK, R. HARNA, Z.: Parallel-mode confocal microscope. *Optical Engineering*, vol. 38, no. 10, 1999: pp. 1635–1639.

[54] BALVAN, J. et al.: Multimodal holographic microscopy: Distinction between apoptosis and oncosis. *PLoS ONE*, vol. 10, no. 3, 2015: pp. 1–16, ISSN 19326203.

[55] BABOCKÝ, J. et al.: Quantitative 3D Phase Imaging of Plasmonic Metasurfaces. *ACS Photonics*, vol. 4, no. 6, jun 2017: pp. 1389–1397.

[56] STRBKOVA, L. et al.: Automated classification of cell morphology by coherence-controlled holographic microscopy. *Journal of Biomedical Optics*, vol. 22, no. 8, aug 2017: pp. 1–9.

[57] WOLF, E.: Electromagnetic Diffraction in Optical Systems. I. An Integral Representation of the Image Field. *Proceedings of the Royal Society A: Mathematical, Physical and Engineering Sciences*, vol. 253, no. 1274, 1959: pp. 349–357, ISSN 1364-5021.

[58] WOLF, E.: Three-dimensional structure determination of semi-transparent objects from holographic data. *Optics Communications*, vol. 1, no. 4, 1969: pp. 153–156, ISSN 0030-4018.

[59] CHEN, M. et al.: Multi-layer Born multiple-scattering model for 3D phase microscopy. *Optica*, vol. 7, no. 5, 2020: p. 394.

[60] ZERNIKE, F.: How I discovered phase contrast. *Science (New York, N.Y.)*, vol. 121, no. 3141, 1955: pp. 345–9, ISSN 0036-8075.

[61] ĎURIŠ, M.: *Imaging of an object in turbid medium by combining the signal of ballistic and diffuse photons in the coherence-controlled holographic microscope*. Doctoral Thesis, 2018.

[62] BARER, R.: Interference Microscopy and Mass Determination. *Nature*, vol. 169, no. 4296, 1952: pp. 366–367, ISSN 0028-0836.

[63] ZANGLE, T. A. TEITELL, M. A.: Live-cell mass profiling: An emerging approach in quantitative biophysics. *Nature Methods*, vol. 11, no. 12, 2014: pp. 1221–1228, ISSN 15487105, <NIHMS150003>.

[64] KASTL, L. et al.: Quantitative phase imaging for cell culture quality control. *Cytometry Part A*, vol. 91, no. 5, 2017: pp. 470–481, ISSN 15524930.

[65] HORN, W.: Interference microscope with transmitted illumination. 1956. URL <https://patents.google.com/patent/US2950649>

[66] DILWORTH, D. S., LEITH, E. N. LOPEZ, J. L.: Imaging absorbing structures within thick diffusing media. *Applied optics*, vol. 29, no. 5, 1990: pp. 691–698.

[67] KEMPE, M., RUDOLPH, W. WELSCH, E.: Comparative study of confocal and heterodyne microscopy for imaging through scattering media. *Journal of the Optical Society of America A*, vol. 13, no. 1, 1996: p. 46, ISSN 1084-7529.

[68] KEMPE, M. et al.: Ballistic and diffuse light detection in confocal and heterodyne imaging systems. *J. Opt. Soc. Am. A*, vol. 14, no. 1, 1997: pp. 216–223, ISSN 1084-7529.

[69] WANG, L. M., HO, P. P. ALFANO, R. R.: Double-stage picosecond Kerr gate for ballistic time-gated optical imaging in turbid media. *Applied optics*, vol. 32, no. 4, 1993: pp. 535–540, ISSN 0003-6935.

[70] HEBDEN, J. C. KRUGER, R. A.: Transillumination imaging performance: A time-of-flight imaging system. *Medical Physics*, vol. 17, no. 3, 1990: pp. 351–356.

[71] CAULFIELD, H. J.: Holographic Imaging Through Scatterers. vol. 58, 1968: pp. 276–277, ISSN 0030-3941.

[72] LEITH, E. N. KUEI, C. P.: Interferometric method for imaging through inhomogeneities. *Optics letters*, vol. 12, no. 3, 1987: pp. 149–51, ISSN 0146-9592.

[73] LEITH, E. N. et al.: Imaging through scattering media using spatial incoherence techniques. *Optics Letters*, vol. 16, no. 23, 1991: p. 1820, ISSN 0146-9592.

[74] LEITH, E. et al.: Imaging through scattering media with holography. *Journal of the Optical Society of America A*, vol. 9, no. 7, 1992: pp. 1148–1153, ISSN 1084-7529.

[75] DURDURAN, T. et al.: Diffuse Optics for Tissue Monitoring and Tomography. *Reports on progress in physics. Physical Society (Great Britain)*, vol. 73, no. 7, 2010, ISSN 1361-6633.

[76] VAN ROSSUM, M. C. W. NIEUWENHUIZEN, T. M.: Multiple scattering of classical waves: microscopy, mesoscopy, and diffusion. *Reviews of Modern Physics*, vol. 71, no. 1, 1999: pp. 313–371, ISSN 0034-6861.

[77] POPPOF, S. et al.: Controlling Light Through Optical Disordered Media : Transmission Matrix Approach. *New Journal of Physics*, vol. 13, no. 12, 2011: p. 123021.

[78] YAQOOB, Z. et al.: Optical phase conjugation for turbidity suppression in biological samples. *Nature Photonics*, vol. 2, no. 2, 2008: pp. 110–115, ISSN 17494885.

[79] ĎURIŠ, M. et al.: Towards an ultra-thin medical endoscope: multimode fibre as a wide-field image transferring medium. In *2nd Canterbury Conference on OCT with Emphasis on Broadband Optical Sources*, vol. 10591, ed. by O. Bang; A. Podoleanu, SPIE, 2018, ISBN 9781510616745, p. 34.

[80] EDREI, E. SCARCELLI, G.: Memory-effect based deconvolution microscopy for super-resolution imaging through scattering media. *Scientific Reports*, vol. 6, no. April, 2016: pp. 1–8, ISSN 20452322.

[81] FREUND, I., ROSENBLUH, M. FENG, S.: Memory effects in propagation of optical waves through disordered media. *Physical Review Letters*, vol. 61, no. 20, 1988: pp. 2328–2331, ISSN 00319007.

[82] GOODMAN, J. W.: *Statistical Optics*. Wiley, second edi edition, 2015, ISBN 978-1-119-00945-0.

[83] SHVARTSMAN, N. FREUND, I.: Speckle spots ride phase saddles sidesaddle. *Optics Communications*, vol. 117, no. 3-4, 1995: pp. 228–234, ISSN 00304018.

[84] ĎURIŠ, M. CHMELÍK, R.: Coherence gate manipulation for enhanced imaging through scattering media by non-ballistic light in partially coherent interferometric systems. *Opt. Lett.*, vol. 46, no. 18, sep 2021: pp. 4486–4489.

[85] KIM, K. et al.: Optical diffraction tomography techniques for the study of cell pathophysiology. *Journal of Biomedical Photonics & Engineering*, 2016: pp. 020201–1–020201–16, ISSN 2411-2844.

[86] ENGELHARDT, K. HÄUSLER, G.: Acquisition of 3-D data by focus sensing. *Applied Optics*, vol. 27, no. 22, nov 1988: p. 4684, ISSN 0003-6935.

[87] NEIL, M. A. A., JUŠKAITIS, R. WILSON, T.: Method of obtaining optical sectioning by using structured light in a conventional microscope. *Optics Letters*, vol. 22, no. 24, dec 1997: p. 1905, ISSN 0146-9592.

[88] LEE, K. et al.: Time-multiplexed structured illumination using a DMD for optical diffraction tomography. *Optics Letters*, vol. 42, no. 5, 2017: p. 999, ISSN 0146-9592, `<1612.00044>`.

[89] HEINTZMANN, R. HUSER, T.: Super-Resolution Structured Illumination Microscopy. *Chemical Reviews*, vol. 117, no. 23, dec 2017: pp. 13890–13908, ISSN 0009-2665.

[90] MICÓ, V. et al.: Superresolution digital holographic microscopy for three-dimensional samples. *Opt. Express*, vol. 16, no. 23, nov 2008: pp. 19260–19270.

[91] MICO, V. et al.: Transverse resolution improvement using rotating-grating time-multiplexing approach. *Journal of the Optical Society of America A*, vol. 25, no. 5, 2008: pp. 1115–1129.

[92] GUTZLER, T. et al.: Coherent aperture-synthesis, wide-field, high-resolution holographic microscopy of biological tissue. *Optics Letters*, vol. 35, no. 8, 2010: p. 1136, ISSN 0146-9592.

[93] PATURZO, M. et al.: Super-resolution in digital holography by a two-dimensional dynamic phase grating. *Optics Express*, vol. 16, no. 21, 2008: p. 17107, ISSN 1094-4087.

[94] CHOWDHURY, S. et al.: Structured illumination multimodal 3D-resolved quantitative phase and fluorescence sub-diffraction microscopy. *Biomed. Opt. Express*, vol. 8, no. 5, 2017: pp. 2496–2518.

[95] WICKER, K. HEINTZMANN, R.: Resolving a misconception about structured illumination. *Nature Photonics*, vol. 8, no. 5, 2014: pp. 342–344, ISSN 1749-4893.

[96] PARK, Y. et al.: Speckle-field digital holographic microscopy. *Opt. Express*, vol. 17, no. 15, 2009: pp. 12285–12292.

[97] BAEK, Y., LEE, K. PARK, Y.: High-Resolution Holographic Microscopy Exploiting Speckle-Correlation Scattering Matrix. *Physical Review Applied*, vol. 10, no. 2, 2018: p. 1, ISSN 23317019.

[98] BISHARA, W. et al.: Lensfree on-chip microscopy over a wide field-of-view using pixel super-resolution. *Opt. Express*, vol. 18, no. 11, 2010: pp. 11181–11191.

[99] XU, W. et al.: Digital in-line holography for biological applications. *Proceedings of the National Academy of Sciences*, vol. 98, no. 20, sep 2001: pp. 11301 LP – 11305.

[100] GARCIA-SUCERQUIA, J. et al.: Digital in-line holographic microscopy. *Applied Optics*, vol. 45, no. 5, 2006: pp. 836–850.

[101] MICÓ, V. ZALEVSKY, Z.: Superresolved digital in-line holographic microscopy for high-resolution lensless biological imaging. *Journal of Biomedical Optics*, vol. 15, no. 4, jul 2010: pp. 1–5.

[102] GRANERO, L. et al.: Single-exposure super-resolved interferometric microscopy by RGB multiplexing in lensless configuration. *Optics and Lasers in Engineering*, vol. 82, 2016: pp. 104–112, ISSN 0143-8166.

[103] ZHENG, G., HORSTMEYER, R. YANG, C.: Wide-field, high-resolution Fourier ptychographic microscopy. *Nature Photonics*, vol. 7, no. 9, 2013: pp. 739–745, ISSN 1749-4893.

[104] TIAN, L. et al.: Computational illumination for high-speed in vitro Fourier ptychographic microscopy. *Optica*, vol. 2, no. 10, oct 2015: p. 904, ISSN 2334-2536.

[105] FIENUP, J. R.: Reconstruction of a complex-valued object from the modulus of its Fourier transform using a support constraint. *Journal of the Optical Society of America A*, vol. 4, no. 1, 1987: pp. 118–123.

[106] SHEPPARD, C. J.: Fundamentals of superresolution. *Micron*, vol. 38, no. 2, 2007: pp. 165–169, ISSN 09684328.

[107] YUAN, C., ZHAI, H. LIU, H.: Angular multiplexing in pulsed digital holography for aperture synthesis. *Optics Letters*, vol. 33, no. 20, 2008: pp. 2356–2358.

[108] MIRSKY, S. K. SHAKED, N. T.: First experimental realization of six-pack holography and its application to dynamic synthetic aperture superresolution. *Optics Express*, vol. 27, no. 19, 2019: pp. 26708–26720.

[109] SHAKED, N. T. et al.: Off-axis digital holographic multiplexing for rapid wavefront acquisition and processing. *Advances in Optics and Photonics*, vol. 12, no. 3, 2020: pp. 556–611.

[110] DARDIKMAN, G. SHAKED, N. T.: Is multiplexed off-axis holography for quantitative phase imaging more spatial bandwidth-efficient than on-axis holography? [Invited]. *Journal of the Optical Society of America A*, vol. 36, no. 2, 2019: pp. A1–A11.

[111] HEINTZMANN, R. CREMER, C. G.: Laterally modulated excitation microscopy: Improvement of resolution by using a diffraction grating. *Optical Biopsies and Microscopic Techniques III*, vol. 3568, no. February 2015, 1999: pp. 185–196.

[112] LANG, P. et al.: Cellular imaging in drug discovery. *Nature Reviews Drug Discovery*, vol. 5, no. 4, 2006: pp. 343–356, ISSN 1474-1784.

[113] COSTA, M. R. et al.: Continuous live imaging of adult neural stem cell division and lineage progression in vitro. *Development*, vol. 138, no. 6, mar 2011: pp. 1057–1068, ISSN 0950-1991.

[114] LOHMANN, A. W. et al.: Space–bandwidth product of optical signals and systems. *Journal of the Optical Society of America A*, vol. 13, no. 3, 1996: p. 470, ISSN 1084-7529.

[115] HUANG, F. M. ZHELUDEV, N. I.: Super-Resolution without Evanescent Waves. *Nano Letters*, vol. 9, no. 3, mar 2009: pp. 1249–1254, ISSN 1530-6984.

[116] GBUR, G.: Using superoscillations for superresolved imaging and subwavelength focusing. *Nanophotonics*, vol. 8, no. 2, 2018: pp. 205–225, ISSN 21928614.

[117] ROGERS, E. T. F. et al.: A super-oscillatory lens optical microscope for subwavelength imaging. *Nature Materials*, vol. 11, no. 5, 2012: pp. 432–435, ISSN 1476-4660.

[118] ROGERS, E. T. F. et al.: Far-field unlabeled super-resolution imaging with superoscillatory illumination. *APL Photonics*, vol. 5, no. 6, jun 2020: p. 66107.

[119] DI FRANCIA, G. T.: Super-gain antennas and optical resolving power. *Il Nuovo Cimento (1943-1954)*, vol. 9, no. 3, 1952: pp. 426–438, ISSN 1827-6121.

[120] REZA, N. HAZRA, L.: Toraldo filters with concentric unequal annuli of fixed phase by evolutionary programming. *J. Opt. Soc. Am. A*, vol. 30, no. 2, feb 2013: pp. 189–195.

[121] HUANG, K. et al.: Optimization-free superoscillatory lens using phase and amplitude masks. *Laser & Photonics Reviews*, vol. 8, no. 1, jan 2014: pp. 152–157, ISSN 1863-8880.

[122] ROGERS, K. S. et al.: Optimising superoscillatory spots for far-field super-resolution imaging. *Opt. Express*, vol. 26, no. 7, apr 2018: pp. 8095–8112.

[123] SUNG, Y. et al.: Optical diffraction tomography for high resolution live cell imaging. *Optics InfoBase Conference Papers*, vol. 17, no. 1, 2009: pp. 1977–1979, ISSN 21622701.

[124] TIAN, L. WALLER, L.: 3D intensity and phase imaging from light field measurements in an LED array microscope. *Optica*, vol. 2, no. 2, 2015: p. 104, ISSN 2334-2536.

[125] CHOWDHURY, S. et al.: High-resolution 3D refractive index microscopy of multiple-scattering samples from intensity images. *Optica*, vol. 6, no. 9, 2019: p. 1211, ISSN 23342536, <1909.00023>.

[126] LIM, J. et al.: High-fidelity optical diffraction tomography of multiple scattering samples. *Light: Science and Applications*, vol. 8, no. 1, 2019: pp. 1–12, ISSN 20477538.

[127] KINGMA, D. P. BA, J. L.: Adam: A method for stochastic optimization. *3rd International Conference on Learning Representations, ICLR 2015 - Conference Track Proceedings*, 2015: pp. 1–15, <1412.6980>.

[128] KOU, S. S. SHEPPARD, C. J. R.: Image formation in holographic tomography. *Opt. Lett.*, vol. 33, no. 20, 2008: pp. 2362–2364.

[129] KOU, S. S. SHEPPARD, C. J. R.: Image formation in holographic tomography: high-aperture imaging conditions. *Appl. Opt.*, vol. 48, no. 34, dec 2009: pp. H168—-H175.

[130] PARK, Y. et al.: Refractive index maps and membrane dynamics of human red blood cells parasitized by Plasmodium falciparum. *Proceedings of the National Academy of Sciences of the United States of America*, vol. 105, no. 37, sep 2008: pp. 13730–13735, ISSN 1091-6490.